

NORTHWESTERN UNIVERSITY

Search for Flavor Changing Neutral Higgs Decay from Top Quarks with
Multilepton Final States

A DISSERTATION

SUBMITTED TO THE GRADUATE SCHOOL
IN PARTIAL FULFILLMENT OF THE REQUIREMENTS

for the degree

DOCTOR OF PHILOSOPHY

Field of Physics

By

Nathaniel J. Odell

EVANSTON, ILLINOIS

June 2015

UMI Number: 3705331

All rights reserved

INFORMATION TO ALL USERS

The quality of this reproduction is dependent upon the quality of the copy submitted.

In the unlikely event that the author did not send a complete manuscript and there are missing pages, these will be noted. Also, if material had to be removed, a note will indicate the deletion.



UMI 3705331

Published by ProQuest LLC (2015). Copyright in the Dissertation held by the Author.

Microform Edition © ProQuest LLC.

All rights reserved. This work is protected against
unauthorized copying under Title 17, United States Code



ProQuest LLC.
789 East Eisenhower Parkway
P.O. Box 1346
Ann Arbor, MI 48106 - 1346

© Copyright by Nathaniel J. Odell 2015

All Rights Reserved

ABSTRACT

Search for Flavor Changing Neutral Higgs Decay from Top Quarks with Multilepton
Final States

Nathaniel J. Odell

After the discovery of the Higgs boson at the LHC, the task of characterizing its properties is underway. One property of particular interest is the Higgs coupling to the top quark, the heaviest known fermion. Given the masses of these two particles, $m_t = 173.34 \text{ GeV}$ and $m_H = 125.09 \text{ GeV}$, decays of the Higgs to top-antitop pairs are kinematically suppressed. Tree-level decays of a top quark to a Higgs boson plus an up or charm quark are, on the other hand, suppressed by the lack of flavor-changing neutral-currents in the standard model. However, there exist extensions of the standard model, such as supersymmetry, that require that there be multiple Higgs-like particles. Theories that incorporate such two Higgs doublet models can give rise to tree level flavor changing neutral Higgs decays of the top quark with branching fractions on the order of 10^{-3} .

The thesis describes a search for the process $t \rightarrow Hc$ using data collected with the CMS detector. Events with either two or three well-isolated leptons in their final state are investigated.

Acknowledgements

I would first like to thank my advisor, Mayda Velasco, who took me on as a complete novice in particle physics and made a physicist out of me in spite of myself. I would also like to thank my fellow graduate students working in the Northwestern CMS group, in particular (Andy, Andrey, and Brian), who shared in all of the triumphs and torments of earning a Ph.D.

I dedicate this thesis to my parents who would support me in any path I set out on, but were sure to nudge me in the right direction.

Table of Contents

ABSTRACT	3
Acknowledgements	4
List of Tables	7
List of Figures	9
Chapter 1. Introduction	19
Chapter 2. Definitions	22
2.1. Abbreviations	23
Chapter 3. Theory	25
3.1. The Standard Model	25
3.2. The Higgs Mechanism	27
3.3. SM Decays of the W and Z Bosons	33
3.4. The Top Quark	34
3.5. Flavor-Changing Neutral Currents and the GIM mechanism	36
3.6. Two Higgs Doublet Model	40
Chapter 4. Experiment Description	46
4.1. LHC	46

	6
4.2. The Compact Muon Solenoid (CMS)	48
Chapter 5. Analysis	60
5.1. Datasets	60
5.2. Object selection	65
5.3. Event selection	79
5.4. Background estimation	94
5.5. Systematics	120
5.6. Results	122
5.7. Conclusions	123
References	125
Appendix A. Supplemental analysis material	134
A.1. Analysis distributions by flavor category	134
A.2. Multi-variate analysis	164
Appendix B. Measurement of luminosity and normalized beam-induced background using CMS Fast Beam Conditions Monitor	169
B.1. Introduction	169
B.2. Beam Conditions Monitoring at CMS	169
B.3. BCM1F Signal Characterization	171
B.4. Beam-induced background measurement	173
B.5. Luminosity Determination and Calibration	176
B.6. Simulation	181
B.7. Conclusions	183

List of Tables

3.1	Decay modes and their branching fractions for the W and Z bosons.	34
3.2	Current experimental [1] and theoretical [2] status for measurement of t flavor violating decays mediated by a vector or higgs boson.	39
4.1	A short list of relevant LHC parameters with design specifications and values for the 2012 run.	47
5.1	2012 datasets: individual luminosities are determined based on a luminosity mask that is based on events that are processed. The datasets were gathered over the course of 2012 and reprocessed in January 2013.	61
5.2	Trigger efficiency scale factors between data and MC for HLT_Ele17_Ele8 for leading (top) and trailing (bottom) legs.	62
5.3	Simulated MC samples used in the analysis. All samples are from the production Summer12_DR53X-PU_S10_START53_V7A-v*/AODSIM tier data.	64
5.4	MET dependent HT cuts for same-sign dilepton extraction.	87
5.5	Event yields for trilepton (top) and same-sign (bottom) categories assuming $\mathcal{B}(t \rightarrow Hc) = 1\%$.	94

5.6	Yields for WZ control region. Quoted uncertainties are statistical only.	96
5.7	Yields in $t\bar{t}$ control region. Quoted uncertainties are statistical only.	98
5.8	Comparison of composition of fake rates after applying $\geq 2jet$ requirement for $\mu\mu$ and ee final states.	111
5.9	Bin-by-bin contribution to the fake rate uncertainty for muons (top) and electrons (bottom).	113
5.10	Sources of systematic uncertainty and the approximate effect on percent uncertainty of the yields.	122
5.11	Upper limits at 95% CL on branching fraction of $t \rightarrow Hc$ for three leptons, same-sign dilepton, and combined selections.	123
A.1	Event yields for trilepton category with eee final states.	134
A.2	Event yields for trilepton category with $ee\mu$ final states.	134
A.3	Event yields for trilepton category with $e\mu\mu$ final states.	134
A.4	Event yields for trilepton category with $\mu\mu\mu$ final states.	135
A.5	Event yields for same-sign dilepton category with $\mu\mu$ final states.	135
A.6	Event yields for same-sign dilepton category with ee final states.	135
A.7	Event yields for same-sign dilepton category with $e\mu$ final states.	135
A.8	Ranking of input variables for BDT by flavor category.	167

List of Figures

1.1	Feynmann diagrams of flavor-changing neutral higgs decays that result in trilepton or same-sign dilepton final states.	21
3.1	Summary of known particles of the standard model.	26
3.2	Higgs potential 3.11 for the case of $\mu^2 < 0$ and $\lambda > 0$.	30
3.3	Leading order diagrams for $t\bar{t}$ production.	35
3.4	Loop-induced FCNC in the SM for $t \rightarrow c\gamma$ decays.	36
3.5	Branching fraction for top decaying to a Higgs boson and charm quark for various top and Higgs masses. The solid lines indicate CP-even Higgs decays and dashed indicate CP-odd Higgs decays.	45
4.1	General layout of the LHC experiments, as well as the accelerator complex which supplies them with collisions.	47
4.2	Schematic view of the CMS detector showing the various sub-detectors.	49
4.3	Schematic side-view of the CMS silicon tracker.	50
4.4	CMS tracker resolution performance for single muons [?] as a function of η for three different charged particle momentums. Resolution for transverse momentum (left), transverse vertex resolution (center), and longitudinal vertex resolution (right) are shown.	51

		10
4.5	Schematic view of the CMS ECAL.	52
4.6	Energy resolution of the ECAL as a function of beam energy from electron test beam measurements.	53
4.7	Schematic side-view of the CMS HCAL.	54
4.8	Jet transverse momentum resolution as a function of p_T for different pileup scenarios (left), and for different jet compositions (right), as measured in 2012 data.	55
4.9	MET resolution measured in Z/γ events. The MET is projected either in the direction parallel (left) to the direction of the reconstructed Z/γ or perpendicular (right).	56
4.10	Schematic side-view of the CMS Muon detectors.	57
4.11	(Left) Residuals of reconstructed hits on the CSC strips in cosmic ray data. Expected position is acquired using a fit to the other 5 layers of the same CSC chamber. (Right) Summary of resolutions obtained for each chamber type compared to the design expectation.	58
5.1	Comparison of pileup distributions for 19.7 fb^{-1} of data taken at 8 TeV and simulation with S10 pileup scheme.	65
5.3	Multiplicity of leptons after selection of triggers and lepton identification (efficiency corrections are not applied). Uncertainties are statistical only and all background estimates are done with MC.	67

5.4	Number of events for in same-sign dilepton (left) and trilepton events by flavor category are shown. Lepton preselection (see section 5.3.1) is applied.	68
5.5	Scale factors for muon trigger efficiency between data and simulation. The scale factors are done in two bins of muon p_T : $10 \text{ GeV} < p_T < 20 \text{ GeV}$ (left) and $p_T > 20 \text{ GeV}$.	70
5.6	Scale factors for muon identification (left) and isolation (right) efficiency between data and simulation.	71
5.9	Multiplicity of jets in three lepton (left) and same-sign dilepton events (right) at the preselection level.	75
5.10	Efficiencies measured from MC for jets associated to b quarks (left), c quarks (middle), and light quarks or gluons (right) to pass CSV medium working point.	77
5.11	Multiplicity of b-jets passing medium CSV working point in three lepton (left) and same-sign dilepton events (right) at the preselection level.	78
5.2	Effect of applying pileup reweighting on reconstructed primary vertices distribution for three lepton (top left), same-sign dileptons (top right), and inclusive (bottom) final states.	81
5.7	Scale factors for efficiency of electrons between data and simulation.	81

5.8	ΔR between all muons and electrons in all events passing dilepton triggers. Does not include efficiency corrections or QCD background estimate.	82
5.12	MET distributions for trilepton events (left), and same-sign dilepton events (right) at the preselection level.	83
5.13	Examples of variables that are cut on in the analysis at the preselection level for three lepton events. From upper left to lower right they are OSSF dilepton mass, trilepton mass, MET, H_T , light jet multiplicity, and b-jet multiplicity.	84
5.14	Examples of variables that are cut on in the analysis at the preselection level for same-sign dilepton events. From upper left to lower right they are dilepton mass, MET, H_T , light jet multiplicity, and b-jet multiplicity.	85
5.15	Trilepton mass vs dilepton same-flavor, opposite-sign mass at the preselection level.	86
5.16	Distributions of events in the MET vs. H_T plane for same-sign dilepton events after requiring that there be at least 2 jets in the event. From left to right: signal, data, and background.	89
5.17	Multiplicity of all jets after the Z veto requirement for three lepton (left) and same-sign (right) selections.	89
5.18	Multiplicity of b-jets after the MET and H_T requirements for three lepton (left) and same-sign (right) selections.	90

5.19	MET distributions for three lepton (left) and same-sign selections after ≥ 2 jet requirement.	90
5.20	H_T distributions for three lepton (left) and same-sign selections after ≥ 2 jet requirement.	91
5.21	Examples of variables that are cut on in the analysis at the final selection level for three lepton events. From upper left to lower right they are opposite-sign, same flavor dilepton mass, trilepton mass, MET, H_T , light jet multiplicity, and b-jet multiplicity.	92
5.22	Examples of variables that are cut on in the analysis at the final selection level for same-sign dilepton events. From upper left to lower right they are dilepton mass, MET, H_T , light jet multiplicity, and b-jet multiplicity.	93
5.23	From upper left: MET, jet multiplicity, $M_{\ell\ell\ell}$, and $MT_{\ell 3, MET}$ distributions in WZ control region. Observed data distributions (points) are plotted against simulation.	97
5.24	MET and jet multiplicity distributions for the $t\bar{t}$ control region. Observed data distributions (points) are plotted against predicted Standard Model contributions.	98
5.25	Example of internal asymmetric conversion originating from Drell-Yan production.	99
5.26	Variables used to increase purity of QCD $b\bar{b}$ region: $\Delta\phi(tag, probe)$ is shown on the left; the balance is on the right.	102

5.27	Kinematic distributions for the tag muon in the QCD $b\bar{b}$ region.	103
5.28	p_T distributions for the probe muon (top left), passing muons (top right), probe electron (bottom left) and passing electrons (bottom right) in the QCD $b\bar{b}$ region.	104
5.29	Fake rates measured QCD $b\bar{b}$ region for muons (left), and electrons (right).	105
5.30	Kinematic distributions for the tag muon in the Z+jet region.	106
5.31	p_T distributions for the probe muon (top left), passing muons (top right), probe electron (bottom left) and passing electrons (bottom right) in the Z+jet region.	107
5.32	Composition of sample used for estimation of fake background. The QCD estimation is not shown, but is presumed to account for the missing background.	109
5.33	Fake rates measured in MC for various processes. Muon rates are shown on the left; electrons are on the right.	110
5.34	Comparison of fake rates measured in MC for measurement region and signal region compositions. Ratios between the two regions are shown in the bottom row with muons shown on the left, and electrons are shown on the right.	111
5.35	Fake rates measured from data (combined QCD and Z+jet rates) parameterized as a function of p_T for muons (left) and electrons (right). Error bands include both statistical and systematic uncertainties.	112

5.36	Templates used in the estimation of the fake background for muons (left) and electrons (right).	113
5.37	Transverse impact parameter of electrons in same-sign dielectron events before (left) and after (right) tightening the cut from 0.015 cm to 0.005 cm.	114
5.38	Charge flip η dependence in both data and Z+jets MC.	115
5.39	Dielectron mass for same-sign (left) and opposite-sign (right) pairs near the Z mass.	116
5.40	Two dimensional charge mis-identification rates for dielectron events.	117
5.41	Charge mis-identification probabilities parameterized by p_T for different η bins and jet multiplicities.	118
5.42	Comparison of charge flips measured using MC for events inside and outside a 30 GeV window centered on the Z mass for electrons with $ \eta < 0.8$ (top left), $0.8 < \eta < 1.479$ (top right), and $ \eta > 1.479$ (bottom).	119
A.1	Kinematic distributions for $e^\pm e^\pm$ at preselection level.	136
A.2	Analysis variables for $e^\pm e^\pm$ at preselection level.	137
A.3	Kinematic distributions for $e^\pm e^\pm$ after Z veto.	138
A.4	Analysis variables for $e^\pm e^\pm$ after Z veto	139
A.5	Kinematic distributions for $e^\pm e^\pm$ after 2 jet requirement.	140
A.6	Analysis variables for $e^\pm e^\pm$ after 2 jet requirement.	141

A.7	Kinematic distributions for $e^\pm e^\pm$ after MET and HT cuts.	142
A.8	Analysis variables for $e^\pm e^\pm$ after MET and HT cuts.	143
A.9	Kinematic distributions for $e^\pm \mu^\pm$ at preselection level.	144
A.10	Analysis variables for $e^\pm \mu^\pm$ at preselection level.	145
A.11	Kinematic distributions for $e^\pm \mu^\pm$ after 2 jet requirement.	146
A.12	Analysis variables for $e^\pm \mu^\pm$ after 2 jet requirement.	147
A.13	Kinematic distributions for $e^\pm \mu^\pm$ after MET and HT cuts.	148
A.14	Analysis variables for $e^\pm \mu^\pm$ after MET and HT cuts.	149
A.15	Kinematic distributions for $\mu^\pm \mu^\pm$ at preselection level.	150
A.16	Analysis variables for $\mu^\pm \mu^\pm$ at preselection level.	151
A.17	Kinematic distributions for $\mu^\pm \mu^\pm$ after 2 jet requirement.	152
A.18	Analysis variables for $\mu^\pm \mu^\pm$ after 2 jet requirement.	153
A.19	Kinematic distributions for $\mu^\pm \mu^\pm$ after MET and HT cuts.	154
A.20	Analysis variables for $\mu^\pm \mu^\pm$ after MET and HT cuts.	155
A.21	Kinematic distributions for eee at preselection level.	156
A.22	Analysis variables for $\mu^\pm \mu^\pm$ at preselection level.	157
A.23	Kinematic distributions for $\mu^\pm \mu^\pm$ at preselection level.	158
A.24	Analysis variables for $\mu^\pm \mu^\pm$ at preselection level.	159
A.25	Kinematic distributions for $\mu^\pm \mu^\pm$ at preselection level.	160
A.26	Analysis variables for $\mu^\pm \mu^\pm$ at preselection level.	161
A.27	Kinematic distributions for $\mu^\pm \mu^\pm$ at preselection level.	162

		17
A.28	Analysis variables for $\mu^\pm\mu^\pm$ at preselection level.	163
A.29	M_T distribution at preselection level for three lepton events.	165
A.30	Input variables for trilepton (top) and same-sign dilepton (bottom) BDT.	166
A.31	Correlation matrix of input variables for trilepton (top) and same-sign dilepton (bottom) BDT.	167
A.32	Significance and efficiencies for singal and background by cut of the trilepton (left) and same-sign dilepton (right) BDT discriminator output.	168
B.1	Schematic of arrival time for various beam products.	170
B.2	A schematic of the BCM1F readout chain	171
B.3	Pulse characterization from data collected with back-end ADC.	172
B.4	Single bunch hit probabilities as a function of the instantaneous luminosity measured by HF. Hit probability is measured for the leading bunch in each orbit.	173
B.5	Schematic of BCM1F back-end gating to select on beam-gas products (<i>left</i>). Comparison of beam-gas measurement and vacuum quality using pressure gauges (<i>right</i>).	175
B.6	Data gathered during the April 2012 VdM scan. The data is fit with a double gaussian plus constant where the single gaussian components are shown in red and green, the constant in blue, and the combined result is in black.	179

B.7	Comparison between CMS luminometers of width of beam overlap for x and y scans.	181
B.8	Examples of distributions that are generated from the ADC analysis and used as inputs to the detector simulation.	182
B.9	Results of simulation of the BCM1F counting rate as a function of bunch-crossing for fill pattern with 1380 filled bunches, 1331 of which are colliding at IP5.	183

CHAPTER 1

Introduction

The discovery of the Higgs boson at the Large Hadron Collider is a milestone in high energy physics, and resolves one of the outstanding quandries in our understanding of the fundamental properties of matter. In brief, the Higgs mechanism gives rise to particle masses by way of breaking the $SU(2) \times U(1)$ symmetry that describes electroweak interactions. This has been an outstanding issue for the half century since the Standard Model formalism began to take shape, and in a sense, provides the final piece.

Having confirmed the existence of the Higgs boson, efforts to characterize its properties are underway. Analyses based on data collected by the ATLAS and CMS collaborations have done preliminary measurements of the mass, spin statistics, and couplings of the Higgs. These results suggest the observed particle is consistent with Standard Model predictions, but still allow for possible beyond Standard Model properties.

Of particular interest is the coupling between the top quark and the Higgs boson, largely due to the top quark's large mass. The top quark is the only known fundamental particle which has a mass greater than the Higgs boson. Naively, the decay of a top quark to a Higgs boson plus a light flavored quark would be kinematically allowed, but is expected to be exceedingly rare due to suppression of flavor-changing neutral-current interactions.

In the standard model, there are strict limits on the amount of flavor changing neutral currents (FCNC). This is largely based on measurements of mixing of lighter flavor

quarks and decays involving neutral vector bosons. In the standard model, the decay of a top quark mediated by a Higgs boson is theorized to be highly suppressed (smaller than 10^{-11} [3–5]), but several extensions of the standard model, most significantly those involving a two Higgs boson doublet, allow for an enhancement of Higgs boson production through flavor-changing neutral decays. In some these models, $\text{BR}(t \rightarrow Hc)$ can be as large as 10^{-2} [5]. Therefore, detection of this enhancement could suggest new physics beyond the standard model.

This thesis will describe a measurement of the branching fraction $\text{BR}(t \rightarrow Hc)$ in multilepton final states using data gathered with the CMS detector. The final states under consideration are where the decays lead to trilepton (consisting of three prompt leptons) or same-sign dilepton (two prompt leptons where the charge of the two leptons are the same). Opposite-sign dilepton final states are not considered because the high production of such final states makes sensitivity to possible FCNC signals negligible. The relevant processes are shown in figure 1.1.

This document is split into three main categories:

- (1) description of the relevant theoretical background including the Higgs mechanism, flavor changing processes, and a beyond the standard model scenario that could give rise to enhanced FCNC;
- (2) a description of the CMS detector and LHC accelerator systems;
- (3) description of the analysis of CMS data to set an upper limit on the branching fraction of $t \rightarrow hc$.

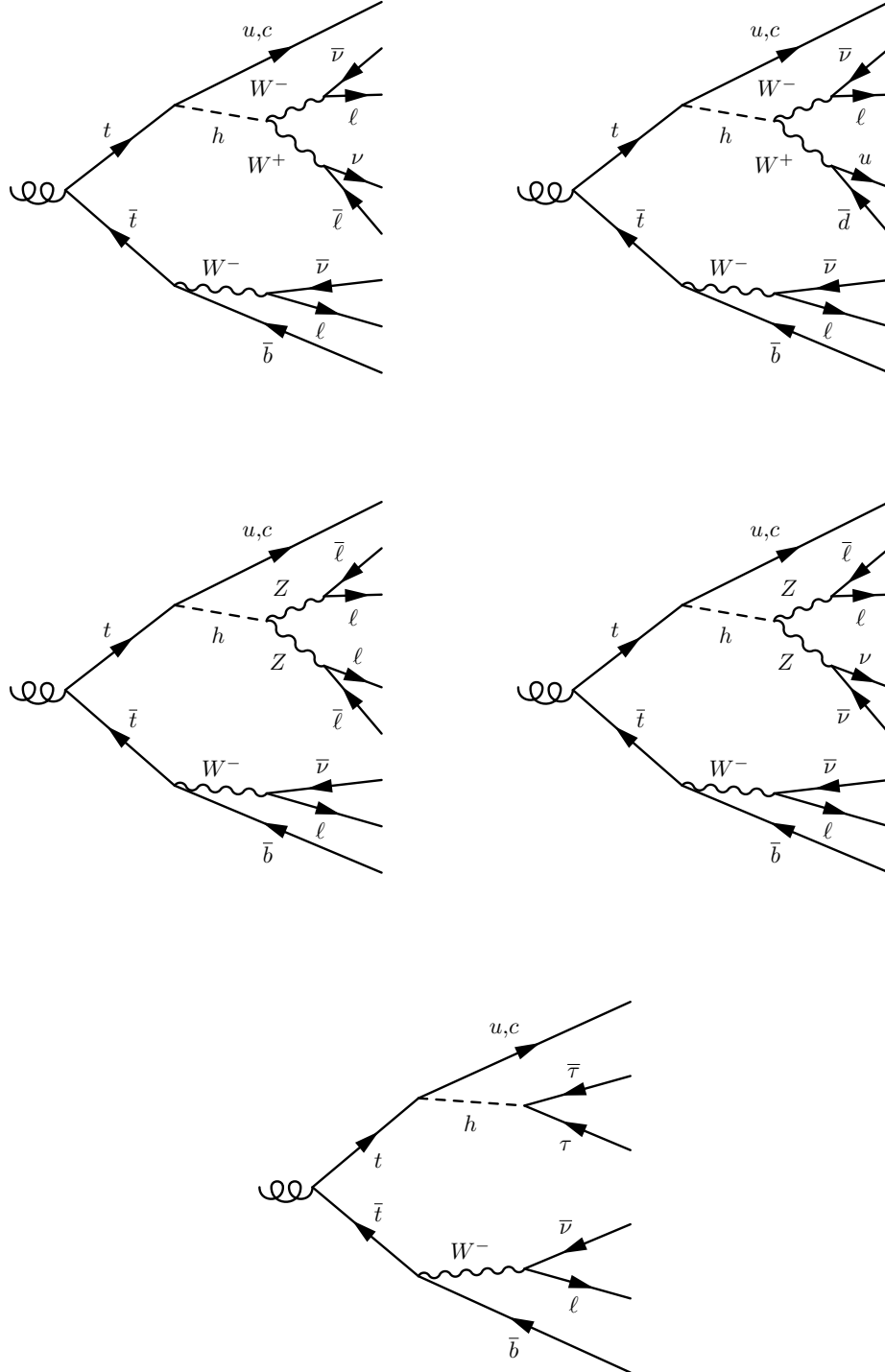


Figure 1.1. Feynmann diagrams of flavor-changing neutral higgs decays that result in trilepton or same-sign dilepton final states.

CHAPTER 2

Definitions

CMS [6] uses a coordinate system which defines the $+x$ axis to point towards the center of the LHC ring, the $+y$ axis to point upwards, and the z axis to lie along the beamline. The CMS coordinate system is right-handed, so the $+z$ direction corresponds to anti-clockwise if the ring is viewed from above. The origin of the coordinate system is at the nominal interaction point at the center of the CMS detector. The azimuthal angle ϕ is defined as the angle from the x -axis in the $x - y$ plane, and the polar angle θ is measured from the positive z direction in the $y - z$ plane.

It is typically more convenient to use the pseudorapidity $\eta = -\ln \left[\tan \left(\frac{\theta}{2} \right) \right]$, and to define relative distances ΔR between two vectors as the distance in $\eta - \phi$ space: $\Delta R = \sqrt{\Delta\eta^2 + \Delta\phi^2}$. In this way, it is possible to define a measure which is invariant with respect to Lorentz transformations along the beam axis.

The $x - y$ plane is perpendicular to the beam direction, and is therefore referred to as the “transverse” plane. A subscript “T” denotes a quantity measured in the transverse plane; the transverse momentum (p_T) is the projection of the particle momentum into the $x - y$ plane. Displacements along the z axis are said to be in the “longitudinal” direction.

It is conventional in particle physics to use the system of natural units, wherein the values of c (the speed of light) and \hbar (the reduced Planck’s constant) are defined to be one.

2.1. Abbreviations

ATLAS: A Large Toroidal LHC ApparatuS

CDF: Collider Detector at Fermilab

CERN: European Organization for Nuclear Research

CMS: Compant Muon Solenoid

CMSSW: CMS SoftWare

CSC: Cathode Strip Chamber

CTEQ: The Coordinated Theoretical-Experimental Project on QCD

DT: Drift Tube

DY: Drell-Yan

ECAL: Electromagnetic Calorimeter

EB: ECAL Barrel

EE: ECAL Endcap

FSR: Final-State Radiation (refers to QED photon emission in this thesis)

HCAL: Hadronic Calorimeter

HB: HCAL Barrel

HE: HCAL Endcap

HF: HCAL Forward detector

HO: HCAL Outer detector

HLT: High-Level Trigger

IP: Interaction Point

ISR: Initial-State Radiation (refers to QED photon emission in this thesis)

JSON: JavaScript Object Notation

L1T: Level-1 Trigger

LEP: Large Electron-Positron collider

LHC: Large Hadron Collider

MC: Monte Carlo

PDF: Parton Distribution Function

PF: Particle Flow

QCD: Quantum Chromodynamics

RPC: Resistive Plate Chamber

SM: Standard Model

SUSY: Supersymmetry

CHAPTER 3

Theory

3.1. The Standard Model

The Standard Model (SM) of particle physics is a quantum field theory that describes all known matter in terms of a small number of fermionic "matter" particles and three gauge interactions mediated by bosonic particles. Figure 3.1 summarizes all of the known standard model particles and some of their properties. The theory, proposed by Glashow, Salam, and Weinberg in the mid-1960s, unifies the electromagnetic and weak interactions. So far, no experimental result has contradicted a prediction of the SM. This fact is a testament to the robustness of the theoretical framework.

The notion of symmetry is of paramount importance in physics, and has guided the development of physical theories describing a multitude of phenomena. The underlying mechanism upon which the SM is built is the gauge principle, that is, if the Lagrangian describing the dynamics of a system is required to be invariant under a certain group transformation, this can be used to describe the interactions amongst particles.

The electroweak portion of the SM lagrangian can be written in compact form as,

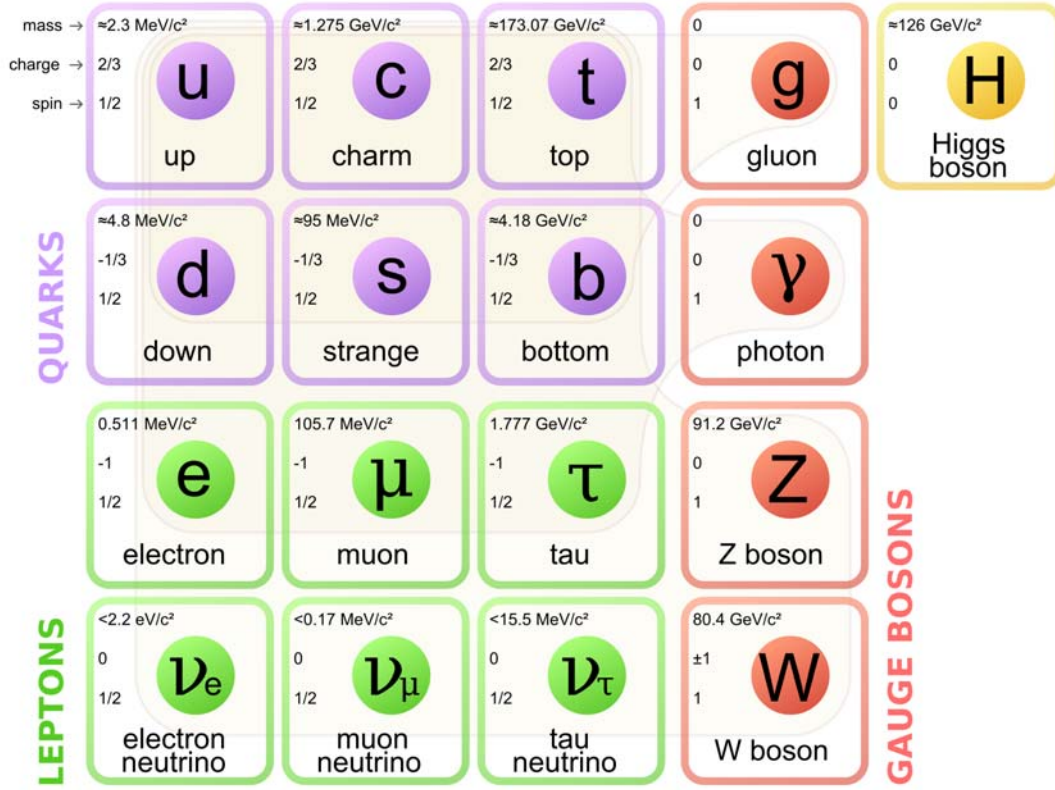


Figure 3.1. Summary of known particles of the standard model.

$$(3.1) \quad \mathcal{L} = -\frac{1}{4} \mathbf{F}_{\mu\nu}^a \mathbf{F}^{a\mu\nu}$$

$$(3.2) \quad \begin{aligned} &+ i\bar{\psi} \not{D} \psi + h.c. \\ &+ \psi_i y_{ij} \psi_j + h.c. \\ &+ |D_\mu \phi|^2 - V(\phi). \end{aligned}$$

The first two lines describe the dynamics of the fermions and boson fields and have been verified by numerous experiments. The validity of the last two lines has only recently

been confirmed with the discovery of the Higgs boson at the LHC [7, 8]. The third line describes the coupling of the Higgs field to the fermions while the fourth describes the dynamics of Higgs field including its self-interaction.

3.2. The Higgs Mechanism

It is worth exploring the Higgs mechanism closer. Absent the Higgs term, the SM lagrangian includes terms describing just the $(\text{SU}(2)_L \times \text{U}(1)_Y)$ gauge bosons and the fermions (for this discussion, the strong interaction between quarks is ignored). That is,

$$(3.3) \quad \mathcal{L} = \mathcal{L}_{\text{gauge}} + \mathcal{L}_{\text{fermions}},$$

where,

$$(3.4) \quad \mathcal{L}_{\text{gauge}} = -\frac{1}{4}F_{\mu\nu}^a F^{a\mu\nu} - \frac{1}{4}f_{\mu\nu}$$

$$(3.5) \quad \mathcal{L}_{\text{fermions}} = \bar{\text{R}} \left(\partial_\mu + i\frac{g'}{2}\mathcal{A}_\mu Y \right) \text{R} + \bar{\text{L}} i\gamma^\mu \left(\partial_\mu + i\frac{g'}{2}\mathcal{A}_\mu Y + i\frac{g}{2}\boldsymbol{\tau} \cdot \mathbf{B}_\mu \right) \text{L}.$$

The gauge term consists of the field-strength tensors, $F_{\mu\nu}$ and $f_{\mu\nu}$, which pertain to the SU(2) isospin and U(1) hypercharge components, respectively, and are defined in terms of the field potentials as,

$$(3.6) \quad f_{\mu\nu} = \partial_\mu \mathcal{A}_\nu - \partial_\nu \mathcal{A}_\mu;$$

$$(3.7) \quad F_{\mu\nu}^a = \partial_\mu B_\nu^a - \partial_\nu B_\mu^a + g\varepsilon_{bca} B_\mu^b B_\nu^c \text{ for } a = 1, 2, 3.$$

Here \mathcal{A}_μ and B_μ are the potentials associated with the U(1) and SU(2) parts of the electroweak fields, respectively, and g and g' are the corresponding coupling strengths. The fermionic portion describes the kinetic behavior (terms involving ∂_μ) as well the interactions between the left and right-handed fermions and the gauge bosons. The interaction terms come about by requiring invariance under the relevant gauge transformations. To meet this condition, the covariant derivatives are used in place of ordinary space-time derivatives, i.e.,

$$(3.8) \quad \partial_\mu \rightarrow D_\mu = \partial_\mu + \frac{ig'}{2} A_\mu Y + \frac{ig}{2} \boldsymbol{\tau} \cdot \mathbf{B}_\mu.$$

In this form, the gauge bosons ($\mathcal{A}_\mu, B_\mu^1, B_\mu^2, B_\mu^3$) are massless. This, of course, is contrary to what would be expected given that the W and Z bosons only interact over a limited range.

As the theory stood at this point, all the vector bosons are treated as being identical. Clearly this symmetry is broken in the real world. The idea of a spontaneously-broken local symmetry was successfully integrated into the standard model through work published separately by Englert and Brout [9] and Peter Higgs [10, 11]. This work incorporated ideas from condensed matter physics, notably work by Anderson [12] and Nambu [13],

that was used to describe superconductivity in terms of a spontaneously-broken local U(1) symmetry.

To see how spontaneous symmetry breaking gives rise to massive particles (both gauge bosons and fermions), a scalar field that is a complex doublet of SU(2) is introduced,

$$(3.9) \quad \phi = \begin{pmatrix} \phi^+ \\ \phi^0 \end{pmatrix}$$

and added into the Lagrangian,

$$(3.10) \quad \mathcal{L}_{\text{Higgs}} = (D_\mu \phi)^\dagger (D^\mu \phi) - V(\phi^\dagger \phi),$$

where the effective potential, $V(\phi^\dagger \phi)$, is defined as,

$$(3.11) \quad V(\phi^\dagger \phi) = \mu^2 (\phi^\dagger \phi) + \lambda (\phi^\dagger \phi)^2.$$

As will be shown, this potential gives rise to a non-zero vacuum expectation value (v.e.v.) in the case that the mass term, μ^2 , is negative and the coefficient of the ϕ^4 term, λ , is required to be positive. This Higgs potential is shown in figure 3.2. From this picture, it is clear that $|\phi| = 0$ is a local maximum.

Additionally, it is desirable to include terms that describe the interaction between the Higgs field and the fermion fields,

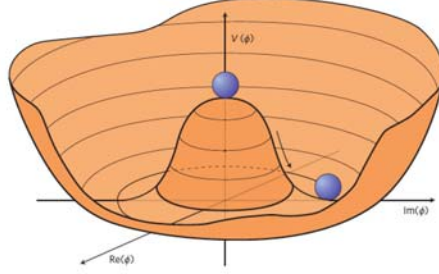


Figure 3.2. Higgs potential 3.11 for the case of $\mu^2 < 0$ and $\lambda > 0$.

$$(3.12) \quad \mathcal{L}_{\text{Yukawa}} = -g_f [\bar{R}\phi^\dagger L + \bar{L}\phi R] .$$

Through the Yukawa coupling, the matter particles, are imbued with mass which corresponds to the strength of their coupling to the Higgs field. An important corollary of this is the Higgs field couples more strongly to particles that are more massive.

To determine the v.e.v. of the Higgs field, the minimum of the effective potential needs to be determined, that is,

$$(3.13) \quad \frac{\partial}{\partial (\phi^\dagger \phi)} V(\phi^\dagger \phi) = 0 \rightarrow \mu^2 + 2\lambda \left[(\phi_{\text{vac}}^+)^2 + (\phi_{\text{vac}}^0)^2 \right] = 0.$$

Based on this expression, There is some flexibility in the choice of ground state energies for the two components of the Higgs doublet. A popular choice is $\phi_{\text{vacuum}}^+ = 0$ and $\phi_{\text{vacuum}}^0 = \sqrt{-\mu^2/(2\lambda)}$ since it breaks both the SU(2) and U(1) symmetries, while maintaining a residual U(1) gauge symmetry associated with electromagnetism. The broken symmetries lead to the appearance of three massless Goldstone bosons [14]. These Goldstone bosons

introduce three additional degrees of freedom which are "eaten" by the weakly interacting gauge bosons to give them a longitudinal spin degree of freedom.

To see how the Goldstone boson degrees of freedom, ξ , are absorbed into the massive gauge bosons, it is useful to consider perturbations around the vacuum. The Higgs field perturbed from the ground state by an amount η can be represented as follows,

$$(3.14) \quad \phi = \exp \left[\frac{i\xi \cdot \tau}{2v} \right] \begin{pmatrix} 0 \\ (v + \eta) / \sqrt{2} \end{pmatrix},$$

and then apply a gauge transformation so that the fields associated to the Higgs boson, the gauge bosons, and the fermions transform as,

$$(3.15) \quad \phi \rightarrow \phi' = \exp \left[\frac{-i\xi \cdot \tau}{2v} \right] \phi,$$

$$(3.16) \quad \tau \cdot \mathbf{B}_\mu \rightarrow \tau \cdot \mathbf{B}'_\mu,$$

$$(3.17) \quad L \rightarrow L' = \exp \left[\frac{-i\xi \cdot \tau}{2v} \right] L.$$

Both \mathcal{A}_μ and R are invariant under transformations by τ (SU(2) matrices; Pauli spin matrices) and are therefore not shown here. Before rewriting the Higgs Lagrangian given this parametrization, it is useful to write the physical vector bosons in terms of the gauge bosons,

$$(3.18) \quad W_\mu^\pm \equiv \frac{B_\mu^1 \mp i B_\mu^2}{\sqrt{2}},$$

$$(3.19) \quad Z_\mu \equiv \frac{-g' \mathcal{A}_\mu + g B_\mu^3}{\sqrt{g^2 + g'^2}},$$

$$(3.20) \quad \mathcal{A}_\mu \equiv \frac{g \mathcal{A}_\mu + g' B_\mu^3}{\sqrt{g^2 + g'^2}}.$$

The Higgs portion of the Lagrangian can then be written,

$$(3.21) \quad \mathcal{L}_{Higgs} = \left[\frac{1}{2} (\partial^{mu} \eta) (\partial_{mu} \eta) - \frac{\mu^2}{2} \eta^2 \right] + \frac{v^2 g^2}{8} (W^{+\mu} W_\mu^+ + W^{-\mu} W_\mu^-) + \frac{(g^2 + g'^2) v^2}{8} Z^\mu Z_\mu + \dots$$

The terms in square brackets describe the dynamics of the free Higgs field while the remaining terms show the Higgs coupling to the W and Z vector bosons. It is clear the massless photon (\mathcal{A}_μ) interaction term is absent as is expected due to the unbroken U(1) symmetry. The massive gauge bosons have masses given by,

$$(3.22) \quad m_W = \frac{gv}{2}, m_Z = \frac{v}{2} \sqrt{g^2 + g'^2}.$$

The final component in the SM Lagrangian to be addressed is the portion describing the coupling of the Higgs to the fermions. The Yukawa terms can be summarised as,

$$(3.23) \quad \mathcal{L}_{Yukawa} = -g_f \frac{v + \eta}{\sqrt{2}} (\bar{e}_R e_L + \bar{e}_L e_R),$$

where the coupling is proportional to the mass of the fermion given by,

$$(3.24) \quad m_f = g_f \frac{v}{\sqrt{2}}.$$

This analysis is concerned with the coupling between the top quark and the Higgs boson which is described in the Yukawa term. As can be seen from 3.23, this coupling occurs between $t\bar{t}$ pairs, and does not give rise to flavor changing terms. In later sections, consideration will be given to how flavor changing interaction occur in the SM, and how the SM can be extended to include flavor violating Yukawa couplings between the up-type quarks.

3.3. SM Decays of the W and Z Bosons

The allowed SM decay modes of W and Z bosons give rise to the production of fermion pairs. In the case of W boson, its decay results in the fermions produced at the interaction vertex be separated by one unit of electrical charge and that the flavor change. This results in the production of either a charged lepton and a neutrino, or an up-type quark and a down-type anti-quark (or vice versa). The Z boson, on the other hand, decays to lepton-antilepton or quark-antiquark pairs.

The leptonic decays of the W and Z make for an exceptionally clean experimental signature due to the high transverse momentum and isolation of the resulting particles. The branching fractions are summarized in table 3.1 [15]. This analysis relies on defining the signal topology in terms of isolated leptons produced in these types of decays.

Decay mode	$\mathcal{B}(V \rightarrow X)(\%)$
W	
$e\nu_e$	10.72 ± 0.16
$\mu\nu_\mu$	10.57 ± 0.22
$\tau\nu_\tau$	10.74 ± 0.27
hadrons	67.96 ± 0.35
Z	
e^+e^-	3.363 ± 0.004
$\mu^+\mu^-$	3.366 ± 0.007
$\tau^+\tau^-$	3.370 ± 0.008
neutrinos	20.00 ± 0.06
hadrons	69.91 ± 0.06

Table 3.1. Decay modes and their branching fractions for the W and Z bosons.

3.4. The Top Quark

The top quark has been intensely studied since its discovery by the CDF [16] and D0 [17] experiments in 1995. It is of particular interest because of its large mass ($m_t = 173.34 \pm 0.76 \text{ GeV}$ [18]) which is the largest of the known fundamental particles and is significantly more massive than the next heaviest quark. The large mass of the top quark makes it important in radiative corrections involving new particles and suggests that it might have a special role in electroweak symmetry breaking.

The existent of the top quark was proposed as part of the extension of the Glashow-Illiopolous-Maiani mechanism (see section 3.5) developed by Kobayashi and Maskawa. It is an up-type quark ($Q = +2/3e$) and is the weak isospin ($T_3 = -1/2$) partner of the bottom quark. The top quark's large mass results in a short lifetime ($\approx 10^{-25}\text{s}$) which is less than the characteristic time scale of the strong interaction. The result of this is that the top quark decays through electroweak interactions rather than hadronization

mediated by the strong force. This allows for the study bare quark properties such as spin properties. The branching fraction of $t \rightarrow Wb$ is nearly 100%.

3.4.1. $t\bar{t}$ Production at the LHC

The LHC is only the second generation (after the Tevatron) of experiments that have been capable of measuring the properties of the top quark. The production cross-section of top-antitop pairs is $\sim 20\times$ higher at the LHC than at the Tevatron with a value of $\sigma_{t\bar{t}} = 252\text{pb}$ [19] at $\sqrt{s} = 8\text{TeV}$. The predominant production channel at the LHC involves gluon fusion as opposed to quark-antiquark annihilation at the TeV. Figure 3.3 shows the leading-order diagrams for $t\bar{t}$ production.

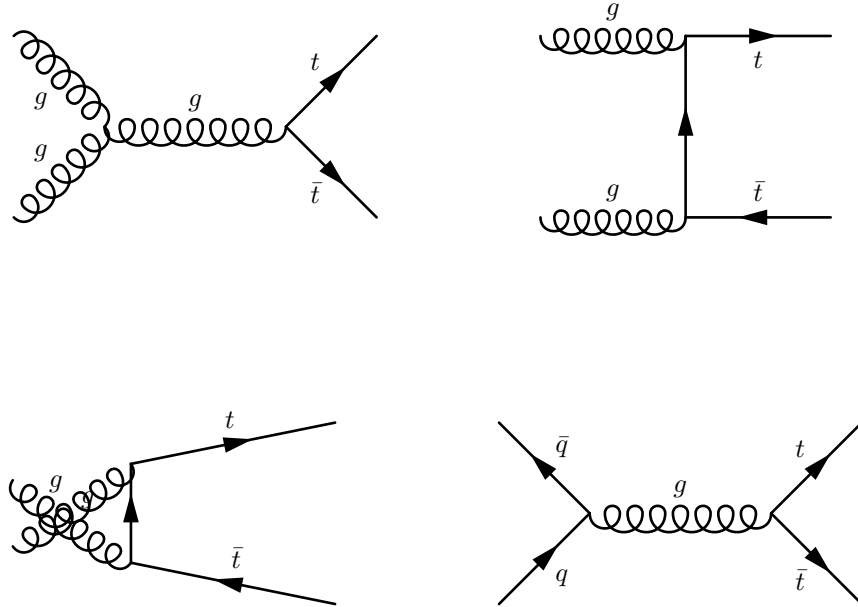


Figure 3.3. Leading order diagrams for $t\bar{t}$ production.

3.5. Flavor-Changing Neutral Currents and the GIM mechanism

In the SM, tree-level flavor-changing interactions are exclusively mediated through the W boson, that is, there are no flavor-changing interactions that do not also change the charge of a particle. Flavor-Changing Neutral Currents (FCNC) are heavily suppressed in the SM due to the Glashow-Illiopoulos-Maiani (GIM) mechanism [20], and only occur through a one-loop decays (see figure 3.4).

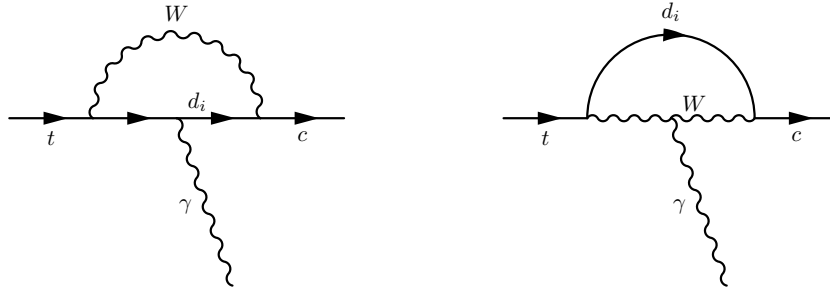


Figure 3.4. Loop-induced FCNC in the SM for $t \rightarrow c\gamma$ decays.

To understand how the GIM mechanism works, it is useful to consider the state of the model of quark interactions at the time it was proposed. The model, as layed out by Gell-Mann [21] and Zweig [22], only included the observed u , d , and s quarks. That is, the quarks sector could be represented in the triplet,

$$(3.25) \quad q = \begin{bmatrix} u \\ d \\ s \end{bmatrix},$$

and the hadronic portion of the weak current can be written,

$$(3.26) \quad J_\mu^{had} = \bar{q}\gamma_\mu(1 - \gamma_5)\mathcal{C}q.$$

where,

$$(3.27) \quad \mathcal{C} = \begin{pmatrix} 0 & \cos\theta_c & \sin\theta_c \\ 0 & 0 & 0 \\ 0 & 0 & 0 \end{pmatrix}.$$

Here $\theta_C = 0.257$, is the Cabibo angle [23] which indicates the down-type quark mixing and preserves universality of the weak current in the quark sector. This formulation will give rise to neutral current terms coupling down and strange quarks. This appeared to be contradicted by observations of kaon decays, in particular, the lack of $K_L \rightarrow \mu^+\mu^-$. With the addition of the charge 2/3 charm quark, the terms in the weak current become

$$(3.28) \quad U = \begin{pmatrix} u \\ c \end{pmatrix}; \quad D = \begin{pmatrix} d \\ s \end{pmatrix}; \quad \mathcal{C} = \begin{pmatrix} 0 & \cos \theta & \sin \theta \\ 0 & -\sin \theta & \cos \theta \\ 0 & 0 & 0 \end{pmatrix},$$

and the FCNC terms cancel. The important thing here is that because of the orthogonality of \mathcal{C} , the neutral current associated with the third component of the weak isospin is flavor diagonal,

$$(3.29) \quad 2(I_W)_3 = [\mathcal{C}, \mathcal{C}^\dagger] = \begin{pmatrix} UU^T & 0 \\ 0 & -U^T U \end{pmatrix} = \begin{pmatrix} 1 & 0 \\ 0 & -1 \end{pmatrix}.$$

This result combined with fact that the hypercharge component of the physical Z^0 is also flavor diagonal implies no tree-level FCNC.

Of course, it is now known that there are at least three generations of quarks. This is empirical fact at this point, but was initially proposed by Kobayashi and Maskawa to account for the observed CP violation in weak interactions. The extension of the GIM mechanism to include the mixing between the top, bottom, and other quarks is described by the CabibboKobayashiMaskawa (CKM) matrix,

$$(3.30) \quad \begin{bmatrix} d' \\ s' \\ b' \end{bmatrix} = \begin{bmatrix} V_{ud} & V_{us} & V_{ub} \\ V_{cd} & V_{cs} & V_{cb} \\ V_{td} & V_{ts} & V_{tb} \end{bmatrix} \begin{bmatrix} d \\ s \\ b \end{bmatrix}.$$

The matrix elements can be parameterized by three real angles and one complex phase, and the experimentally determined values for their magnitudes are [24],

$$(3.31) \quad U_{CKM} = \begin{pmatrix} 0.97428 \pm 0.00015 & 0.2253 \pm 0.0007 & 0.00347^{+0.00016}_{-0.00012} \\ 0.2252 \pm 0.0007 & 0.97345^{+0.00015}_{-0.00016} & 0.0410^{+0.0011}_{-0.0007} \\ 0.00862^{+0.00026}_{-0.00020} & 0.0403^{+0.0011}_{-0.0007} & 0.999152^{+0.000030}_{-0.000045} \end{pmatrix}$$

The current theoretical and experimental limits on all FCNC interactions is shown in table 3.2. From the table it is clear that the largest enhancement in FCNC come from a two Higgs doublet model that incorporates flavor violation. This will be explored in more detail in the following section.

Process	Measured	SM	2HDM (FV)	2HDM(FC)	MSSM	RPV	RS
$t \rightarrow Zu$ [25]	5×10^{-4}	7×10^{-17}	—	—	$\leq 10^{-7}$	$\leq 10^{-6}$	—
$t \rightarrow Zc$ [25]	5×10^{-4}	1×10^{-14}	$\leq 10^{-6}$	$\leq 10^{-10}$	$\leq 10^{-7}$	$\leq 10^{-6}$	$\leq 10^{-5}$
$t \rightarrow \gamma u$ [26]	3×10^{-2}	4×10^{-16}	—	—	$\leq 10^{-8}$	$\leq 10^{-9}$	—
$t \rightarrow \gamma c$ [26]	3×10^{-2}	5×10^{-14}	$\leq 10^{-7}$	$\leq 10^{-9}$	$\leq 10^{-8}$	$\leq 10^{-9}$	$\leq 10^{-9}$
$t \rightarrow gu$ [27]	3×10^{-5}	7×10^{-17}	—	—	$\leq 10^{-7}$	$\leq 10^{-6}$	—
$t \rightarrow gc$ [27]	2×10^{-4}	1×10^{-14}	$\leq 10^{-4}$	$\leq 10^{-8}$	$\leq 10^{-7}$	$\leq 10^{-6}$	$\leq 10^{-10}$
$t \rightarrow hu$ [28]	5×10^{-3}	2×10^{-17}	6×10^{-6}	—	$\leq 10^{-5}$	$\leq 10^{-9}$	—
$t \rightarrow hc$ [28]	5×10^{-3}	3×10^{-15}	2×10^{-3}	$\leq 10^{-5}$	$\leq 10^{-5}$	$\leq 10^{-9}$	$\leq 10^{-4}$

Table 3.2. Current experimental [1] and theoretical [2] status for measurement of t flavor violating decays mediated by a vector or higgs boson.

3.6. Two Higgs Doublet Model

There are several extensions of the SM (R-parity violation, Randal-Sundrum extra dimensions, etc.) that could potentially give rise to an enhancement in FCNC. The one that results in the largest enhancement in Higgs mediated FCNC decays is the two Higgs doublet model (2HDM).

As the name suggests, this model extends the higgs sector to consist of two weak isospin doublets rather than just one as described in section 3.2. The main motivation for this is supersymmetry. In supersymmetric theories, scalars belong to chiral multiplets and only couple to multiplets of the same chirality. It is therefore not possible to couple a single Higgs doublet to up-type and down-type quarks. Hence, in the Minimal Supersymmetric Standard Model, there are two Higgs doublets to give mass to all quark types.

The most general scalar potential in the 2HDM has 14 parameters and can have CP-conserving, CP-violating, and charge-violating minima. It is typical to assume that CP is conserved and not spontaneously broken. It is also common to introduce discrete symmetries to eliminate quartic terms that are odd in the doublets (motivated by the assumption of no tree-level FCNC). Under these assumptions, the potential for two doublets, Φ_1 and Φ_2 with hypercharge +1, can be written,

$$(3.32) \quad V = m_{11}^2 \Phi_1^\dagger \Phi_1 + m_{22}^2 \Phi_2^\dagger \Phi_2 + m_{12}^2 (\Phi_1^\dagger \Phi_2 + \Phi_1^\dagger \Phi_2) + \frac{\lambda_1}{2} (\Phi_1^\dagger \Phi_1)^2 \\ + \frac{\lambda_2}{2} (\Phi_2^\dagger \Phi_2)^2 + \lambda_3 \Phi_1^\dagger \Phi_1 \Phi_2^\dagger \Phi_2 + \lambda_4 \Phi_1^\dagger \Phi_2 \Phi_2^\dagger \Phi_1 + \frac{\lambda_f}{2} \left[(\Phi_1^\dagger \Phi_2)^2 + (\Phi_1^\dagger \Phi_2)^2 \right]$$

where all coefficients are real. Minimizing the field gives the v.e.v. of both fields,

$$(3.33) \quad \langle \Phi_1 \rangle_0 = \begin{pmatrix} 0 \\ \frac{v_1}{\sqrt{2}} \end{pmatrix}, \langle \Phi_2 \rangle_0 = \begin{pmatrix} 0 \\ \frac{v_2}{\sqrt{2}} \end{pmatrix},$$

which results in 8 fields: five physical fields and three Goldstone modes that are again absorbed into the W^\pm and Z^0 bosons giving them mass.

A general feature of 2HDMs is tree-level FCNC. This is typically considered to be problematic, and the discrete symmetries are introduced to suppress FCNC. This is motivated by phenomenological considerations, in particular, the mixing of $K - \bar{K}$ at tree-level. In this document, the type III 2HDM is considered. This model is constructed to allow for tree-level FCNC, but have sufficient suppression for lighter quarks so as not to conflict with empirical constraints. Additionally, this suppression of FCNC must be achieved without having scalar Higgs with multi-TeV masses.

The Yukawa couplings in this model look like,

$$(3.34) \quad \mathcal{L} = \eta_{ij}^U \bar{Q}_{iL} \bar{H}_1 U_{jR} + \eta_{ij}^D \bar{Q}_{iL} H_1 D_{jR} + \eta_{ij}^L \bar{L}_{iL} H_1 E_{jR}$$

$$(3.35) \quad + \hat{\xi}_{ij}^U \bar{Q}_{iL} \bar{H}_2 U_{jR} + \hat{\xi}_{ij}^D \bar{Q}_{iL} H_2 D_{jR} + \hat{\xi}_{ij}^L \bar{L}_{iL} H_2 E_{jR} + h.c.$$

where the basis for the Higgs has been rotated so that the vev is completely in the basis for the H_1 doublet,

$$(3.36) \quad \langle H_1 \rangle_0 = 1 \begin{pmatrix} 0 \\ v/\sqrt{2} \end{pmatrix}, \langle H_2 \rangle_0 = \begin{pmatrix} 0 \\ 0 \end{pmatrix}.$$

Because of the choice of basis, only the terms involving η_{ij} contribute to generating fermion mass. The other terms give rise to the FCNC interactions,

$$(3.37) \quad \mathcal{L}_{\text{FCNC}} = \xi_{ij}^U \bar{U}_{iL} \bar{H}_2^0 U_{jR} + \xi_{ij}^D \bar{D}_{iL} H_2^0 D_{jR} + \xi_{ij}^L \bar{L}_{iL} H_2^0 L_{jR}$$

where the coefficients ξ_{ij} have been transformed along with the Higgs basis and are effectively arbitrary. The earliest work addressing these types of couplings was done by Bjorken and Weinberg [29] where they chose $\xi_{\mu e}^L$ to be the Yukawa coupling to the muon based on radiative muon decays. Later, work done by McWilliams and Li [30] and Shanker [31] used the decays of muons and kaons as well as $K - \bar{K}$ mixing to argue that the heaviest fermions set the scale for the Yukawa-coupling matrix so $\xi^{U,D,L}$ should be approximately equal to the top, bottom, and tau Yukawa couplings respectively. This leads to a lower bound on the mass of the H_2^0 of 150 TeV. This motivated the prevailing assumption that a discrete symmetry must exist to inhibit the FCNC couplings.

It was not until work done by Cheng and Sher [32] that the so-called type III 2HDM model became viable. They asserted that setting the FCNC couplings to be equal to the Yukawa-couplings of the heaviest fermions was not reliable and proposed that the geometric mean between of the two fermion's Yukawa couplings should be used, i.e.,

$$(3.38) \quad \xi_{ij} = \lambda_{ij} \sqrt{m_i m_j} \frac{\sqrt{2}}{2}$$

where λ_{ij} are of order one. This is referred to as the Cheng-Sher *Ansatz*. This results in suppression of tree-level FCNC processes involving the first two generations of fermions and a reduction on the lower bound of the Higgs mass.

The first calculations of the branching fraction for $t \rightarrow ch_0$ using the Cheng-Sher *ansatz* were carried out by Wei-Shu Hou [33]. In his calculations, the following terms in the Yukawa Lagrangian were under consideration to be considered,

$$(3.39) \quad \mathcal{L} = -\lambda_{tc} \bar{c} t H^0 - i\lambda_{ct} \bar{c} \gamma_5 t A^0 + h.c.$$

where only terms involving the CP-even scalar, H^0 , and CP-odd pseudoscalar, A^0 contribute. With the assumption (now verified to be true for the CP-even scalar) that $M_\phi < m_t$, the decay width can be written,

$$(3.40) \quad \Gamma(t \rightarrow c\phi^0) = \frac{|\lambda_{tc}|^2}{16\pi} \times m_t \times [(1 \pm \rho_c)^2 - \rho_\phi^2] \times \sqrt{1 - (\rho_\phi + \rho_c)^2} \sqrt{1 - (\rho_\phi - \rho_c)^2},$$

where $\rho_c = m_c/m_t$, $\rho_\phi = M_\phi/m_t$, and the $+$ ($-$) corresponds to whether ϕ is scalar(pseudoscalar).

It is assumed that the total decay width is,

$$(3.41) \quad \Gamma_t = \Gamma(t \rightarrow bW) + \Gamma(t \rightarrow c\phi^0),$$

so the $t \rightarrow c\phi^0$ branching fraction is,

$$(3.42) \quad \mathcal{B}(t \rightarrow c\phi^0) = \frac{\Gamma(t \rightarrow c\phi^0)}{\Gamma_t}.$$

The branching fraction for various values of the Higgs mass and top quark mass is shown in figure 3.5 assuming Γ_t as in [34]. The Cheng-Sher *ansatz* can be used to set the coupling strength,

$$(3.43) \quad \lambda_{tc} = \frac{\sqrt{m_t m_c}}{v} \simeq 0.063.$$

Using $m_t = 173.3 \text{ GeV}$, $m_c = 1.4 \text{ GeV}$, and $M_\phi = 125 \text{ GeV}$ the branching fraction can be calculated to be, $\mathcal{B}(t \rightarrow c\phi^0) = 2.2 \times 10^{-3}$. In the case of the decays to the top quark, the branching fraction is decreased by approximately a factor of $m_u/m_t \simeq 10^{-3}$.

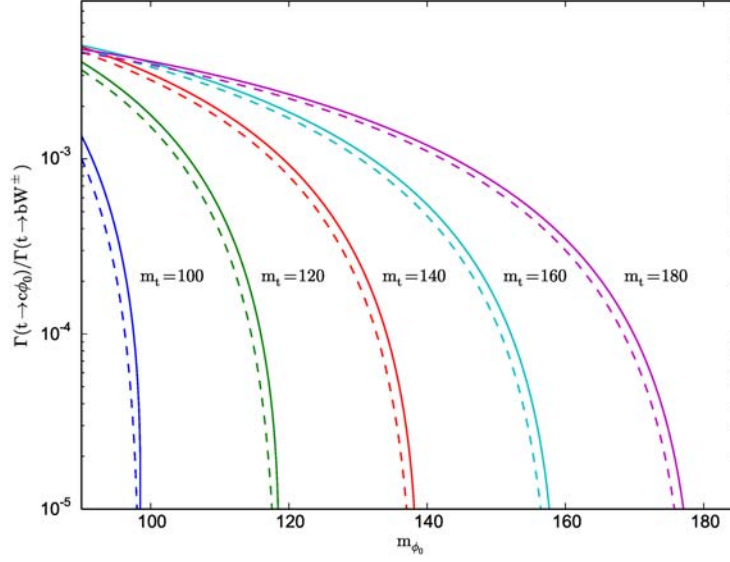


Figure 3.5. Branching fraction for top decaying to a Higgs boson and charm quark for various top and Higgs masses. The solid lines indicate CP-even Higgs decays and dashed indicate CP-odd Higgs decays.

CHAPTER 4

Experiment Description

4.1. LHC

The LHC [35] is a two-ring, superconducting, hadron collider located at the European Organization for Nuclear Research (CERN) facility near Geneva, Switzerland. It is installed approximately 100 meters underground in the 27 km circumference tunnel that had previously housed the LEP collider. A cartoon schematic of the LHC is shown in figure 4.1.

The LHC design was motivated by the search to determine the nature of electroweak symmetry breaking, now confirmed to be due to the Higgs mechanism, which in practical terms, translates into the requirement for higher energies and higher collision rates. The LHC is designed to collide protons at a center-of-mass energy of $\sqrt{s} = 14 \text{ TeV}$, and have a peak luminosity of $\mathcal{L} = 10^{34} \text{ cm}^{-2}\text{s}^{-1}$. These design conditions require a careful consideration of the detector systems. Of particular concern is the energies of collision products that will traverse the detector, and the rate at which they will be produced. Table 4.1 gives a summary of relevant parameters characterizing the LHC for both the 2012 run and by design.

4.2. The Compact Muon Solenoid (CMS)

The LHC has two general purpose detectors one of which is the Compact Muon Solenoid (CMS) [6]. As alluded to in the previous section, the design of the detector is motivated by the need to discern the products of highly energetic collisions, and to efficiently gather data given the high rate at which the collisions occur. The latter consideration is addressed by using highly-segmented, radiation-hard detectors with excellent time resolution.

The detector requirements as dictated by the expected collision products are as follows:

- efficient muon identification, high momentum resolution, and unambiguous charge identification
- good charged particle momentum resolution and reconstruction efficiency
- precise vertex location for offline τ and b quark tagging
- efficient triggering
- high electromagnetic energy resolution
- wide geometric coverage
- reliable determination of missing transverse energy

A schematic view of the CMS detector is shown in figure 4.2. Central to CMS is a 4 T superconducting solenoid magnet that provides the bending power to measure the momentum of charged particles. Interior to the solenoid is the silicon-based tracking system; the lead-tungstate electromagnetic calorimeter (ECAL); and the lead and organic scintillator hadronic calorimeter (HCAL). Outside the magnet's bore are the muon tracking system made up of drift tubes, cathode strip chambers, and resistive plate chambers. These subsystems are described in detail in the following sections.

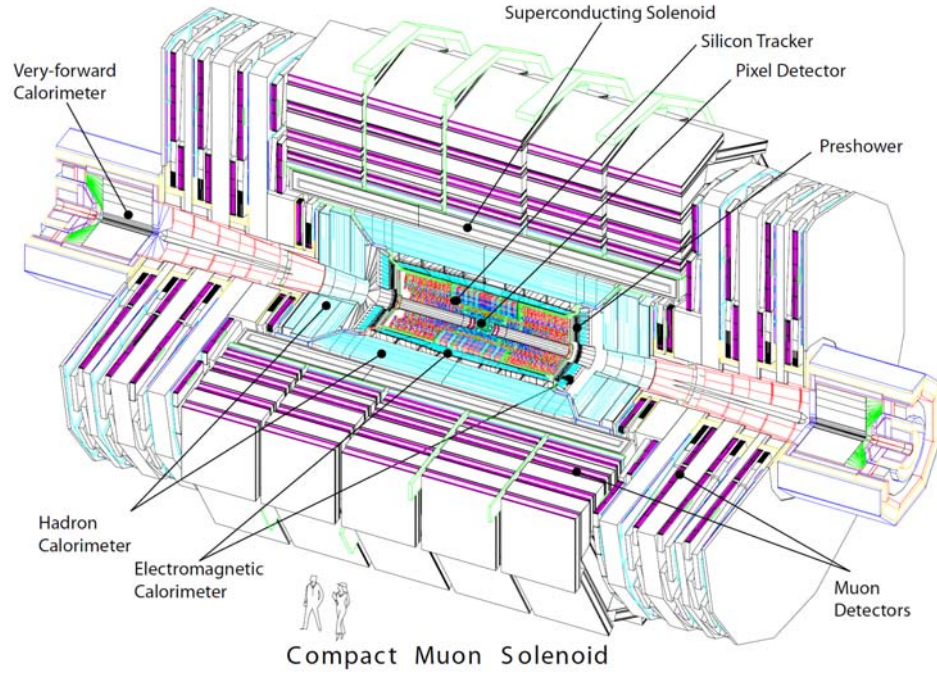


Figure 4.2. Schematic view of the CMS detector showing the various sub-detectors.

4.2.1. Superconducting Magnet

The superconducting magnet is designed to maintain a 4 T field with a stored energy of 2.6 GJ at full current. It is a 220 t solenoid with dimensions of 6 m in diameter and 12.5 m in length. Of note is the 4-layer winding made from reinforced NbTi Rutherford-type cable which is cooled to 4.5 K using liquid He. The iron return yoke is composed of 6 endcap disks and 5 barrel wheels which also serve to house the muon tracking system.

4.2.2. Tracker

The inner tracking system facilitates precise and efficient determination of the trajectories of charged particles as well as identification of secondary vertices from the decay of longer lived particles and photon conversions to electron-positron pairs. It is designed to handle an expected average of 1000 particles produced every bunch crossing (400 MHz). The subsystem (shown in figure 4.3) is composed of two different components: the innermost layers consisting of silicon pixels for vertex determination and the outer layers composed of silicon strips for measuring particle trajectories and momenta. The physical dimensions of the detector system results in a coverage up to $|\eta| < 2.5$.

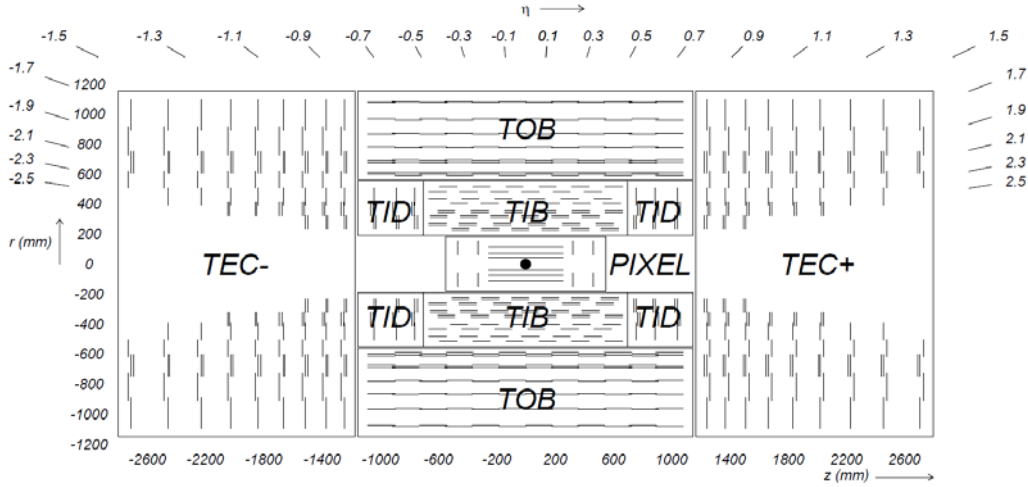


Figure 4.3. Schematic side-view of the CMS silicon tracker.

The pixel detector has a total of 66 million $100 \times 150 \mu\text{m}^2$ silicon pixels spread over three barrel layers and two endcap disks, resulting in an active area of about 1 m^2 and spatial resolution on the order of $15 - 20 \mu\text{m}$. The strips range in size between $10 \text{ cm} \times 80 \mu\text{m}$ nearest the beam line to $25 \text{ cm} \times 180 \mu\text{m}$ in the outer parts of the detector. The total active area of the silicon tracking detector is more than 205 m^2 .

The measurement resolution of the transverse momentum of charged tracks at around 100 GeV is $\approx 2\%$. The track reconstruction efficiency is near 100% for muons over the full extent of the detector acceptance, but less for pions (75-95% depending on the particle p_T and η) due to higher interaction with non-detecting material in the tracker. The momentum and vertex resolution is shown in figure 4.4 as a function of η . A more detailed description of the tracker performance can be found in [36].

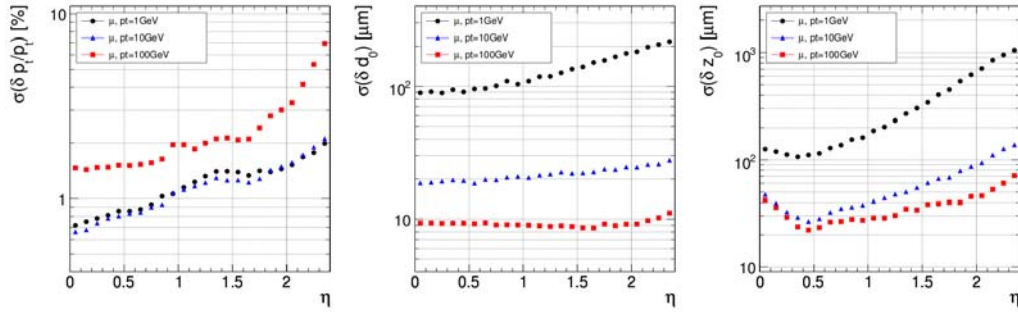


Figure 4.4. CMS tracker resolution performance for single muons [?] as a function of η for three different charged particle momenta. Resolution for transverse momentum (left), transverse vertex resolution (center), and longitudinal vertex resolution (right) are shown.

4.2.3. Electromagnetic Calorimeter

One of the most prominent search channels for the detection of the Higgs boson is when it decays to two high-energy photons. This motivates the need for excellent energy resolution of the CMS ECAL (shown in figure 4.5). To achieve this, lead tungstate (PbWO_4) crystals are used as the active material. The characteristics that make this material an ideal choice for a high-granularity, compact detector are its high density (8.28 g/cm^3), short radiation length (0.89 cm) and small Molière radius (2.2 cm). Additionally, the material is radiation

hard and has a scintillation decay time such that 80% of the light is emitted in the time between bunch crossings (25 ns).

The ECAL is split into barrel and endcap sections. The barrel section covers $|\eta| < 1.44$ and is composed of 61,200 crystals while the endcap covers $1.56 < |\eta| < 3.0$ and contains 14,846 crystals. The longitudinal dimensions of the crystals corresponds to 25.8 radiation lengths in the barrel and 24.7 radiation lengths in the endcap.

To better discriminate against signals arising from neutral pions and improve the position determination of electrons and photons, a sampling calorimeter is placed before the ECAL endcap. The so-called Preshower covers a range of $1.65 < |\eta| < 2.6$ and functions by a layer of lead radiators initiating electromagnetic showers which subsequently traverse a layer of silicon strip detectors that measure the deposited energy and characterize the transverse shower profiles.

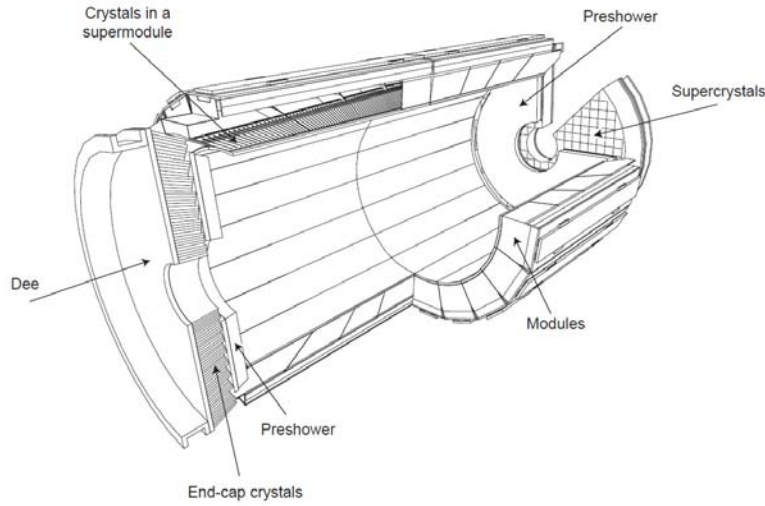


Figure 4.5. Schematic view of the CMS ECAL.

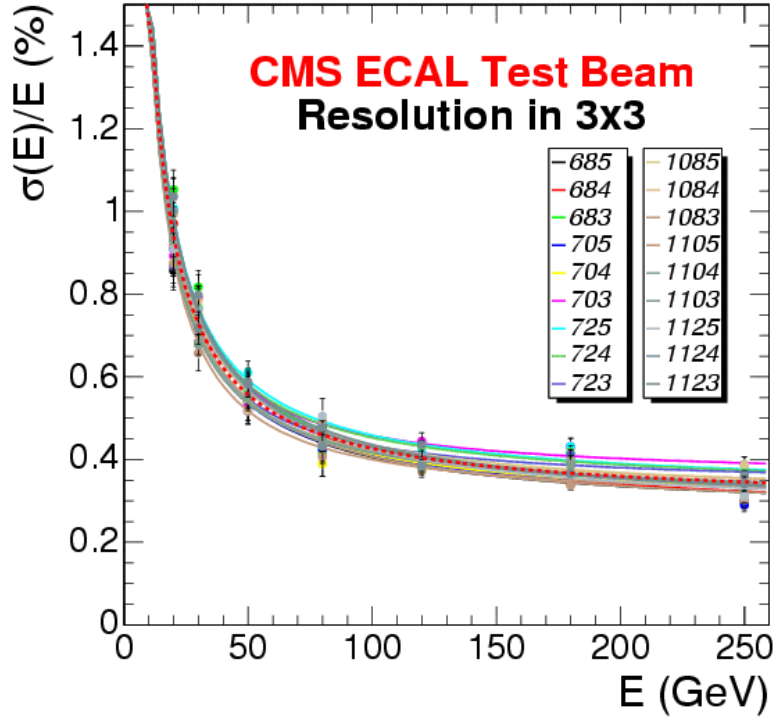


Figure 4.6. Energy resolution of the ECAL as a function of beam energy from electron test beam measurements.

As the energy of the particle traversing the ECAL increases beyond 500 GeV, a significant portion of the shower can leak out the rear of the calorimeter. For energies below this, the energy resolution can be parameterized as follows:

$$(4.1) \quad \left(\frac{\sigma}{E}\right)^2 = \left(\frac{S}{\sqrt{E}}\right)^2 + \left(\frac{N}{E}\right)^2 + C,$$

where the S (2.8%) term represents stochastic effects, the N (12%) term accounts for the effect from noise, and C (0.3%) is a constant term [37]. The resolution performance in the barrel as determined during 2007 test beam is shown in figure 4.6.

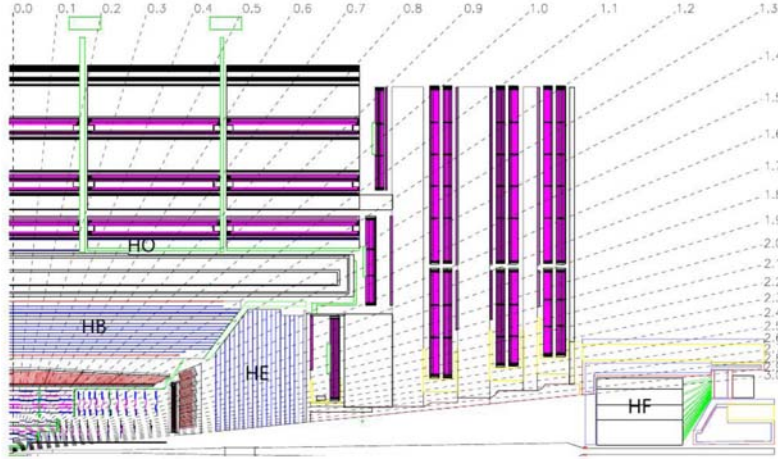


Figure 4.7. Schematic side-view of the CMS HCAL.

4.2.4. Hadronic Calorimeter

The HCAL is of particular use in measurement of hadron jets and determination of missing transverse energy arising from neutrinos or exotic particles. It consists of several components: nested between the ECAL and the magnet is the hadronic calorimeter (HCAL) barrel ($|\eta| < 1.3$) and ($1.3 < |\eta| < 3.0$) endcap; outside the magnet's bore is a tail catcher; and at high pseudorapidity ($|\eta| > 3$) is the forward hadronic calorimeter (HF). A longitudinal schematic of the HCAL is shown in figure 4.7.

The barrel, endcap, and tailcatcher are composed of alternating layers of brass and scintillating tiles. As is the case with sampling calorimeters, not all energy is measured directly in the scintillating tiles so that energy deposited in the brass must be inferred. The barrel (HB) and endcap (HE) sections are transversely segmented in 72×32 and 72×26 towers, respectively, in the $\phi \times \eta$ plane.

The construction of HF differs from the rest of HCAL to account for its forward location where there is a much higher particle flux. It is also a sampling calorimeter, but

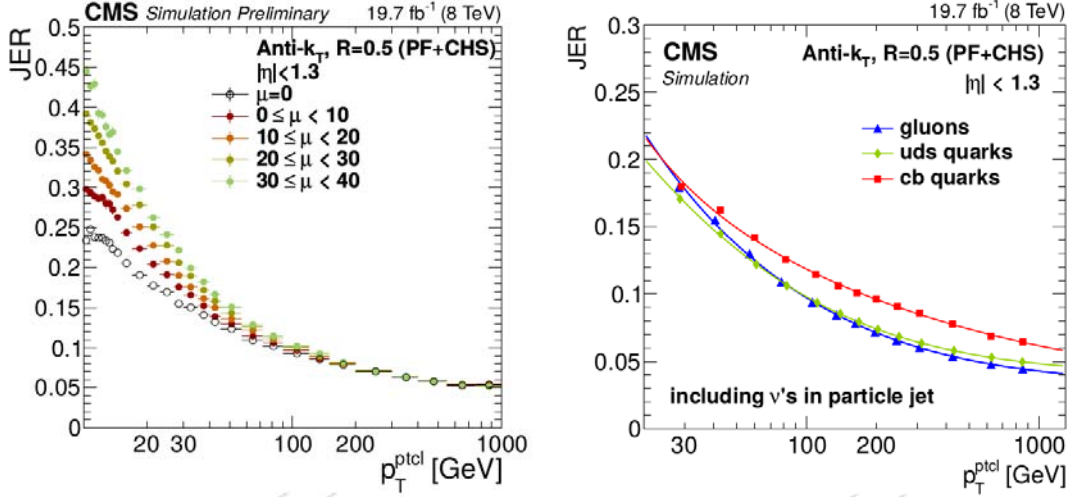


Figure 4.8. Jet transverse momentum resolution as a function of p_T for different pileup scenarios (left), and for different jet compositions (right), as measured in 2012 data.

uses steel plates as an absorber and quartz fibers as the active medium. A crude particle identification can be achieved through the use of short and long fibers, i.e., particles that penetrate deeper (hadrons) into the material will interact with both type of fibers whereas particles that only penetrate slightly (electromagnetically interacting) will only interact with the long fibers.

The jet energy resolution based on $\sqrt{s} = 7\text{TeV}$ data collected in 2011 [38] (the 2012 study is still ongoing) for both central and forward jets is shown in figure 4.8. The resolution of MET during the 2012 run [39] is shown in figure 4.9. Though hadronic jets and MET are reconstructed using information from all of the CMS subdetectors, the accuracy of the measurement of both jet energy and MET are very strongly dependent on the performance of HCAL.

Figure 4.8 shows the jet energy resolution for the two both central and extremely forward jets [38]. Although the jet energy determination pulls information from all of

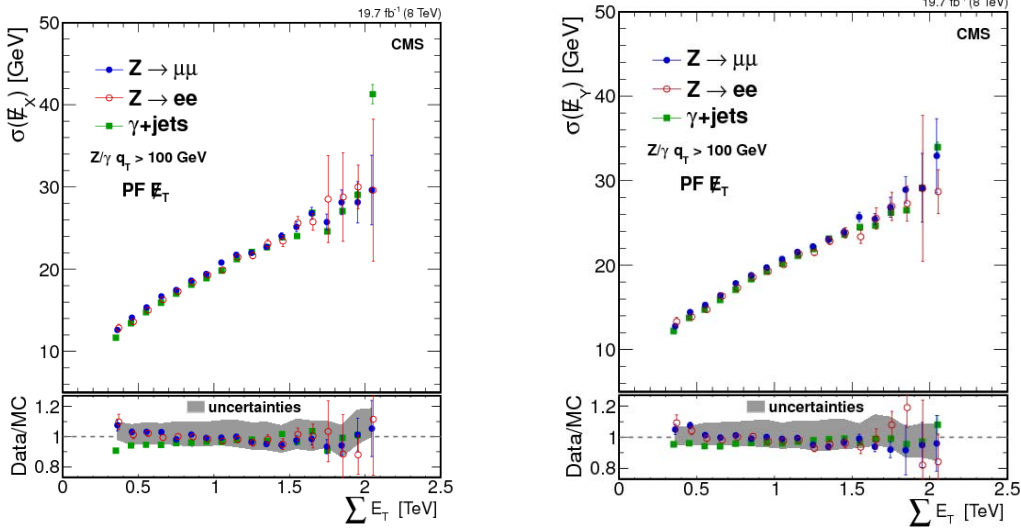


Figure 4.9. MET resolution measured in Z/γ events. The MET is projected either in the direction parallel (left) to the direction of the reconstructed Z/γ or perpendicular (right).

the subdetectors, the performance of the HCAL weighs heavily in the final resolution obtainable for hadron jets in CMS.

4.2.5. Muon Detectors

The muon subsystem is designed with the singular purpose of aiding in the identification and momentum determination of muons. This is largely motivated by the expectation of very high sensitivity to a SM Higgs boson decaying to Z boson pairs which subsequently decay to four leptons. Of particular importance is the fact that the best 4-particle mass resolution can be achieved in the case that all four leptons are muons.

The subsystem is comprised of three distinct types of tracking detectors. These are drift tube (DTs) which are located in the barrel region ($|\eta| < 1.2$); cathode strip chambers (CSCs) which extend ($0.9 < |\eta| < 2.4$); and resistive plate chambers (RPCs) that overlap

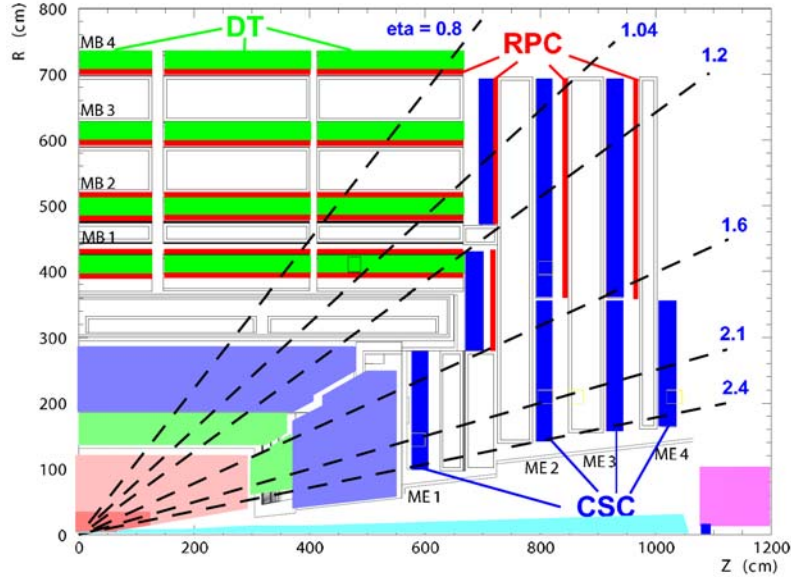


Figure 4.10. Schematic side-view of the CMS Muon detectors.

with the other two muon detectors in the region of $|\eta| < 1.6$. A schematic rendering of the system is shown in figure 4.10.

The DT system consists of four concentric cylindrical layers of chambers, interspersed between layers of the iron magnetic return yoke. In total there are 172,000 sensitive wires dispersed throughout the chambers which are contained in superlayers of partially overlapping drift cells. The wires are alternately oriented either parallel or perpendicular to the beam direction depending on the distance from the beam line in order to ensure precise resolution of the muon's η and ϕ coordinates.

The CSC system is composed of multi-wire proportional chambers of 6 anode wire planes interleaved among 7 cathode panels. Both the wires and the cathode strips are used to determine the position measurement of an incident muon. The wires also serve to properly assign events to the corresponding bunch crossing in the LHC, as they have timing resolution within the 25 ns needed to do this properly. The strips are read out

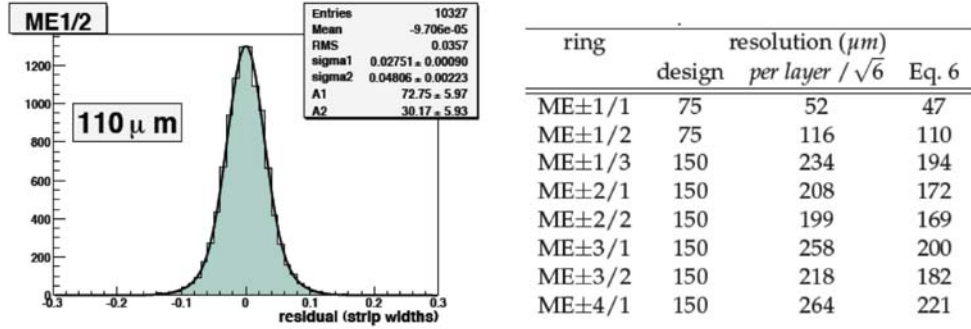


Figure 4.11. (Left) Residuals of reconstructed hits on the CSC strips in cosmic ray data. Expected position is acquired using a fit to the other 5 layers of the same CSC chamber. (Right) Summary of resolutions obtained for each chamber type compared to the design expectation.

preserving the measurement of total charge induced on the incident strip, as well as on neighboring strips which can be used to estimate azimuthal position with high precision. Given that muons are mostly deflected in the azimuthal direction, this ensures accurate determination of the muon momentum. Figure 4.11 shows a summary of a study the CSC spatial resolution based on CRAFT data [40].

4.2.6. Trigger

The 40 MHz rate of collisions at the LHC exceeds the limitations for writing out the data and storing on tape. This necessitates a reduction of the amount of data that actually needs to be processed. To address these constraints, CMS employs a two-tier trigger system.

The initial filtering of data, the so-called Level-1 Trigger (L1T), is hardware based and accepts events based on an approximation of physical quantities (for example, the amount of energy measured in the calorimeter system). This step reduces the rate down to 100 kHz. The next step, known as the High-Level Trigger (HLT), is software-based, and

uses a complete physics reconstruction that is as close to what is used for offline analyses as possible. After this step the rate is further reduced to the much more manageable rate of 100 Hz. The data is separated into different streams which are characterized by a set of reconstructed physics objects (leptons, jets, MET, etc.). Streams which have excessively high rates are further prescaled so that only a portion of the events passing the HLT are recorded to tape.

4.2.7. Area of Expertise

The LHC and the associated experiments are the result of the combined efforts of thousands of physicists and engineers. It is therefore of some value to draw a distinction between this author's contributions and the rest of the collaborators who have contributed to the design, construction, maintenance, and successful operation of the device. In consideration of this, this section provides a brief outline of the author's technical contributions. These can be summarized as,

- data quality monitoring shifter (summer 2009)
- maintenance of HCAL conditions database
- development of tau triggers for Higgs analyses
- on-call shifter for beam and radiation monitoring group
- development of luminosity measurement using the fast beams condition monitor (BCM1F) [41, 42]

The last item lead to a parallel talk being delivered at the 2012 International Conference for High Energy Physics in Melbourne, Australia. The proceedings from the talk are included in appendix B.

CHAPTER 5

Analysis

5.1. Datasets

This analysis uses 19.7 fb^{-1} of data collected at $\sqrt{s} = 8 \text{ TeV}$. To optimally select on multilepton events, several trigger streams are used that require the presence of two or more leptons in the final state.

5.1.1. Data Samples

Datasets used in this analysis come from trigger streams that require the identification of at least two leptons where the leptons are either muons or electrons. The datasets and their corresponding luminosities are listed in table 5.1. This data was reprocessed in early 2013 to correct for machine conditions that were not known at the time of acquisition.

The luminosity is determined by counting clusters of hits in the silicon pixel detector [43]. The value of the luminosity used in the analysis takes into consideration the triggers used and excludes runs that are not centrally certified, i.e., have some critical issue which makes the data unreliable.

Triggers are defined so as to have the lowest possible thresholds on the leptons' momentum and identification without being prescaled. These triggers require that there be at least two leptons (electrons or muons) reconstructed at the HLT where one of the leptons must have $p_T > 17 \text{ GeV}$ and the other must have $p_T > 8 \text{ GeV}$. Muons have

Dataset	Run Range	Integrated Luminosity (fb^{-1})
DoubleMu(Parked)	190645 - 208686	19.71
Run2012A	190456-190949	0.875
Run2012B	193834-196531	4.402
Run2012C	198022-203746	7.114
Run2012D	203768-208686	7.318
DoubleElectron	190645 - 208686	19.74
Run2012A	190456-190949	0.889
Run2012B	193834-196531	4.399
Run2012C	198022-203746	7.132
Run2012D	203768-208686	7.318
MuEG	190645 - 208686	19.78
Run2012A	190456-190949	0.8894
Run2012B	193834-196531	4.429
Run2012C	198022-203746	7.152
Run2012D	203768-208686	7.309

Table 5.1. 2012 datasets: individual luminosities are determined based on a luminosity mask that is based on events that are processed. The datasets were gathered over the course of 2012 and reprocessed in January 2013.

no identification requirements, but the electrons are required to pass both identification and isolation requirements based on detector information from the calorimeters and the tracker.

Triggers are emulated in the simulated MC samples. Events that fail to pass the listed triggers are discarded in both data and MC. The efficiency for a given event to pass the trigger selection differs between data and MC which is accounted for by applying scale factors. This is only done for the case of same-sign dileptons because in the case where there are three leptons in the final state it is expected that the triggers to be near 100% efficient. Scale factors for double muon triggers are provided by the muon POG; double electron trigger scale factors are taken from [44]. Parametrization of the muon trigger

Ele17	$ \eta < 1.4442$	$1.4442 < \eta < 1.566$	$ \eta > 1.566$
$20 < p_t < 30$	0.9863	0.9664	0.9892
$30 < p_T < 40$	0.9910	0.9645	0.9965
$40 < p_T < 50$	0.9920	0.9752	0.9991
$50 < p_T$	0.9933	0.9868	0.9998
Ele8	$ \eta < 1.4442$	$1.4442 < \eta < 1.566$	$ \eta > 1.566$
$10 < p_T < 15$	0.9085	0.9493	0.9010
$15 < p_T < 20$	0.9750	1.0459	0.9715
$20 < p_t < 30$	0.9869	1.0033	0.9966
$30 < p_T < 40$	0.9908	0.9929	0.9954
$40 < p_T < 50$	0.9914	0.9940	0.9977
$50 < p_T$	0.9929	0.9944	0.9979

Table 5.2. Trigger efficiency scale factors between data and MC for HLT_Ele17_Ele8 for leading (top) and trailing (bottom) legs.

scale factors are shown in 5.5. Electron scale factors are shown in table 5.2. Events passing the muEG triggers do not have any corrections applied.

Since there can be significant overlap between the three data streams (double muon, double electron, and combined muon plus electron), the following scheme is followed to avoid double counting events in data:

- **double muon:** this data is given highest priority, and events are selected from it based on whether they pass the double muon triggers;
- **double electron:** this data is given secondary priority, and events are selected if they pass the double electron triggers but fail to pass the double muon triggers;
- **muon plus electron:** this data is given lowest priority, and events are selected if they pass the muEG triggers but fail to pass both the double muon and double electron triggers.

5.1.2. Signal Samples

FCNH signal samples were generated using the PYTHIA [45] Monte Carlo generator with Tune Z2 and CTEQ6 [46]. The Higgs boson is assumed to be chargeless with spin 0 and have a mass of 125 GeV. The Higgs boson is allowed to decay to WW ($\mathcal{B}(H \rightarrow WW) = 0.215$), ZZ ($\mathcal{B}(H \rightarrow ZZ) = 0.026$), and $\tau\tau$ ($\mathcal{B}(H \rightarrow \tau\tau) = 0.063$) final states [47]. Throughout this analysis, a $\mathcal{B}(t \rightarrow Hc) = 0.01$ is assumed unless explicitly stated otherwise. The value of the $t\bar{t}$ cross-section is assumed to be 252 pb [19].

5.1.3. Background Samples

Backgrounds for the final states under consideration use simulated samples produced during the Summer 2012 MC generation campaign. These samples are generated using either MADGRAPH [48], POWHEG [49] or PYTHIA. PYTHIA is also used to handle parton showering for events generated with MADGRAPH or POWHEG. A complete set of background samples is listed in table 5.3.

Simulated events are reweighted based on the number of hard interactions per event (pileup). The motivation for this is described in the following section.

5.1.4. MC Pileup Reweighting

Throughout 2012 data-taking, the instantaneous luminosity of the LHC was increased from approximately 5×10^{-34} to 8×10^{-34} cm s⁻¹. This results in a moderate variation in the amount of pileup (about 25 to 35 interactions per bunch crossing). In order to match the pileup distribution in MC to the distribution observed in data, the MC is reweighted so that the multiplicity of simulated vertices matches the measured pile-up

Process	Generator	$\sigma \times \text{BR}(pb)$
μ -enriched QCD $p_T > 20 \text{ GeV}$	PYTHIA (Tune Z2)	84679
e -enriched QCD $20 < p_T < 30 \text{ GeV}$	PYTHIA (Tune Z2)	2920632
$30 < p_T < 80 \text{ GeV}$	PYTHIA (Tune Z2)	4615893
$80 < p_T < 170 \text{ GeV}$	PYTHIA (Tune Z2)	183722
$170 < p_T < 250 \text{ GeV}$	PYTHIA (Tune Z2)	4588
$250 < p_T < 350 \text{ GeV}$	PYTHIA (Tune Z2)	556.75
$350 > p_T \text{ GeV}$	PYTHIA (Tune Z2)	89.1
$t\bar{t}$	MADGRAPH +TAUOLA	234
tW	POWHEG +TAUOLA	11.77
$\bar{t} W$	POWHEG +TAUOLA	11.77
t (t channel)	POWHEG +TAUOLA	55.53
\bar{t} (t channel)	POWHEG +TAUOLA	30.7
$t\bar{t} W$	MADGRAPH	0.232
$t\bar{t} Z$	MADGRAPH	0.206
$t\bar{t} \gamma$	MADGRAPH	2.166
$Z/\gamma^* \rightarrow \ell\ell$ $10 < m_{\ell\ell} < 50 \text{ GeV}$	MADGRAPH	860.5
$m_{\ell\ell} > 50 \text{ GeV}$	MADGRAPH	3532.8
$WW \rightarrow 2\ell 2\nu$	MADGRAPH +TAUOLA	5.995
$WZ \rightarrow 3\ell\nu$	MADGRAPH +TAUOLA	1.058
$ZZ \rightarrow 2\ell 2\nu$	MADGRAPH +TAUOLA	0.365
$ZZ \rightarrow 2\ell 2j$	MADGRAPH +TAUOLA	1.28
$ZZ \rightarrow 4e$	POWHEG +PYTHIA	0.0769
$ZZ \rightarrow 4\mu$	POWHEG +PYTHIA	0.0769
$ZZ \rightarrow 4\tau$	POWHEG +PYTHIA	0.0769
WWW	MADGRAPH	0.0822
WWG	MADGRAPH	0.528
WWZ	MADGRAPH	0.0633
WZZ	MADGRAPH	0.0192
ZZZ	MADGRAPH	0.00459

Table 5.3. Simulated MC samples used in the analysis. All samples are from the production Summer12_DR53X-PU_S10_START53_V7A-v*/AODSIM tier data.

distribution observed in data. A comparison of the pileup multiplicity distribution from the S10 pile-up scheme and the distribution measured from data are shown in figure 5.1. As a validation of the weighting procedure a comparison of the primary vertex multiplicity in data and MC after weighting is shown in figure 5.2. Though there is some divergence in the tails of the pileup distribution for dilepton events, the signal region has reduced statistics and therefore only samples from the core of the distribution where agreement is good.

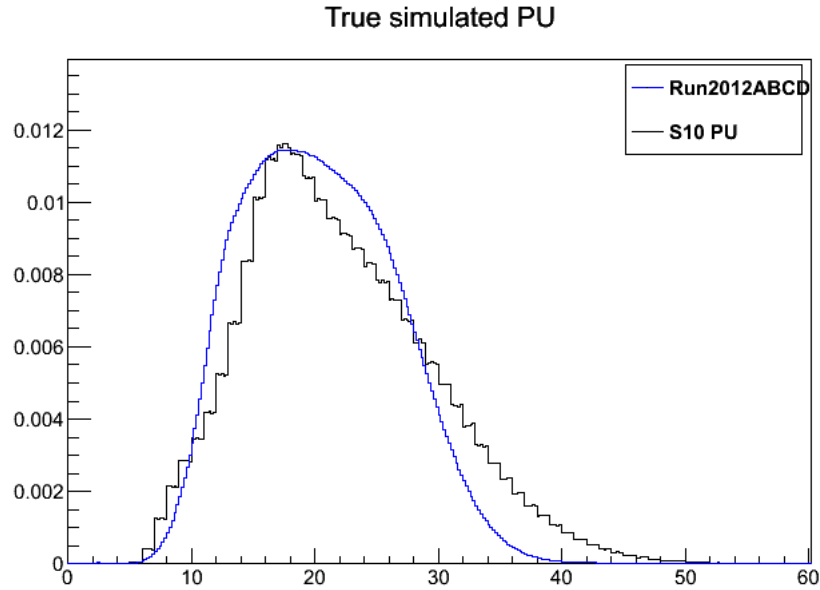


Figure 5.1. Comparison of pileup distributions for 19.7 fb^{-1} of data taken at 8 TeV and simulation with S10 pileup scheme.

5.2. Object selection

The topology of interest involves final states with two or three isolated leptons, MET, and at least two jets. In this section, the reconstruction and selection of these objects is described.

5.2.1. Primary Vertex

Primary vertices (PV) are reconstructed based on information from the tracking subsystem, mainly through the inner pixel detector. Quality cuts are applied to reconstructed PVs to guarantee they come from a proton-proton hard scattering event. These cuts are as follows,

- nDOF of fit > 4 ;
- $|z| < 24$ cm;
- $\sqrt{x^2 + y^2} < 2$ cm.

The PVs are ordered based on the sum p_T of tracks used in their reconstruction. Selected physics objects are associated to the PV with the greatest sum p_T .

5.2.2. Leptons

A description of the reconstruction and identification of muons and electrons (taus are only considered implicitly when they decay to lighter leptons) is presented in this section. The lepton multiplicity (without efficiency corrections) observed in the double lepton data streams and a comparison to the MC prediction is shown in figure 5.3. The efficiency-corrected rate for different dilepton and trilepton final states after the preselection (see section 5.3.1) is shown in figure 5.4.

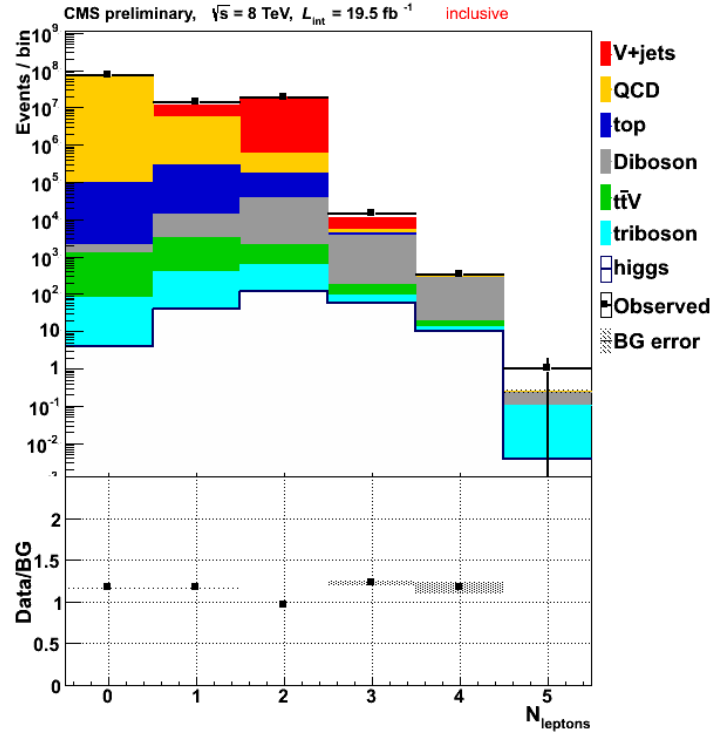


Figure 5.3. Multiplicity of leptons after selection of triggers and lepton identification (efficiency corrections are not applied). Uncertainties are statistical only and all background estimates are done with MC.

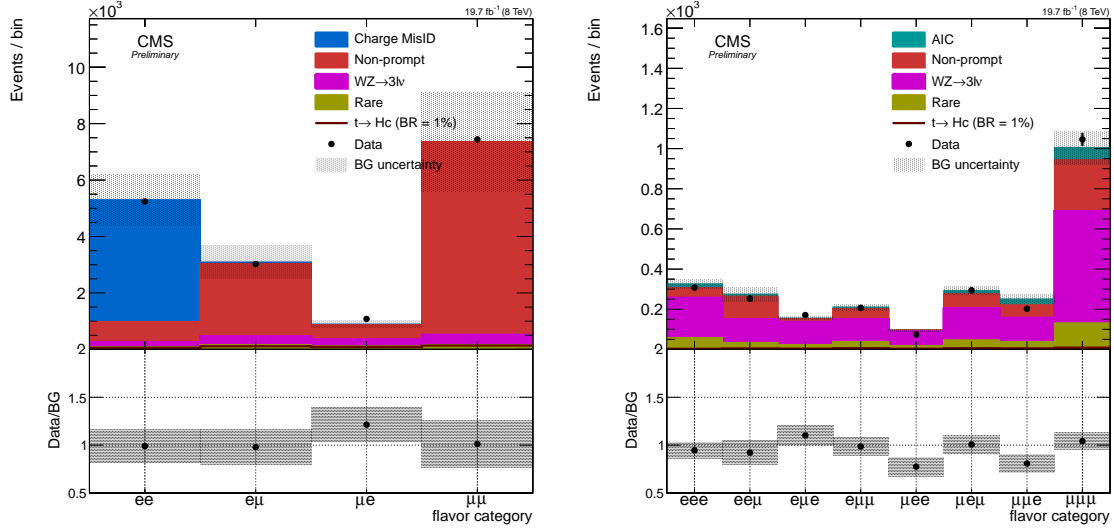


Figure 5.4. Number of events for in same-sign dilepton (left) and trilepton events by flavor category are shown. Lepton preselection (see section 5.3.1) is applied.

5.2.2.1. Muons. Muons candidates are reconstructed using both the CMS muon system and the tracker. The coverage of these two detector systems allows reconstruction within $|\eta| < 2.4$, and allows consideration of muons with p_T as low as 5 GeV [50].

Muons are required to be reconstructed using both the *global muon* and *tracker muon* reconstruction algorithms. These algorithms are distinct in that one begins with tracker information and extrapolates to find consistency with hits in the muons system (*tracker muons*), while the other (*global muon*) inverts the reconstruction steps starting from the muon system and finding tracks that are consistent. The combination of these two algorithms makes for a muon reconstruction that is accurate in predicting muon momentum and efficient in detecting muons within the detector acceptance.

In the interest of detecting muons decaying from vector bosons, a set of identification and isolation requirements are applied [51]. The identification requirements are defined so as to have high efficiency and a low probability of misidentifying muons originating from non-bosonic decays. They are listed here,

- *tracker* muon;
- *global* muon;
- *PF*muon;
- number of matched segments is greater than 1;
- $\chi^2/nDOF < 10$ for muon track fit;
- at least one valid hit in the muon chambers;
- at least one valid hit in the pixel detector;
- at least five track layers with measurements;
- a transverse impact parameter of $|d_0| < 0.015$ relative to the selected PV
- a longitudinal impact parameter of $|d_z| < 0.05$ cm relative to the selected PV.

To select on muons produced in the decay of vector bosons rather than those produced in association with the decay of heavy hadrons, the isolation of the muon is assessed by forming a cone of radius $\Delta R = \sqrt{\Delta\eta^2 + \Delta\phi^2} = 0.4$ about the muon candidate and summing the energy of particle flow (PF) candidates within the cone. This contribution from the various types of PF candidates is split into three types,

- charged hadron,
- neutral hadron,
- neutral electromagnetic (photons).

Additionally, the effect of energy deposited in the isolation cone as by-product of pileup interactions is considered. A combined PF-based relative isolation that is corrected for pileup ($\Delta\beta$) is defined as follows,

$$(5.1) \quad Iso_{comb} = \frac{Iso_{chargedhadron} + Max(0, Iso_{neutralhadron} + Iso_{photon} - 0.5\Delta\beta)}{p_T}.$$

The recommended cut quantity is used and is required to be less than 0.12.

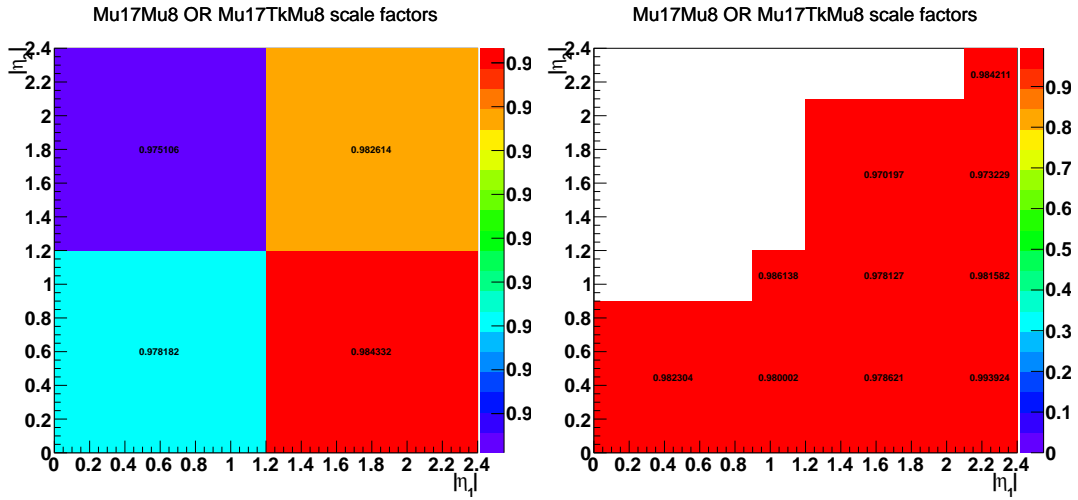


Figure 5.5. Scale factors for muon trigger efficiency between data and simulation. The scale factors are done in two bins of muon p_T : $10 \text{ GeV} < p_T < 20 \text{ GeV}$ (left) and $p_T > 20 \text{ GeV}$.

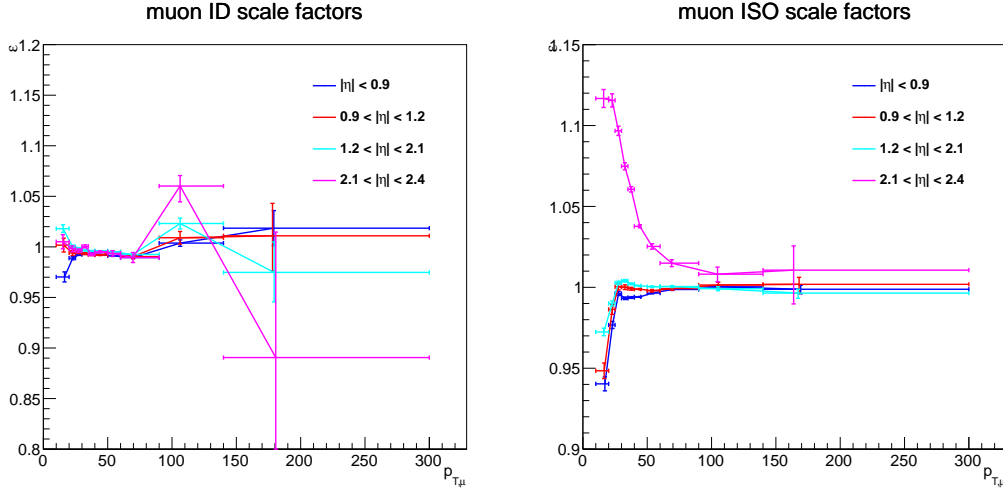


Figure 5.6. Scale factors for muon identification (left) and isolation (right) efficiency between data and simulation.

The muon momentum scale is corrected using the Rochester corrections. These corrections are derived using a method based on binned parametrization of data and MC momentum bias and resolution using $Z \rightarrow \mu\mu$ invariant mass distributions. There are also corrections applied to account for differences between trigger efficiency, identification, and isolation of muons in data and MC simulation. These are shown in figures 5.5 and 5.6.

5.2.2.2. Electrons. Electrons are reconstructed by combining information from the electromagnetic calorimeter and the tracking system. In this analysis, electrons reconstructed using the gaussian-sum filter (GSF) are used [52]. Corrections are applied to account for mismeasurement of electron momentum.

Electron identification is performed by using a boosted decision tree (BDT) that combines various parameters describing the shower shape in the calorimeter and tracking information. The weight files and cut values are centrally prepared [53]. The following

selection cuts are used based on the assumption of analysis electrons having fired the trigger,

- $10 < p_T < 20$ GeV:
 - $0 < |\eta| < 0.8 : \text{BDT} > 0.0$
 - $0.8 < |\eta| < 1.479 : \text{BDT} > 0.1$
 - $1.479 < |\eta| < 2.5 : \text{BDT} > 0.62$
- $p_T > 20$ GeV:
 - $0 < |\eta| < 0.8 : \text{BDT} > 0.94$
 - $0.8 < |\eta| < 1.479 : \text{BDT} > 0.85$
 - $1.479 < |\eta| < 2.5 : \text{BDT} > 0.92$

Additionally, there are several pre-MVA cuts applied,

- $|\eta| < 2.5$
- no missing hits
- conversion veto
- a transverse impact parameter of $|d_0| < 0.005$ relative to the selected PV
- a longitudinal impact parameter of $|d_z| < 0.05$ cm relative to the selected PV.

The transverse impact parameter was tightened from 0.015 cm to 0.005 cm to reduce the probability of mismeasuring the charge of the electron. This is explained further in section 5.4.4.

The isolation is performed in similar manner to the muons, but the relative combined PF isolation is required to be less than 0.15 for the tight electrons, and the so-called ρ corrections are used for the pileup correction,

$$(5.2) \quad Iso_{comb} = \frac{Iso_{chargedhadron} + \text{Max}(0, Iso_{neutralhadron} + Iso_{photon} - \rho \times A_{eff})}{p_T}.$$

There are additional corrections applied, as in the muon case, to account for differences in the efficiency of correctly identifying an electron in data and simulation. These scale factors are applied to MC events according to the p_T and η of the electron candidate. The two-dimensional distribution of scale factors are shown in figure 5.7.

In events where there is clear overlap between a muon and an electron (see figure 5.8), precedence is given to identifying the object as a muon. This is done by vetoing any electron within $\Delta R < 0.1$ of a muon passing all of the identification and isolation requirements described in the previous section.

5.2.3. Photons

Photons are used in a limited context within the scope of this analysis. The sole use is in the estimation of background due to assymetric internal conversions described in section 5.4.2. The photons are reconstructed by clustering energy deposits in the cells of the electromagnetic calorimeter (ECAL) into so-called SuperClusters. To ensure a pure sample of dilepton plus photon events, the tight POG recommendation is used of the photon identification and isolation. This entails the following requirements:

- conversion veto
- $\sigma_{i\eta i\eta} < 0.01(0.028)$,
- Hadronic over EM fraction $< 0.05(0.065)$,
- no overlap with analysis muons or electrons ($\Delta R(\ell, \gamma) > 0.1$),

- $\text{ISO}_{\text{charged},\rho\text{-corrected}} < 1.5(1.2),$
- $\text{ISO}_{\text{neutral},\rho\text{-corrected}} < 1.0(1.5) + 0.04 \times p_{\text{T}},$
- $\text{ISO}_{\text{photon},\rho\text{-corrected}} < 0.7(1.0) + 0.005 \times p_{\text{T}},$

where parenthetical values denote the number used for the endcap ($|\eta| > 1.556$) and the isolation is corrected for pileup using the rho parameter, i.e.,

$$(5.3) \quad \text{ISO}_{\rho\text{-corrected}} = \text{ISO} - \rho \times A_{\text{effective}}.$$

The effective area is calculated based on the location of the photon super cluster in the detector, and what isolation type is being corrected (charged, neutral, or photon). The photon is allowed to have a p_{T} as low as 10 GeV and is required to have $|\eta| < 2.4$.

Because the photon is only used as a proxy for a conversion and is therefore used to model what is a final state lepton in the observed data, corrections for efficiencies and energy mismeasurement are not applied.

5.2.4. Jets

Jets are reconstructed from PF candidates [54]. PF candidates combine information from all of the detector subsystems to facilitate the reconstruction and identification of individual particles. These PF candidates are clustered using the anti- k_{T} algorithm [55] with a cone size of $\Delta R = 0.5$. Once reconstructed, a number of corrections are applied to the jets to correct for pileup contamination, differing absolute response in jet p_{T} , and relative response in η [56]. To reduce contamination from photons and prompt leptons, several ID requirements are placed on the jets,

- number of constituents > 1 ,
- charged hadronic fraction > 0 ,
- charged EM fraction < 0.99 ,
- neutral hadronic fraction < 0.9 ,
- neutral EM fraction < 0.9 ,
- at least one charged constituent.

In addition to the above requirements, it is required that all jets have $p_T > 30$ GeV and $|\eta| < 2.5$. Multiplicities of all jets passing the tight ID requirements and kinematic cuts are shown in figure 5.9.

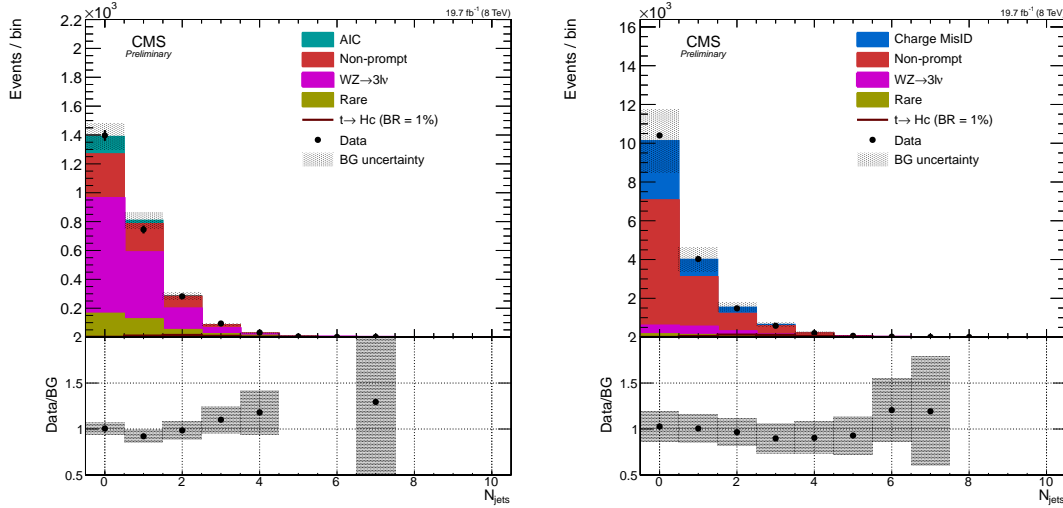


Figure 5.9. Multiplicity of jets in three lepton (left) and same-sign dilepton events (right) at the preselection level.

5.2.4.1. b-tagging. The identification of jets originating from the decay of b quarks is an important part of any analysis involving top quarks. The combined secondary vertex (CSV) b-tagging algorithm [57] is used to optimize the efficiency for identifying b-jets

while reducing the fake rate from light flavor jets. In this analysis, the recommended medium working point ($\text{CSV} > 0.679$) supplied by the b-tag POG is used. According to performance estimates, this results in a 70% b-tagging efficiency and 1.5% mistagging efficiency.

Scale factors are applied to correct for differences between b-tag efficiency and fake rates in data and MC. The approach adopted here relies on promoting or demoting the b-tag status of a given jet based on the b-tagging efficiencies measured in both data and simulation. Scale factors are centrally produced and validated. The mistag rate and efficiencies for b-tagging in MC are determined by considering the flavor content of a jet from MC truth. The measurement considers the efficiency of jets associated to bottom or charm quarks to pass the b-tag working point as well as the efficiency for jets associated to gluons or light quarks (usd) to pass the b-tagging requirement. The result of these measurements are shown in figure 5.10.

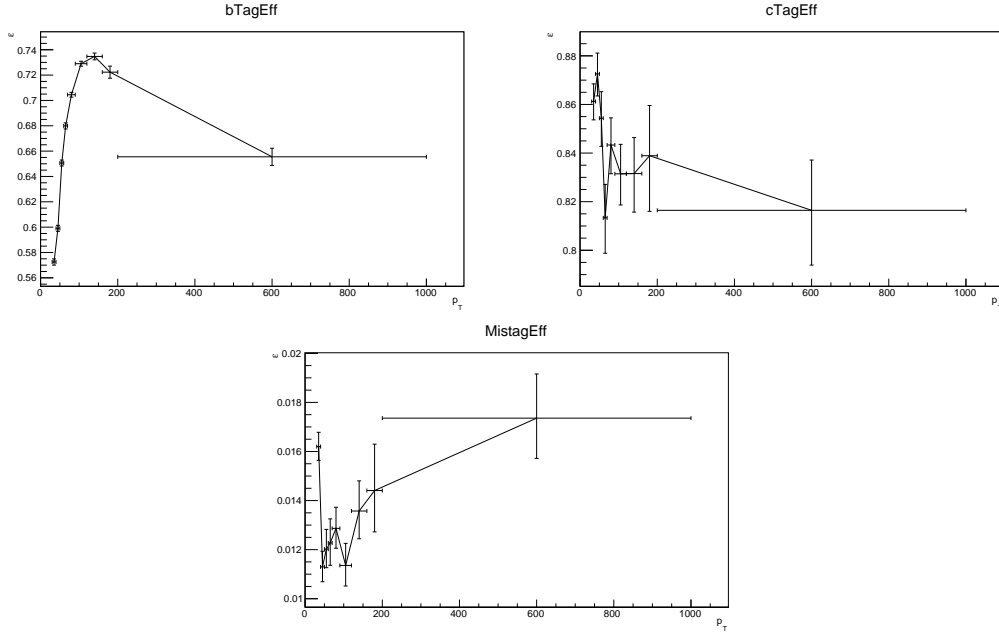


Figure 5.10. Efficiencies measured from MC for jets associated to b quarks (left), c quarks (middle), and light quarks or gluons (right) to pass CSV medium working point.

Depending on the value of the scale factor and the MC-truth flavor of a jet, a probability of being promoted or demoted is assigned. If $SF < 1$, then b-tagged jets can be demoted with a probability,

$$(5.4) \quad f = 1 - SF,$$

whereas if $SF > 1$, there is a probability of promoting an untagged jet to a b-tagged jet with a probability,

$$(5.5) \quad f = \frac{1 - SF}{1 - 1/\varepsilon_{MC}}.$$

The case that a jet is identified with a charm quark is also taken into consideration. This is done by measuring the b-tag efficiency of charm jets in MC for the m

The b-jet multiplicity at preselection level after applying corrections for the trilepton and same-sign dilepton selections are shown in figure 5.11.

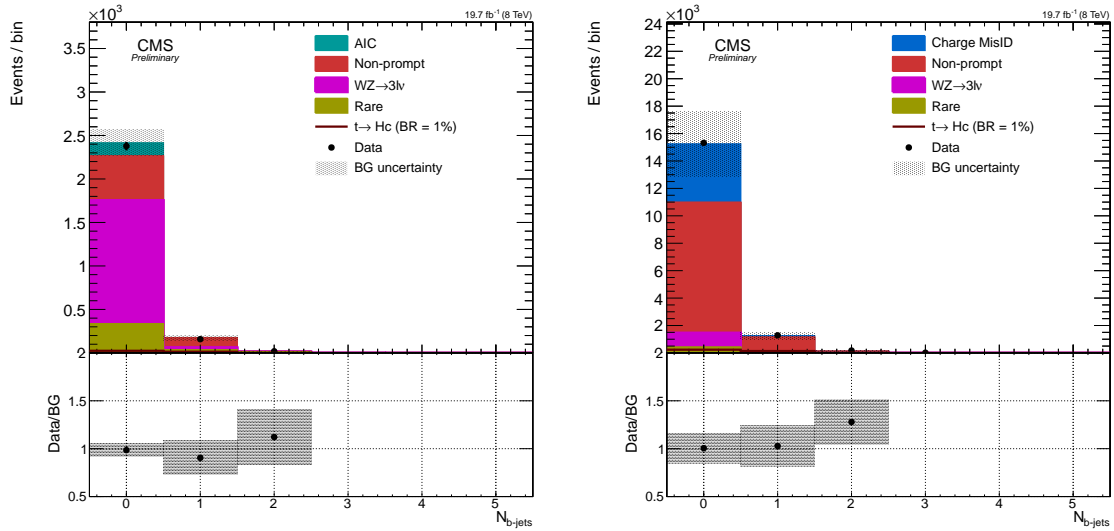


Figure 5.11. Multiplicity of b-jets passing medium CSV working point in three lepton (left) and same-sign dilepton events (right) at the preselection level.

5.2.5. Missing Transverse Energy

Missing transverse energy (MET) is reconstructed by summing the transverse energy of all reconstructed PF candidates in the event. Corrections that are applied to jets

are propagated through to the MET. Examples of the MET distributions are shown in figure 5.12. There is a known issue with the modeling of MET resolution in the simulation. One approach to correct for this is to propagate a smearing on the jet energy measurement to the MET. Because this analysis ultimately is interested in high MET events and will model the contribution from low MET processes from data, such an approach is not pursued in the current scope.

5.3. Event selection

In this section, the criteria for event selection is outlined. Focus is placed on events having either two same-sign leptons or three leptons with tau leptons being considered implicitly where they decay to either muons or electrons.

5.3.1. Preselection

Before attempting to isolate the FCNH signal, there are a number of requirements on the data so that the events under consideration are free of any known detector issues and accurately represent real multilepton events. An outline of the cut flow is shown below,

- (1) **triggers**: one of the triggers described in section 5.1.1 must have fired;
- (2) **primary vertex**: at least one primary vertex satisfying requirements in section 5.2.1;
- (3) **noise filters** (data only): includes scraping filter, HCAL noise filter, and CSC tight halo filter;
- (4) **lepton preselection**: require two same-sign leptons (as defined in section 5.2.2) with lead lepton $p_T > 20 \text{ GeV}$ and trailing lepton $p_T > 10 \text{ GeV}$ or three leptons

with lead lepton $p_T > 20 \text{ GeV}$ and both trailing leptons with $p_T > 10 \text{ GeV}$ (This is mainly driven by the thresholds of the triggers used.);

- (5) **low mass filter:** veto on events where dilepton pair that has a mass less than 30 GeV ;
- (6) **cosmic filter:** veto on events with two muons that are back-to-back (angle between them is within $[\pi - 0.05, \pi + 0.05]$).

Examples of distributions for the relevant variables after applying the preselection requirements from section 5.3.1 are shown in figures 5.13 and 5.14.

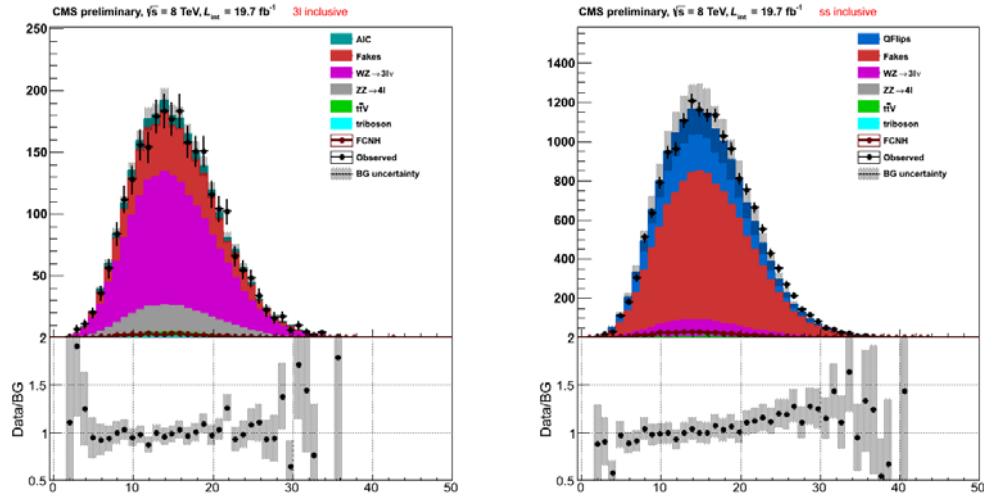


Figure 5.2. Effect of applying pileup reweighting on reconstructed primary vertices distribution for three lepton (top left), same-sign dileptons (top right), and inclusive (bottom) final states.

Combined Scale factors for IdIsoSip

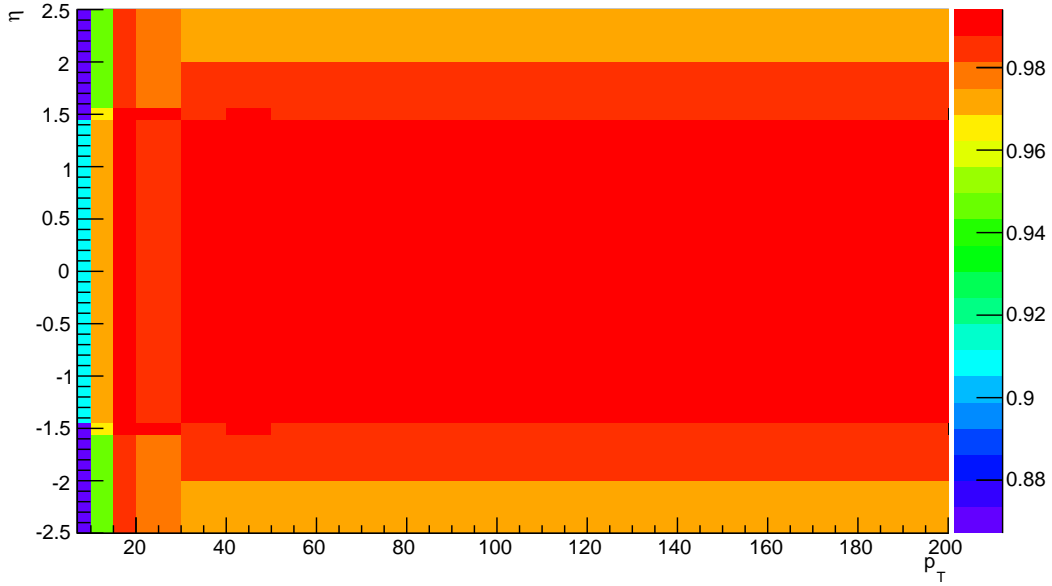


Figure 5.7. Scale factors for efficiency of electrons between data and simulation.

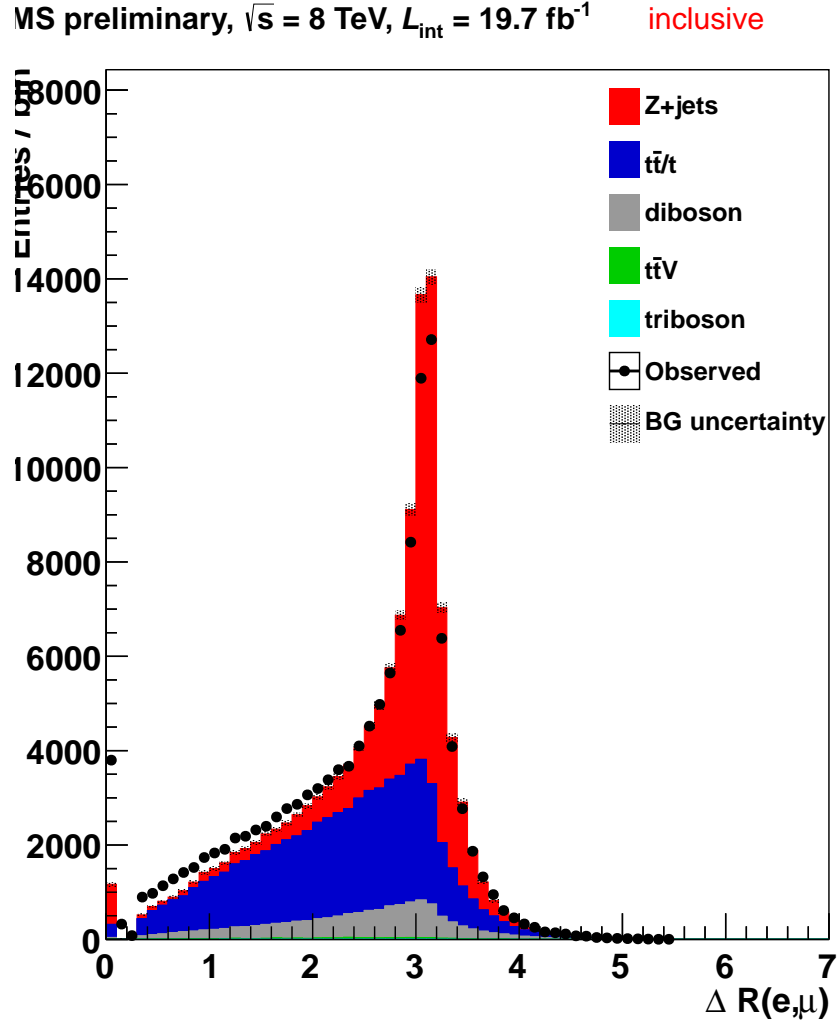


Figure 5.8. ΔR between all muons and electrons in all events passing dilepton triggers. Does not include efficiency corrections or QCD background estimate.

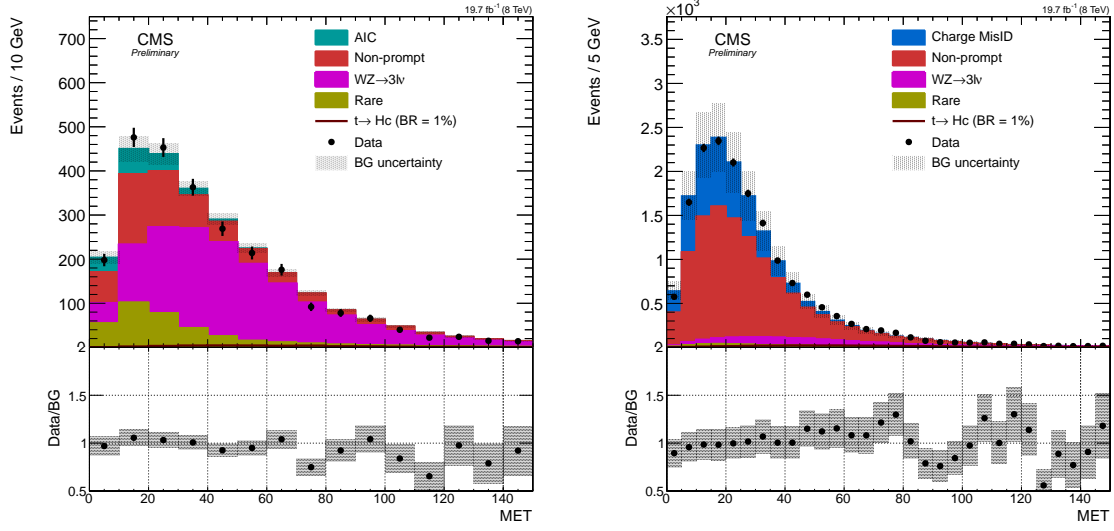


Figure 5.12. MET distributions for trilepton events (left), and same-sign dilepton events (right) at the preselection level.

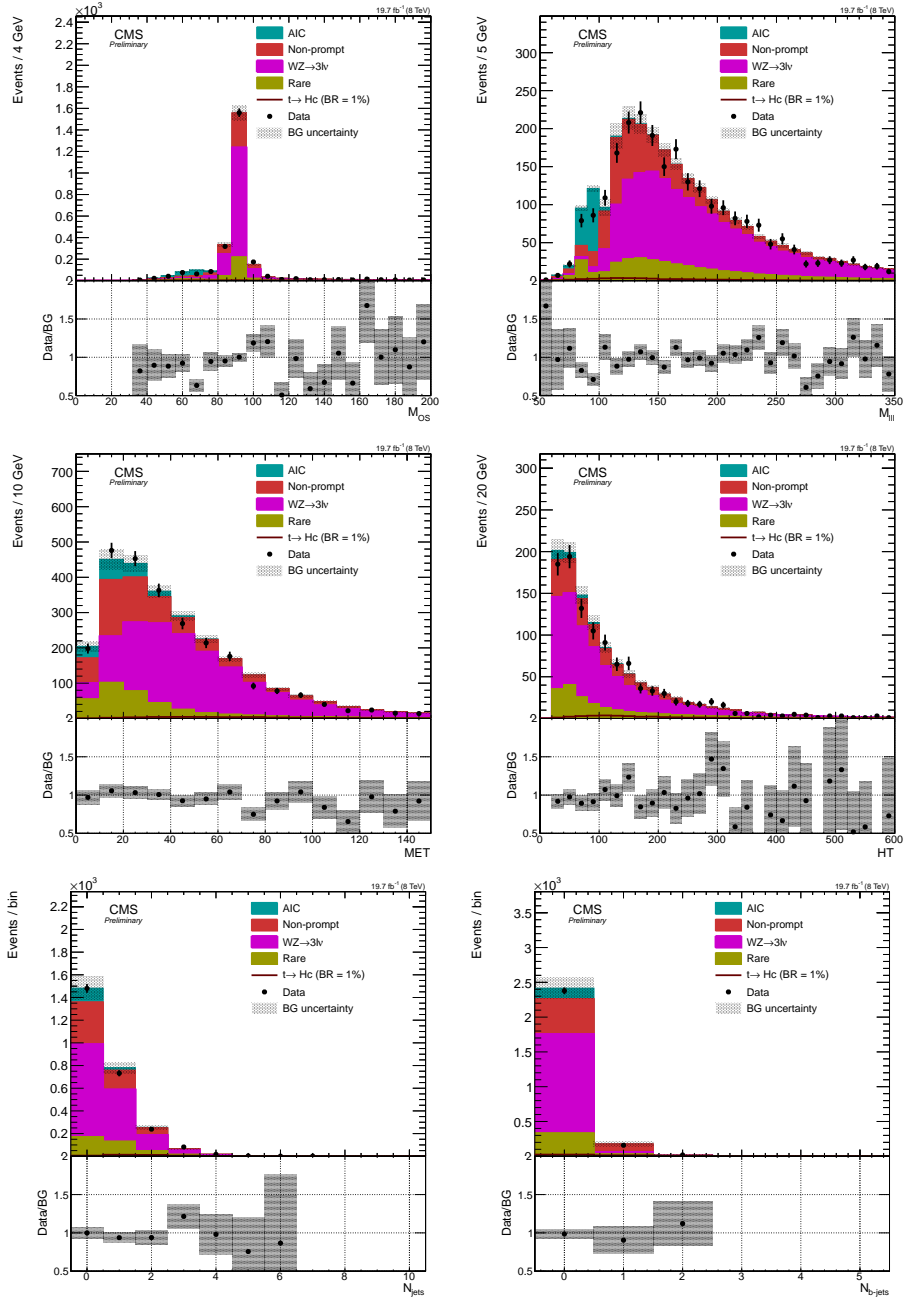


Figure 5.13. Examples of variables that are cut on in the analysis at the preselection level for three lepton events. From upper left to lower right they are OSSF dilepton mass, trilepton mass, MET, H_T , light jet multiplicity, and b-jet multiplicity.

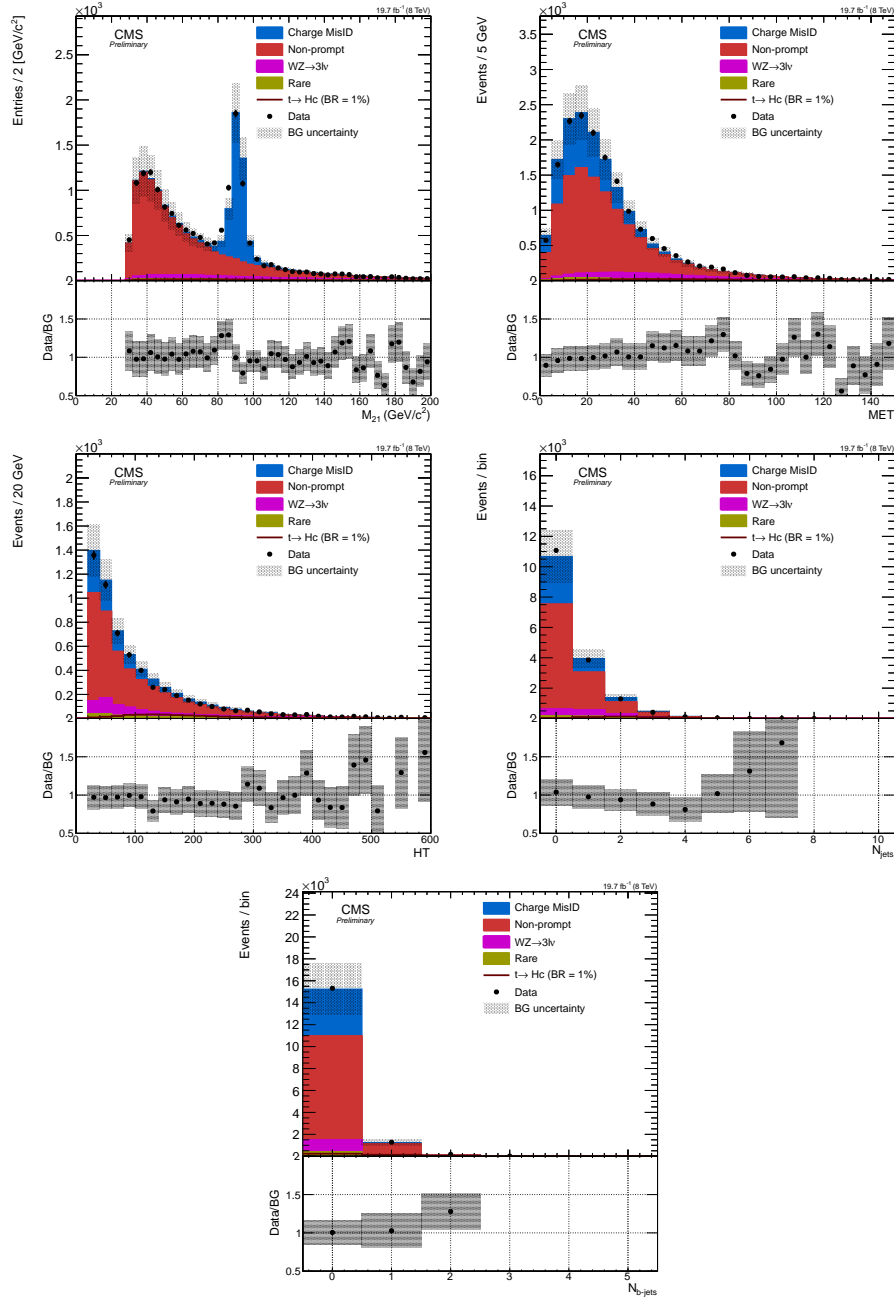


Figure 5.14. Examples of variables that are cut on in the analysis at the preselection level for same-sign dilepton events. From upper left to lower right they are dilepton mass, MET, H_T , light jet multiplicity, and b-jet multiplicity.

5.3.2. Cut-based Analysis

As an initial probe of sensitivity to these types of decays, a simple cut-based analysis is conducted to enhance the signal efficiency and decrease the amount of background contamination. The cuts are motivated by consideration of the FCNH decay topology are summarized here and described in more detail later in this section:

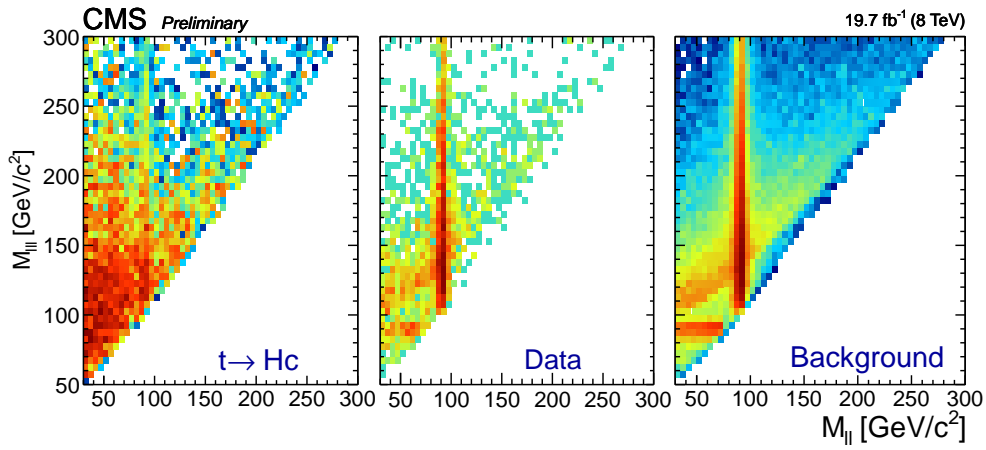


Figure 5.15. Trilepton mass vs dilepton same-flavor, opposite-sign mass at the preselection level.

- 3ℓ analysis:
 - same flavor dilepton Z veto ($|M_{ll} - M_Z| > 15 \text{ GeV}$);
 - trilepton Z veto (if $M_{ll} > 50 \text{ GeV}$ then $|M_{3l} - M_Z| > 10 \text{ GeV}$);
 - 2 or more jets;
- 2ℓ analysis.
 - same flavor dilepton Z veto ($|M_{ll} - M_Z| > 15 \text{ GeV}$);
 - 2 or more jets;
 - $MET > 40 \text{ GeV}$;

- MET dependent HT cuts (see table 5.4);
- at least two jets.

The first step is to remove events originating from decays of Z bosons. This is done by vetoing three lepton events where two leptons forming an opposite-sign, same-flavor (OSSF) pair are within 15 GeV of the nominal Z mass of 91.2 GeV. Rejected events can then be used to form a control region to verify the normalization of backgrounds that are a result of the decay of a Z boson. Additionally, events where there is final state radiation of a photon from one of the leptons decaying from a Z boson is taken into account by considering the trilepton mass. The radiated photon can either fake an electron or convert to a dilepton pair with one of the converted leptons falling outside the acceptance [58]. If there is an opposite-sign, same-flavor pair having mass greater than 50 GeV, the event is vetoed if the trilepton mass, $M_{3\ell}$ is within ± 10 GeV of the Z mass. The M_{ll} vs M_{lll} distribution for signal, background, and data events are shown in figure 5.15.

MET (GeV)	HT (GeV)
40-70	≥ 140
70-90	≥ 100
> 90	≥ 60

Table 5.4. MET dependent HT cuts for same-sign dilepton extraction.

To optimize signal discrimination, several variables are considered based on the signal topology. Distributions of data and background were compared and selection cuts were made decided based upon an optimal value of signal significance,

$$(5.6) \quad \text{significance} = \frac{N_{\text{signal}}}{\sqrt{N_{\text{signal}} + N_{\text{background}}}}.$$

It is found that requiring at least 2 jets (ignoring jet flavor) in the event strongly discriminates between signal and background. The multiplicity of inclusive jets and b-jets after the Z veto is shown in figures 5.17 and 5.18, respectively. The strength of this cut is such that further one dimensional cuts (MET, HT, and b-jet multiplicity were considered as candidates) do not improve the signal significance for the trilepton analysis. For the same-sign dilepton analysis, signal sensitivity can be achieved by applying cuts on both MET and HT.

The cut optimization in the MET versus HT plane is performed by considering the set of cuts that will optimize the expected limit. This is done by scanning through MET values in bins of 10 GeV and considering the HT cut that gives the best expected limit. This results in a series of cuts on HT that are parameterized by MET. A base-level cut of 40 GeV is applied to the MET. The distributions of background-like and signal-like events can be seen in figure 5.16.

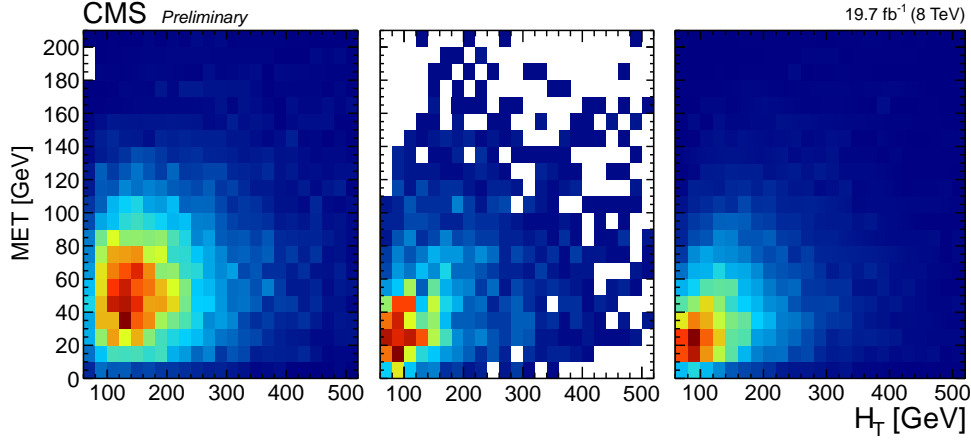


Figure 5.16. Distributions of events in the MET vs. H_T plane for same-sign dilepton events after requiring that there be at least 2 jets in the event.

From left to right: signal, data, and background.

Several variables that are useful for characterizing the signal region are shown in figures 5.21 and 5.22 after the analysis selection has been applied.

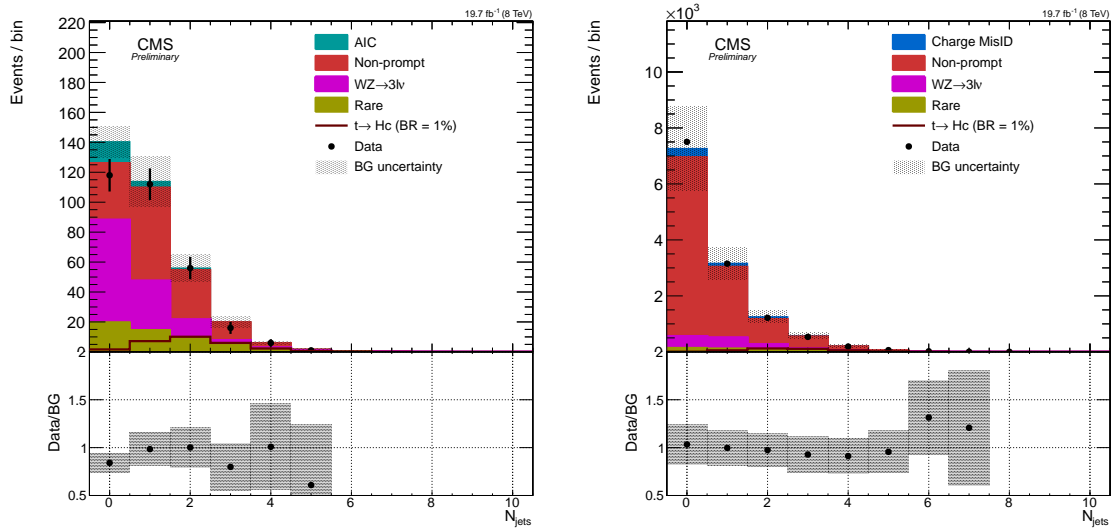


Figure 5.17. Multiplicity of all jets after the Z veto requirement for three lepton (left) and same-sign (right) selections.

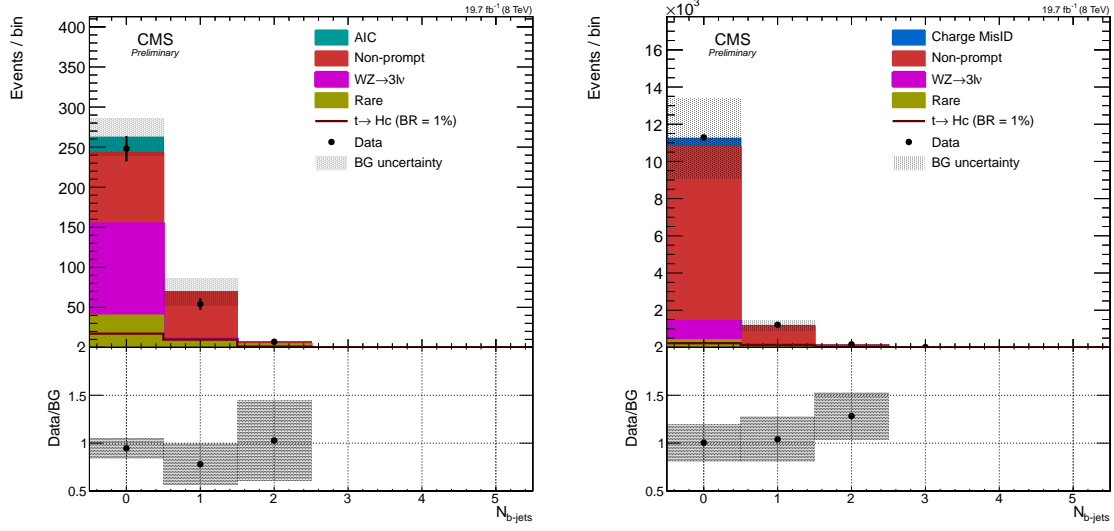


Figure 5.18. Multiplicity of b-jets after the MET and H_T requirements for three lepton (left) and same-sign (right) selections.

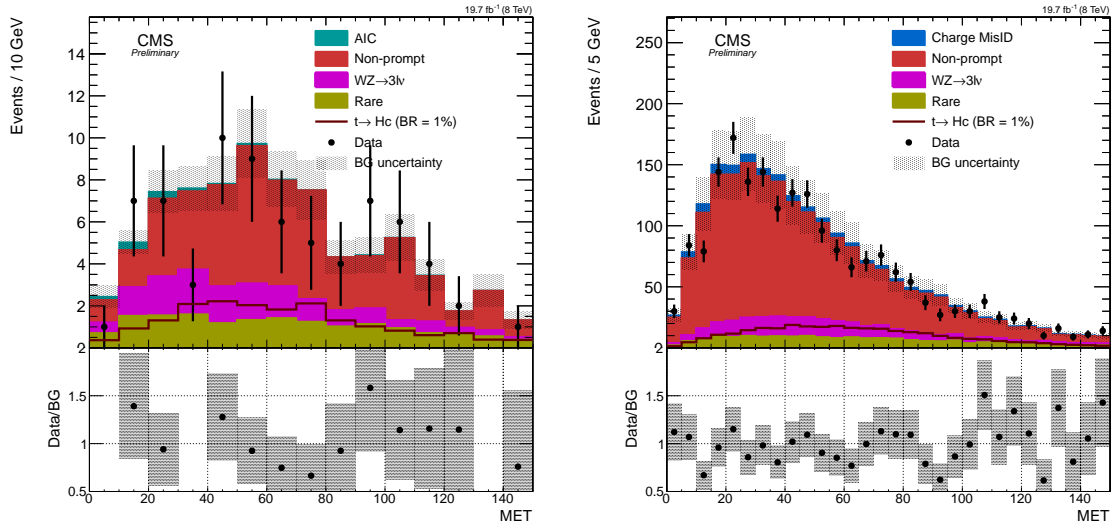


Figure 5.19. MET distributions for three lepton (left) and same-sign selections after ≥ 2 jet requirement.

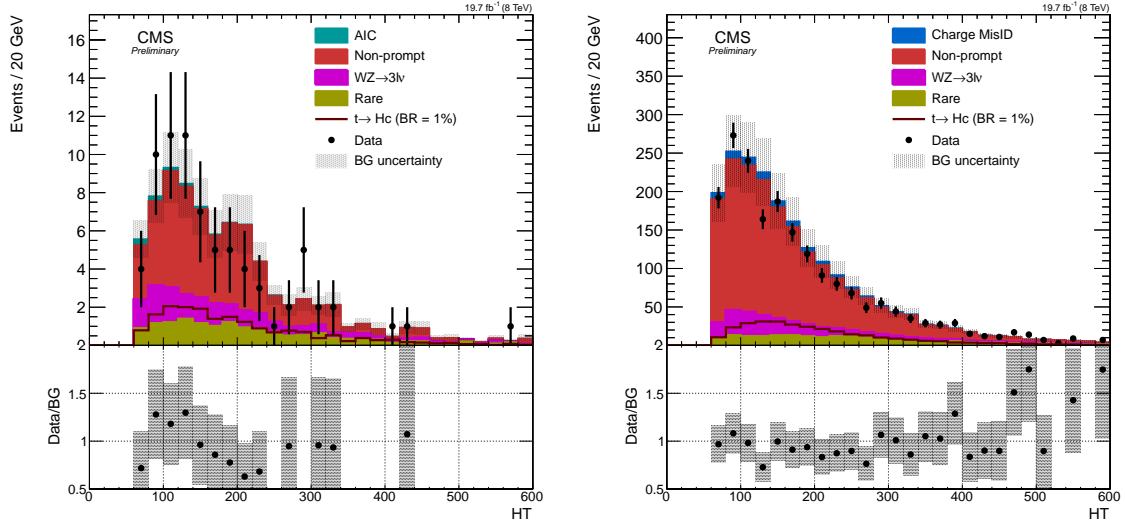


Figure 5.20. H_T distributions for three lepton (left) and same-sign selections after ≥ 2 jet requirement.

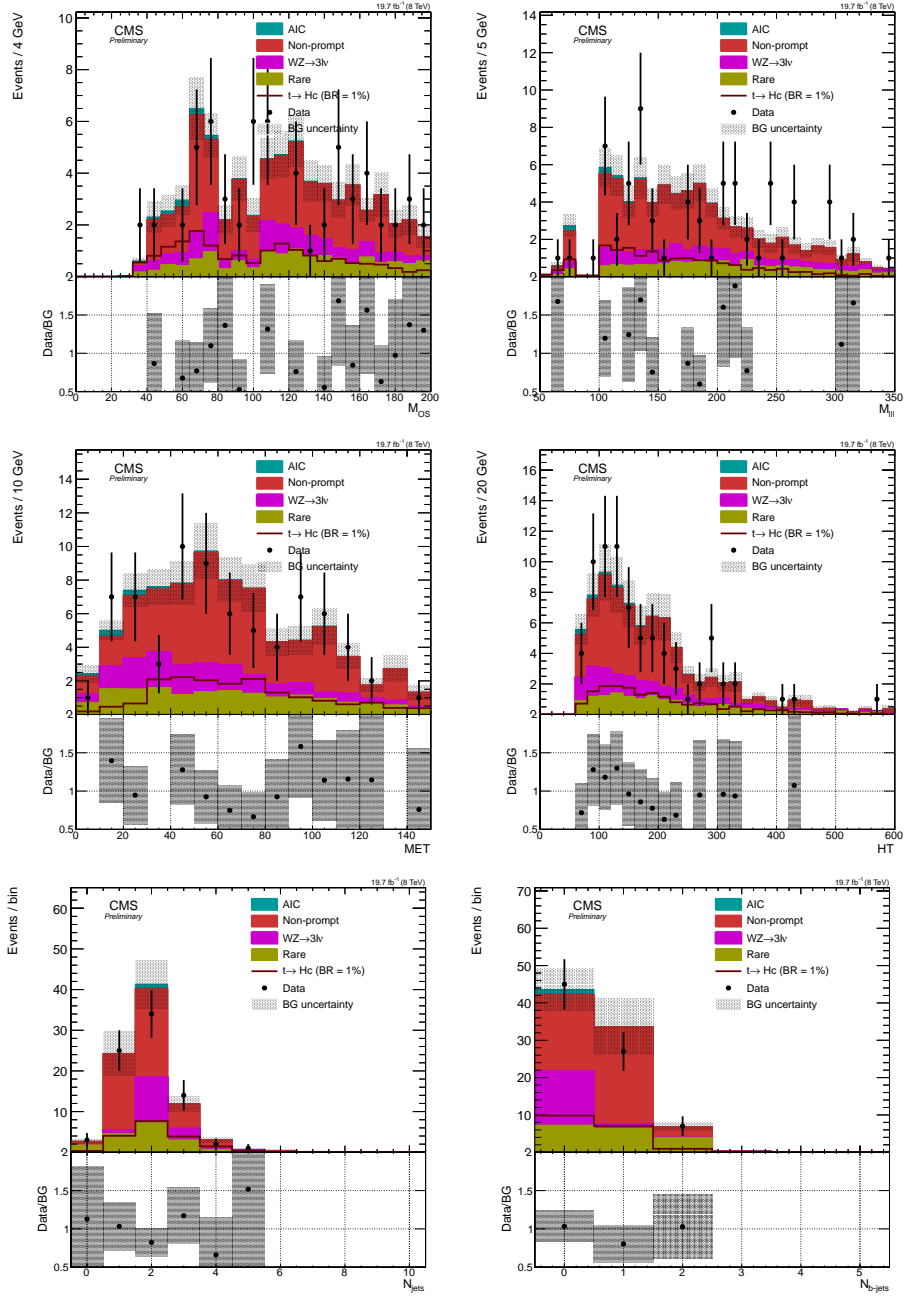


Figure 5.21. Examples of variables that are cut on in the analysis at the final selection level for three lepton events. From upper left to lower right they are opposite-sign, same flavor dilepton mass, trilepton mass, MET, H_T , light jet multiplicity, and b-jet multiplicity.

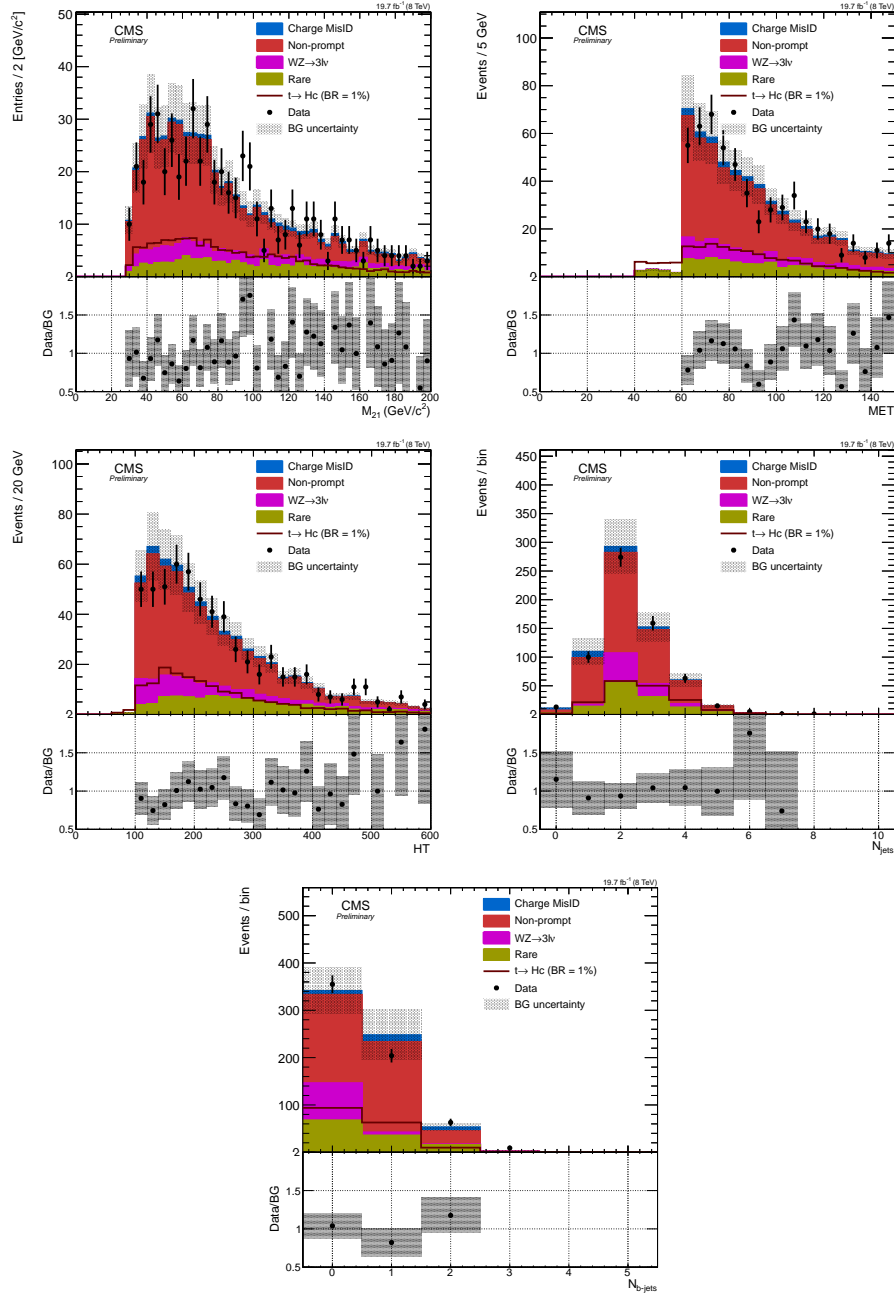


Figure 5.22. Examples of variables that are cut on in the analysis at the final selection level for same-sign dilepton events. From upper left to lower right they are dilepton mass, MET, H_T , light jet multiplicity, and b-jet multiplicity.

process	trilepton	Z removal	≥ 2 jets
Rare	380.4 ± 11.9	54.3 ± 2.1	19.6 ± 1.4
$WZ \rightarrow 3l\nu$	1451.9 ± 93.4	117.0 ± 7.6	15.8 ± 1.1
Non-prompt	613.4 ± 97.3	148.8 ± 25.7	49.4 ± 9.0
BG	2598.3 ± 135.5	339.4 ± 27.0	86.2 ± 9.3
Observed	2555	309	79
$FCNH \rightarrow WW$	27.9 ± 1.9	21.0 ± 1.5	14.4 ± 1.1
$FCNH \rightarrow \tau\tau$	9.1 ± 0.6	6.4 ± 0.4	4.4 ± 0.3
$FCNH \rightarrow ZZ$	2.9 ± 0.2	0.5 ± 0.0	0.4 ± 0.0

process	same-sign dilepton	Z removal	≥ 2 jets	E_T^{miss} -dependent H_T
Rare	512.3 ± 12.9	495.6 ± 12.5	225.5 ± 9.7	128.1 ± 6.4
$WZ \rightarrow 3l\nu$	1080.1 ± 68.4	1041.9 ± 66.0	242.2 ± 15.4	83.9 ± 5.4
Charge MisID	4407.3 ± 881.7	521.1 ± 104.3	101.6 ± 20.3	32.1 ± 6.4
Non-prompt	10644.2 ± 1574.7	10493.7 ± 1568.4	1561.4 ± 248.9	409.8 ± 72.3
BG	16643.9 ± 1806.3	12552.3 ± 1573.5	2130.7 ± 250.6	654.3 ± 73.1
Observed	16790	12686	2032	631
$FCNH \rightarrow WW$	307.8 ± 19.2	295.4 ± 18.4	246.2 ± 15.4	112.2 ± 7.1
$FCNH \rightarrow \tau\tau$	82.0 ± 5.1	79.4 ± 4.9	65.0 ± 4.0	30.8 ± 1.9
$FCNH \rightarrow ZZ$	3.4 ± 0.2	3.2 ± 0.2	2.9 ± 0.2	1.1 ± 0.1

Table 5.5. Event yields for trilepton (top) and same-sign (bottom) categories assuming $\mathcal{B}(t \rightarrow Hc) = 1\%$.

Examples of the analysis distributions and event yields divided into the various flavor categories and after each analysis cut is applied is shown in appendix A.1. The inclusive yields are shown in table 5.5.

An MVA analysis was also considered, but the results were not used in the limit calculation. Some of the preliminary results are shown in appendix A.2.

5.4. Background estimation

The main sources of background can be divided into two broad categories: irreducible backgrounds that have at least two prompt leptons in the final state as well as at least two jets and a non-negligible amount of MET, and reducible backgrounds where one or more of the leptons in the event is misidentified.

Given that at least two prompt leptons and two jets are required in the final state, the main sources of irreducible backgrounds are $t\bar{t}$ associated with vector boson production, WZ, and, to a lesser extent, triboson production. The contribution from these processes are estimated based on simulated samples. Cross-sections for the $t\bar{t} + V$ samples are taken from calculations performed in [59].

For trilepton final states, the contribution from asymmetric internal conversions is also considered though the contribution after the full analysis selection is found to be negligible. This process arises primarily from final state radiation of a virtual photon from a lepton produced via Drell-Yan production. The virtual photon then decays with the majority of its energy going into one of the final state leptons so that the other lepton is undetected due to acceptance requirements. A data-driven estimation is performed following the approach adopted in previous searches for super-symmetric particle production in multilepton final states [60]. The contribution after all selection requirements is on the order of 1-2%, about the same as the contribution from triboson decays. A summary of the method is presented below.

In order to cross-check the validity of the theoretical cross-sections, dedicated control regions are selected for $t\bar{t}$ and WZ events. In these regions the MC prediction is compared to the data and scaled appropriately. These studies are described below.

There are two major sources of reducible backgrounds for the final states of interest: misidentification of prompt lepton production and mismeasurement of electron charge. The former arises due to non-prompt leptons produced during the hadronization process of outgoing quarks (e.g: semileptonic decays of B mesons), or hadrons passing the identification and isolation requirements of the prompt leptons. These events will be referred

to as arising from lepton “fakes”. The other source of background originates from the charge misidentification of electrons (the effect is negligible for muons) in the much more frequent production of opposite sign dilepton pairs (mostly from production of Z bosons). This background only contaminates the same sign dilepton final state. The data-driven methods to estimate non-prompt lepton and charge misidentification backgrounds are described below.

5.4.1. MC Control Regions

To verify the predictions for simulated WZ and $t\bar{t}$ backgrounds, dedicated control regions are selected from the same data streams used for the signal region. The control regions are selected to maximize the contribution of the processes under investigation and to be orthogonal to the signal region.

Sample	N_{event}
WZ $\rightarrow 3\ell\nu$ (MC)	83.9 ± 4.4
Non-WZ	20.1 ± 1.9
WZ $\rightarrow 3\ell\nu$ (Data)	117 ± 10.8
$\frac{ N_{Data,WZ} - N_{MC,non-WZ} }{N_{MC,WZ}}$	1.15 ± 0.14

Table 5.6. Yields for WZ control region. Quoted uncertainties are statistical only.

5.4.1.1. WZ. The WZ control region is selected requiring 3 leptons with two of the leptons forming a same-flavor, opposite-sign pair with an invariant mass within $15 \text{ GeV}/c^2$ of the nominal Z mass, $91.2 \text{ GeV}/c^2$. Events with at least one jet passing the medium CSV working point are vetoed to reduce contamination from $t\bar{t}$ events. Due to the presence of a neutrino from the W decay, a requirement that the $E_T^{\text{miss}} > 50 \text{ GeV}$ is applied. Relevant distributions in the WZ control region are shown in figure 5.23. To make the sample

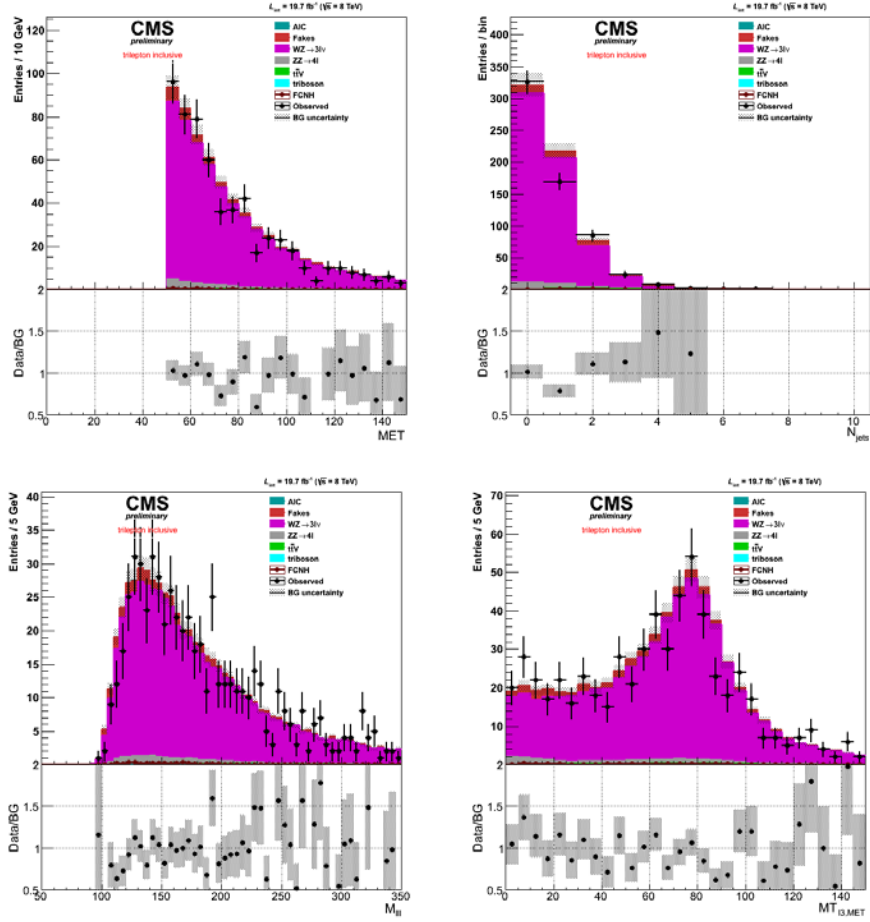


Figure 5.23. From upper left: MET, jet multiplicity, $M_{\ell\ell}$, and $MT_{\ell 3, MET}$ distributions in WZ control region. Observed data distributions (points) are plotted against simulation.

more similar to what is expected in the control region an additional requirement that there be at least two jets in the event is applied. The yields observed in data compared to the estimation from simulation is shown in table 5.6. There is some discrepancy at this level, but it is consistent within the assigned uncertainty. In response to this, there is no scaling factors applied to the WZ sample, but instead the discrepancy is used to apply an overall systematic uncertainty of 15% on the WZ normalization.

5.4.1.2. $t\bar{t}$. The $t\bar{t}$ control region is selected by requiring 2 leptons, with opposite charge and flavor, and one jet passing the medium CSV working point, or two jets passing the loose CSV working point. Predicted and observed rates are shown in table 5.7 and some relevant distributions are shown in figure 5.24. The contribution of $t\bar{t}$ in such a sample is 90%. There is currently no correction applied to account the discrepancy between the MC and observation. The MC $t\bar{t}$ prediction is not used directly in the analysis, but is used when assessing the accuracy of the non-prompt lepton background estimation. It also gives us a handle on the signal normalization since the underlying production mechanism is the same.

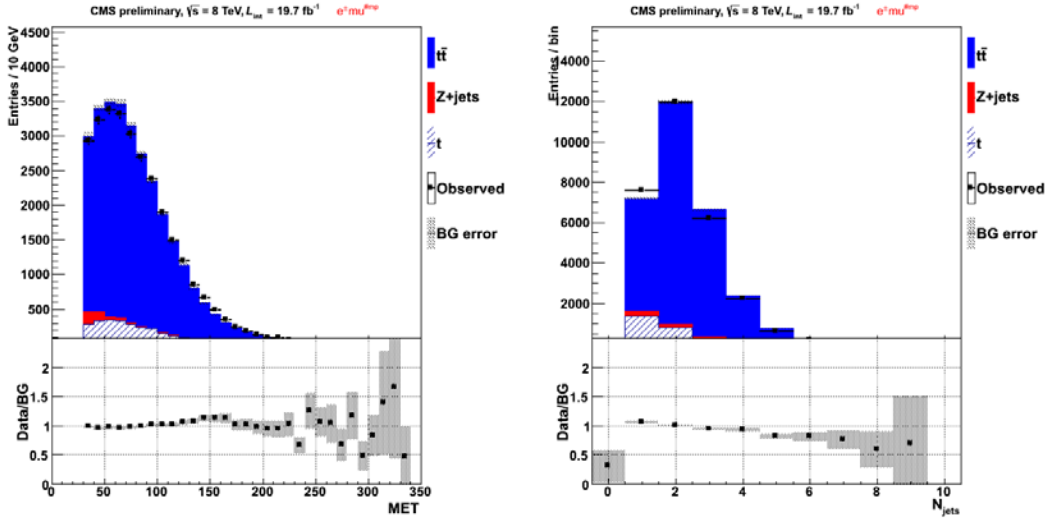


Figure 5.24. MET and jet multiplicity distributions for the $t\bar{t}$ control region. Observed data distributions (points) are plotted against predicted Standard Model contributions.

	t	Z+jets	$t\bar{t}$	BG	Observed
preselection	6036.5 ± 60.9	59884.8 ± 396.5	57370.4 ± 213.2	123291.7 ± 454.3	129437
$t\bar{t}$ control region	2617.1 ± 40.1	502.8 ± 36.7	26055.5 ± 143.7	29175.4 ± 153.6	28813

Table 5.7. Yields in $t\bar{t}$ control region. Quoted uncertainties are statistical only.

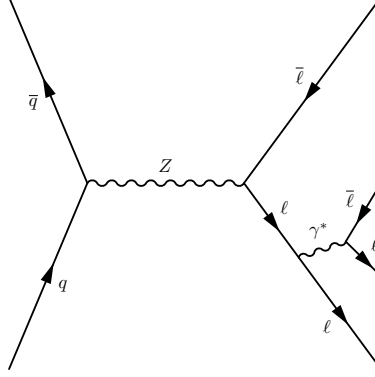


Figure 5.25. Example of internal asymmetric conversion originating from Drell-Yan production.

5.4.2. Asymmetric Internal Conversions

Final state leptons have some probability to radiate photons which can either propagate into the detector and convert to $e^\pm e^\mp$ pairs or convert internally and have near equal probability to convert to electron or muon pairs. The latter process is shown in figure 5.25. The contribution is estimated by reweighting $Z \rightarrow \ell^\pm \ell^\mp + \gamma$ events to $Z \rightarrow \ell^\pm \ell^\mp + \ell^\pm (\ell^\mp)$. This is done by requiring the opposite-sign, same-flavor pair have a dilepton mass below the on-shell Z mass ($M_{\ell\ell} < 75 \text{ GeV}$) and that then making the p_T -dependent ratio,

$$(5.7) \quad w_{AIC}(p_T) = \frac{N_{\ell\ell\ell}(p_T)}{N_{\ell\ell\gamma}(p_T)}.$$

Additionally it is required that the relevant three-body mass be within 15 GeV of the on-shell Z mass. The above ratio is done to take into account the final state lepton flavor composition.

5.4.3. Fake Lepton Background

For the signal regions of interest, events originating from QCD, W/Z+jets and $t\bar{t}$ can contaminate the selected sample when a lepton originating from a non-prompt decay is misidentified as a prompt lepton. The estimation of this type of background is not accurately modeled in simulation or the available samples are statistically limited such that a data-driven method, the “fake rate” method is adopted to estimate the amount of contamination from such backgrounds. This method is used widely in CMS analyses concerned with similar topologies. The approach here is used in many CMS analyses, but follows most closely the procedure used in the CMS search for Higgs boson produced in association with $t\bar{t}$ [61].

The method is carried out in two main steps. First, the probability for a non-prompt lepton-like object to fake a prompt lepton is measured in a dedicated control region (“measurement region”). Once this probability or fake rate is measured, it is applied to a second control region (“application region”) which is enriched in processes that lead to fake contamination in the signal region. The control regions are selected in such a way that kinematics are as close as possible to the signal regions.

Two regions are considered for the determination of the fake rate in order to probe different flavor and kinematic compositions anticipated in the signal region. One control region is enriched in production of bottom quark pairs and the other is enriched in Z+jet production. Both are constrained by triggers which are the same double lepton triggers (see table ??) used for extraction of the signal.

5.4.3.1. QCD $b\bar{b}$ Fake Rate Measurement Region. The QCD $b\bar{b}$ region is prepared by first requiring a tag muon which is roughly consistent with a b quark decay. This is enforced by requiring the following of the tag muon:

- **anti-isolated:** $Is_{rel} > 0.2$,
- **displaced vertex:** $d_{xy} > 0.2 \text{ cm}, d_z > 0.2 \text{ cm}$,
- **loose b-tag:** match muon to a b-tag passing loose CSV working point by requiring $\Delta R_{b-jet,\mu} < 0.3$.

Next, a probe lepton is defined from which the fake rate is determined. For the case of muons it is only required that it be reconstructed as a PF muon. For the electrons, the probe cuts are loosened to the level of the trigger requirement. This is done by requiring:

- $\sigma_{i\eta i\eta} < 0.014(0.035)$,
- $H/E < 0.15(0.1)$,
- $N_{losthits} = 0$,
- $Is_{track}/p_T < 0.2$,
- $Is_{ECAL}/p_T < 0.2$,
- $Is_{HCAL}/p_T < 0.2$,

where the values in parantheses are for electrons in the endcaps. Finally, a set of requirements are placed on the kinematics of the tag/probe pair to further ensure that event is consistent with $b\bar{b}$ production. These are:

- the tag and probe leptons are required to be back-to-back ($\Delta\phi(tag, probe) > 2.$);
- and balanced in transverse momentum in favour of the tag:

$$(5.8) \quad \frac{p_T^{probe}}{p_T^{tag} \cdot (1 + Is_{rel}^{tag})} < 1,$$

- events are vetoed if more than one lepton passing the tight identification requirements are found,

where the distributions for $\Delta\phi(tag, probe)$ and the tag-probe p_T balance are shown in figure 5.26. The kinematic distributions of the resulting tag muons are shown in figure 5.30.

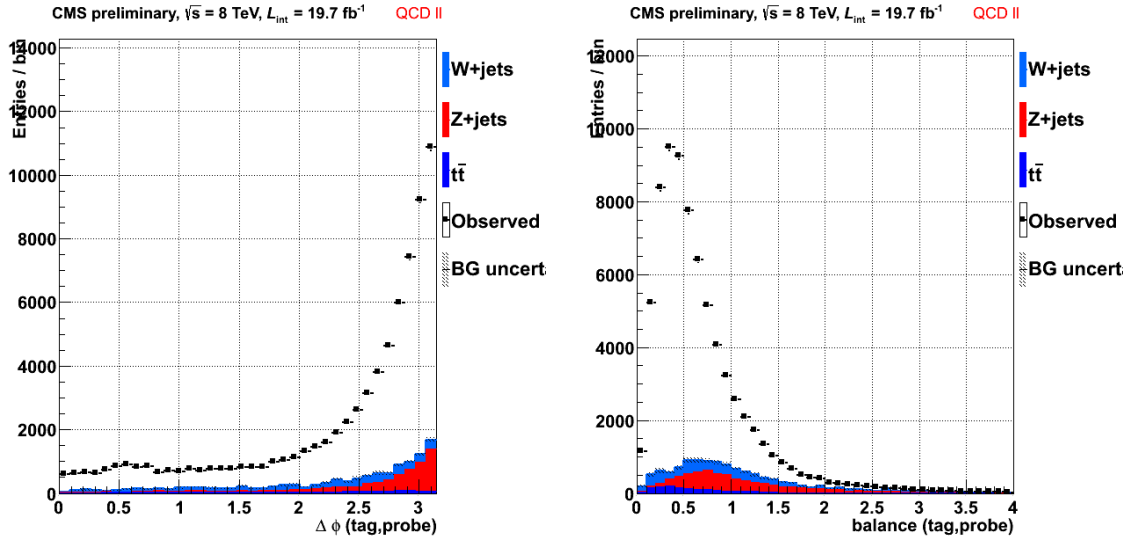


Figure 5.26. Variables used to increase purity of QCD $b\bar{b}$ region:

$\Delta\phi(tag, probe)$ is shown on the left; the balance is on the right.

At this point, the measurement of the fake rate can be carried out. This is done by finding the probability for the probe lepton to pass the tight identification requirements described in section 5.2.2, and parametrizing this quantity in bins of p_T and η (shown in figure 5.31 for both muons and electrons). That is,

$$(5.9) \quad f(p_T, \eta) = \frac{N_{pass}(p_T, \eta)}{N_{pass}(p_T, \eta) + N_{fail}(p_T, \eta)}.$$

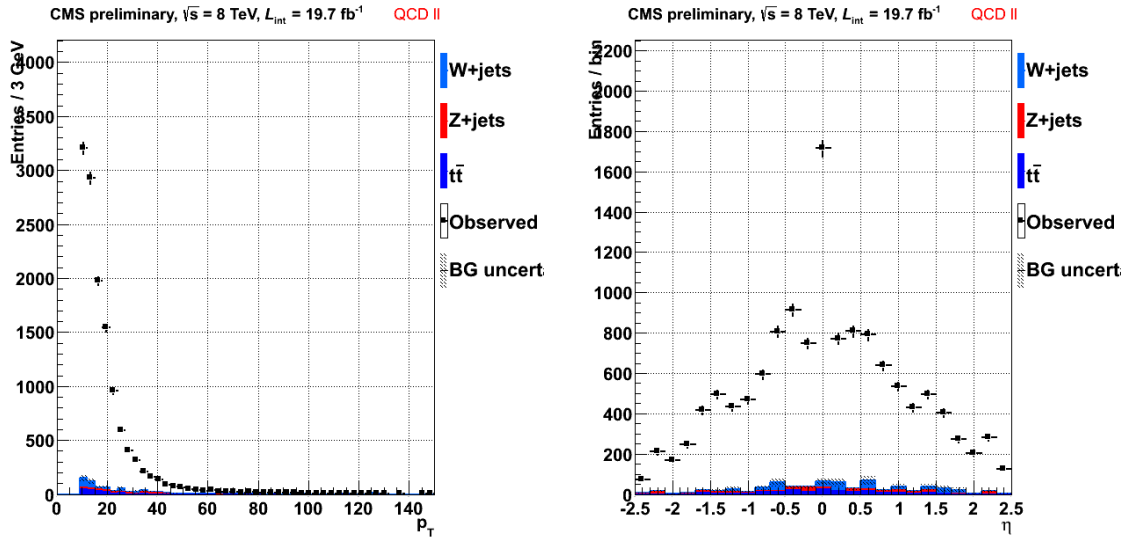


Figure 5.27. Kinematic distributions for the tag muon in the QCD $b\bar{b}$ region.

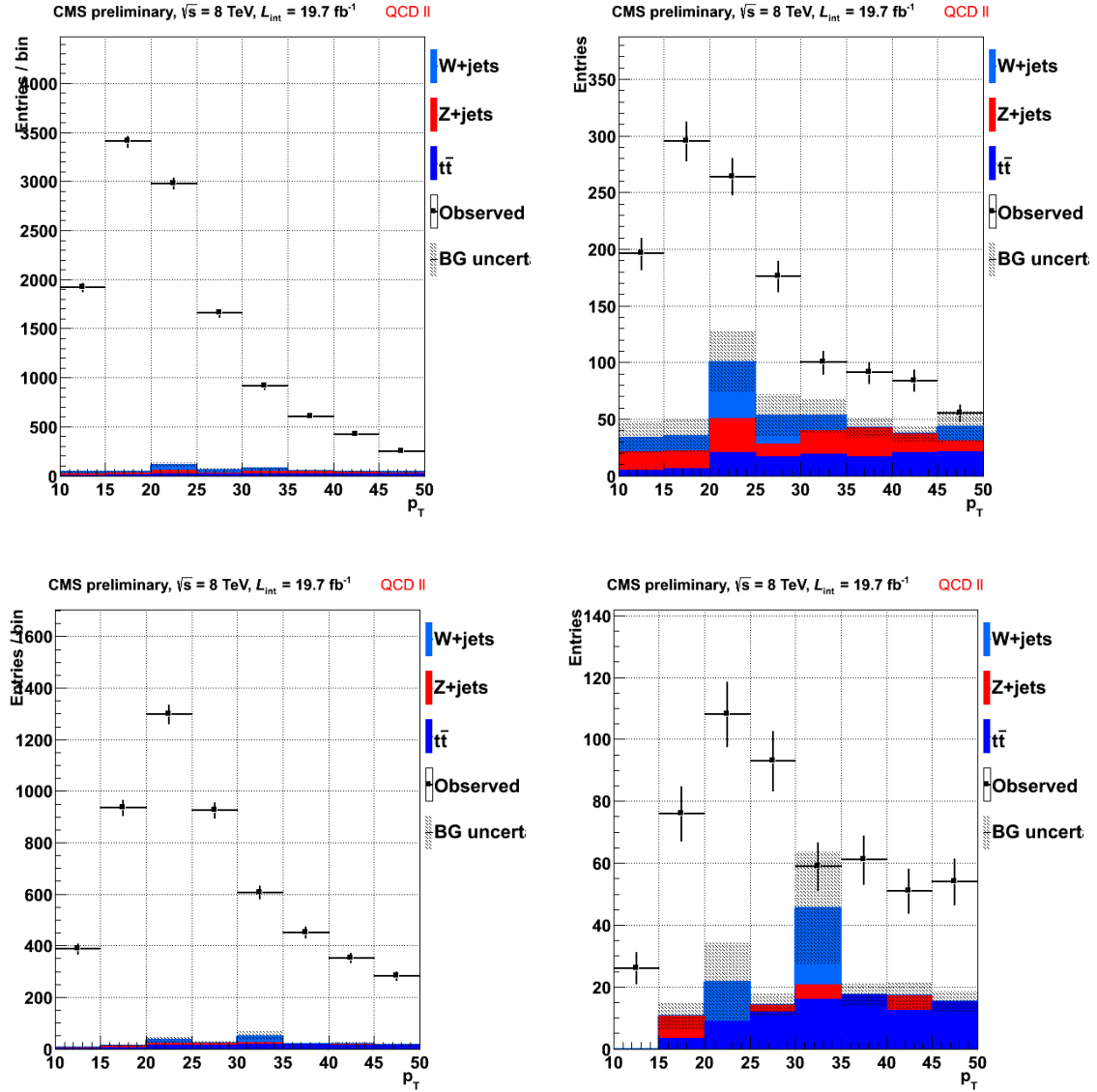


Figure 5.28. p_T distributions for the probe muon (top left), passing muons (top right), probe electron (bottom left) and passing electrons (bottom right) in the QCD $b\bar{b}$ region.

Though, the control region is carefully selected to enhance the purity of non-prompt lepton decays, there is a non-negligible contamination from processes resulting in a decay to a prompt lepton ($Wb\bar{b}$, $Z + \text{jets}$, $t\bar{t}$, etc.). This is taken into account by carrying out the fake rate measurement on simulated samples containing the expected type of contamination and subtracting off the resulting contribution. This leads to the following definition of a contamination subtracted fake rate,

$$(5.10) \quad f(p_T, \eta) = \frac{N_{pass}^{data}(p_T, \eta) - N_{pass}^{MC}(p_T, \eta)}{N_{probe}^{data}(p_T, \eta) - N_{probe}^{MC}(p_T, \eta)}.$$

where $N_{probe} = N_{pass} + N_{fail}$. The measured fake rates from this region for both electrons and muons are shown in figure 5.29.

In the case that a fakeable object is reconstructed as both a muon and an electron, the probability of it to pass both tight selections are considered.

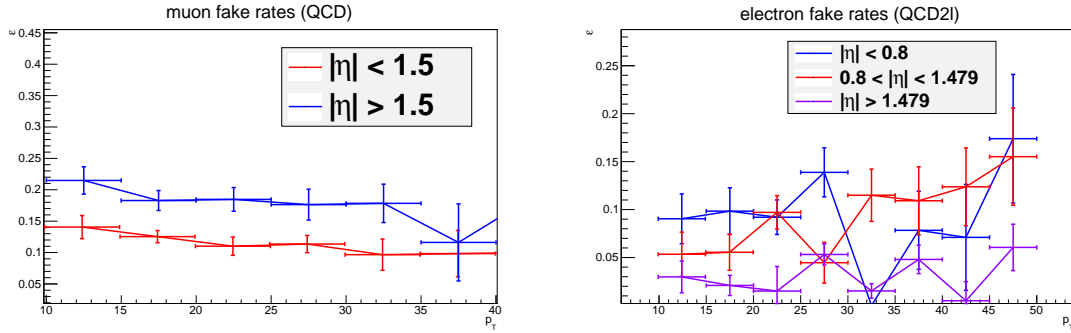


Figure 5.29. Fake rates measured QCD $b\bar{b}$ region for muons (left), and electrons (right).

5.4.3.2. Z+jet Control Region. The Z+jet control region is defined by requiring two same flavor, opposite sign leptons passing the standard analysis lepton identification and

isolation requirements described in section 5.2.2. The dilepton pair fulfills the function of the tag, and is required to have a mass within a 30 GeV window centered at the Z mass. The probe definitions are the same as in the QCD $b\bar{b}$ region with an additional requirement that the MET be below 50 GeV to reduced contamination from WZ events.

This region is mainly useful in measuring the fake rates of lower p_T (less than 30 GeV) electrons.

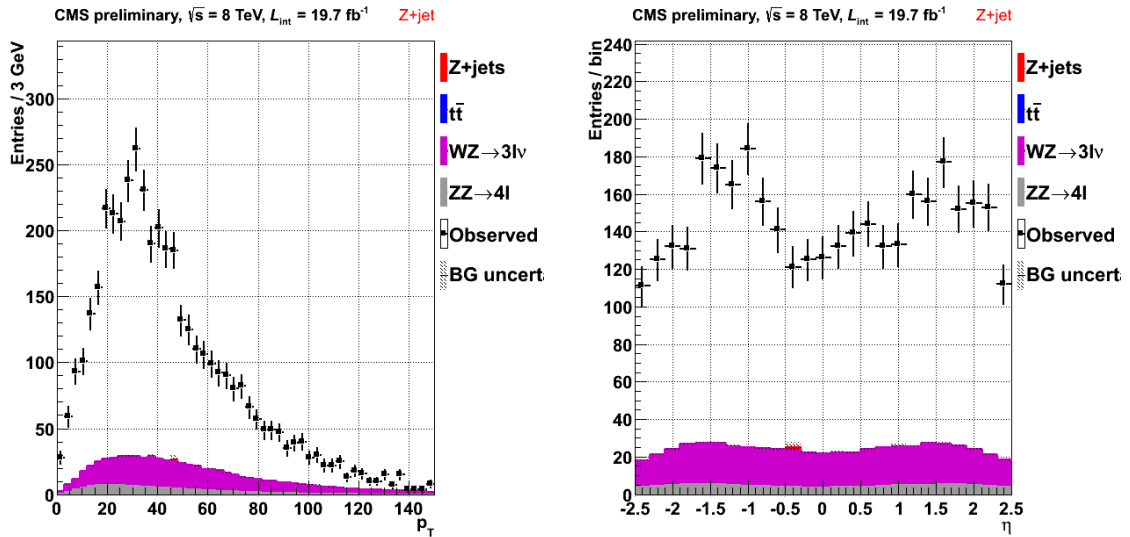


Figure 5.30. Kinematic distributions for the tag muon in the Z+jet region.

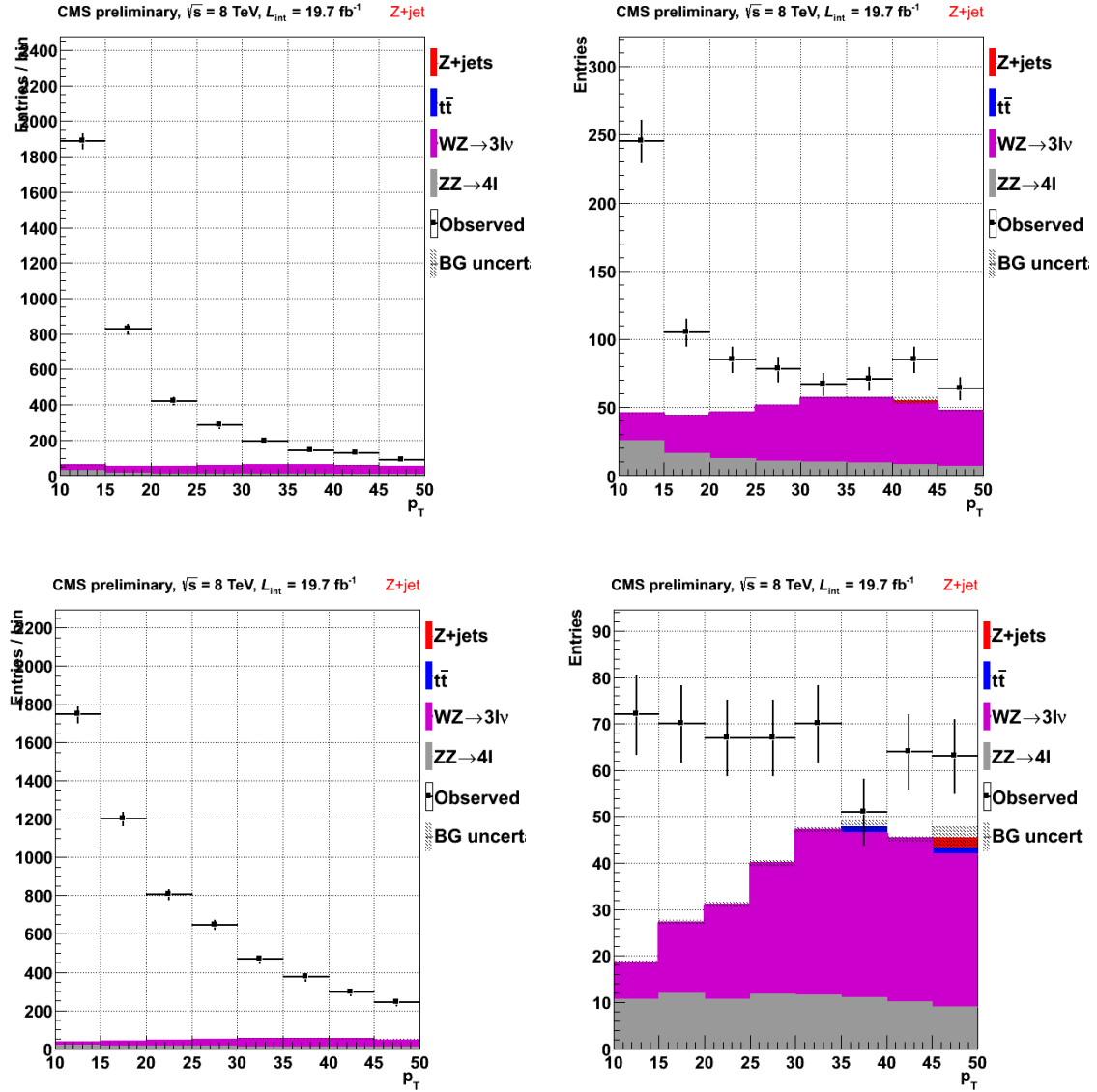


Figure 5.31. p_T distributions for the probe muon (top left), passing muons (top right), probe electron (bottom left) and passing electrons (bottom right) in the Z+jet region.

5.4.3.3. Fake Rate Application. Once the fake rate is determined, it is applied to a control region where there is one or two objects that pass the probe lepton selection but fail the tight lepton identification criteria referred to as a fakeable object. This is done by applying a weight to each event that is based on the failing lepton's kinematics,

$$(5.11) \quad w(p_T, \eta) = \frac{N_{pass}(p_T, \eta)}{N_{fail}(p_T, \eta)}$$

$$(5.12) \quad = \frac{f(p_T, \eta)}{1 - f(p_T, \eta)}.$$

Where the fake rate, f , is defined in equation 5.9. In the case of events with two fakeable objects, the event weight is a multiplicative combination of the the weights from each fakeable individually.

The control region is mostly free from prompt lepton contamination so a monte-carlo subtraction of prompt contamination (as in the measurement region) is not pursued. The composition of fakes in the control region does have a dependance on the type of cuts that are applied. In particular, a tighter cut on the number of reconstructed jets makes it so the application region goes from being dominated by a mixture of QCD and W+jets to being mainly hadronic $t\bar{t}$ and W+jet. Figure 5.32 gives shows how the composition depends on jet multiplicity.

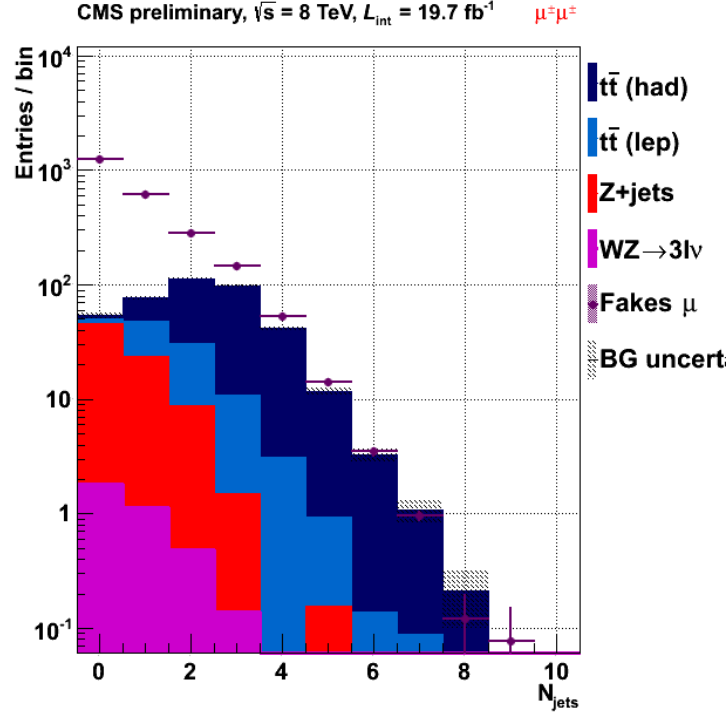


Figure 5.32. Composition of sample used for estimation of fake background.

The QCD estimation is not shown, but is presumed to account for the missing background.

5.4.3.4. Fake Rate Systematics. In order to assess the systematic uncertainty on the measurement of the fake rate, the fake rate is measured in several MC samples which are characteristic of both the measurement and the application regions. There are two main sources of uncertainty that are considered: the difference in composition between the measurement control regions, and the variation in composition between the measurement region and the application region.

The processes that need to be considered as contributing to both the fake rate measurement and the application of the fake rates are QCD, $t\bar{t}$, and V +jet where V can be either a W or Z boson. For several of these processes, it is not possible to prepare a data region with adequate statistics to estimate the fake rates so we rely on the estimation from MC. When measuring the fake rate in MC the same probe definitions are used, but the requirement of the tag is removed. Generator information is used to guarantee that probe lepton does not result from the decay of a vector boson, i.e., the probe is guaranteed to be fake. Figure 5.33 shows the fake rates measured for the relevant processes.

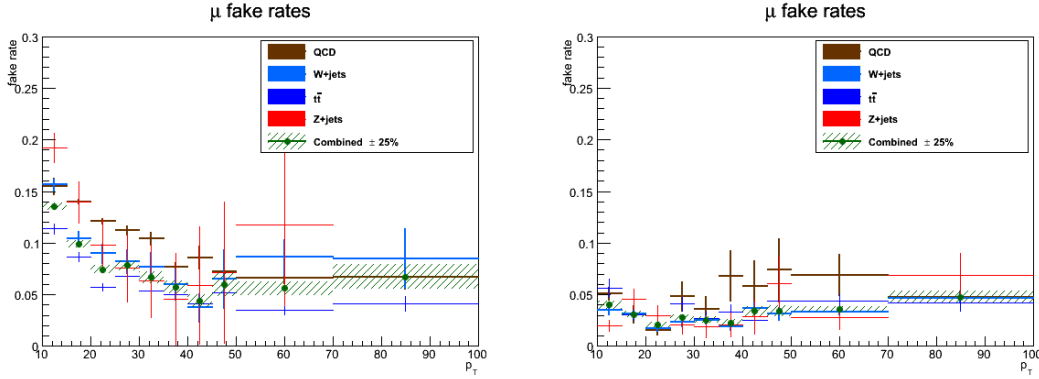


Figure 5.33. Fake rates measured in MC for various processes. Muon rates are shown on the left; electrons are on the right.

Once the fake rates are measured from the various background processes, they are combined according to their proportionate contribution in the signal region and the fake rate measurement region. A comparison of the fake rates in the two regions is shown in figure 5.34, and a breakdown of the relative contribution from each process is shown in table 5.8.

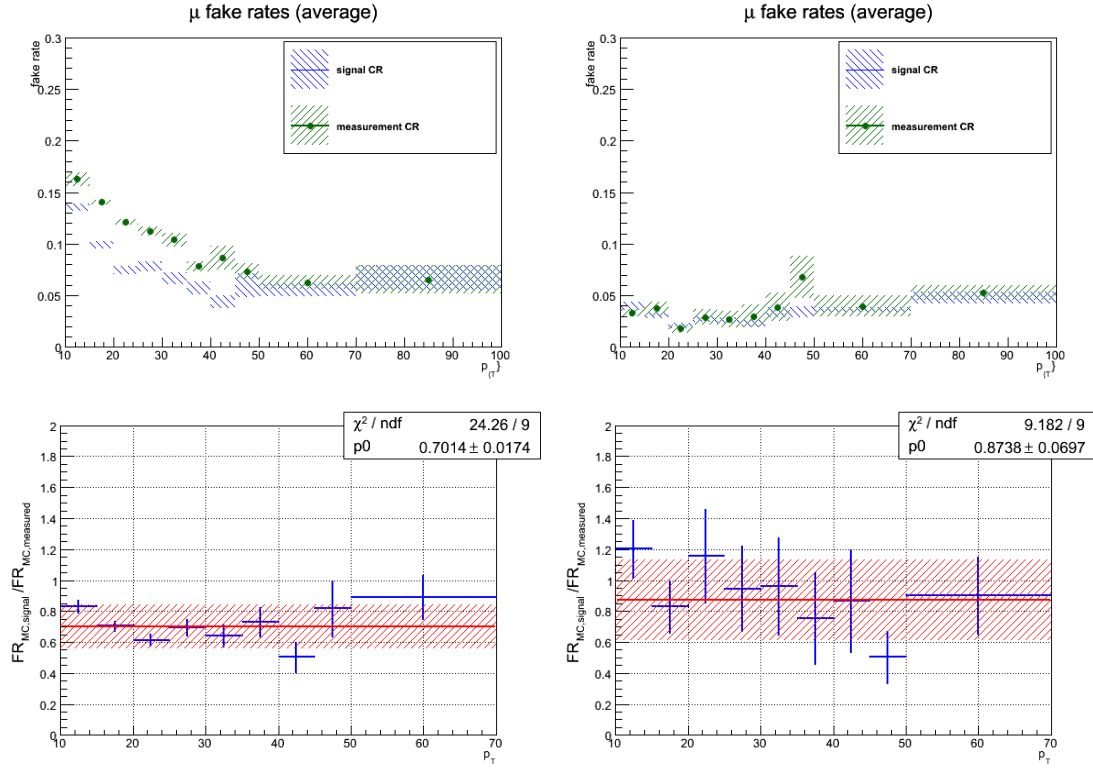


Figure 5.34. Comparison of fake rates measured in MC for measurement region and signal region compositions. Ratios between the two regions are shown in the bottom row with muons shown on the left, and electrons are shown on the right.

	W+Jets	Z+Jets	ttbar	QCD	Fakes
muons	63.1%	0.7%	36.2%	0.0%	236.61
electrons	62.7%	14.8%	22.5%	0.0%	40.56

Table 5.8. Comparison of composition of fake rates after applying $\geq 2jet$ requirement for $\mu\mu$ and ee final states.

The resulting uncertainty is then propagated to the fake rates as measured in data where a bin-by-bin uncertainty can be defined. This uncertainty accounts for the variation between fake rates in different processes represented in the signal region (mainly $t\bar{t}$ and W +jets) and statistical variation in the fake rate in the measurement region (dominated by multijet QCD and Z +jets). This is shown in figure 5.35.

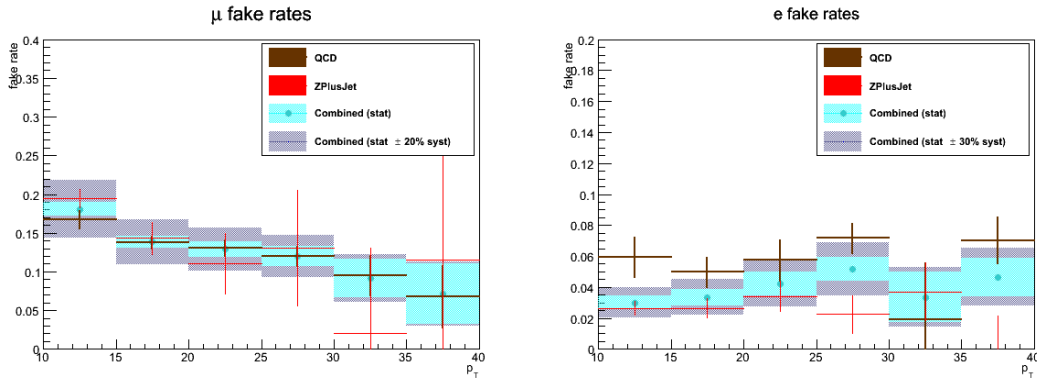


Figure 5.35. Fake rates measured from data (combined QCD and Z +jet rates) parameterized as a function of p_T for muons (left) and electrons (right). Error bands include both statistical and systematic uncertainties.

To propagate the fake rate uncertainty to the final yields, a weighted average of the bin-by-bin fake rate uncertainties is calculated using the relative contribution from each bin based on the template (figure 5.36 used for the background estimation). The uncertainties per bin and their relative contribution are shown in table 5.9. Based on this study, uncertainties of 30% and 40% are used for the component of the fake background arising from non-prompt muons and electrons, respectively.

p_T (GeV)	10-15	15-20	20-25	25-30	30-35	35-40	> 40
μ							
bin error	20.5%	20.8%	21.5%	22.8%	34.1%	58.4%	49.7%
contribution	27.9%	17.6%	13.1%	10.8%	6.8%	5.7%	18%
e							
bin error	33.3%	34.0%	35.2%	33.4%	57.4%	40.1%	41.9%
contribution	7.7%	11.6%	16.0%	11.9%	5.1%	4.0%	44 %

Table 5.9. Bin-by-bin contribution to the fake rate uncertainty for muons (top) and electrons (bottom).

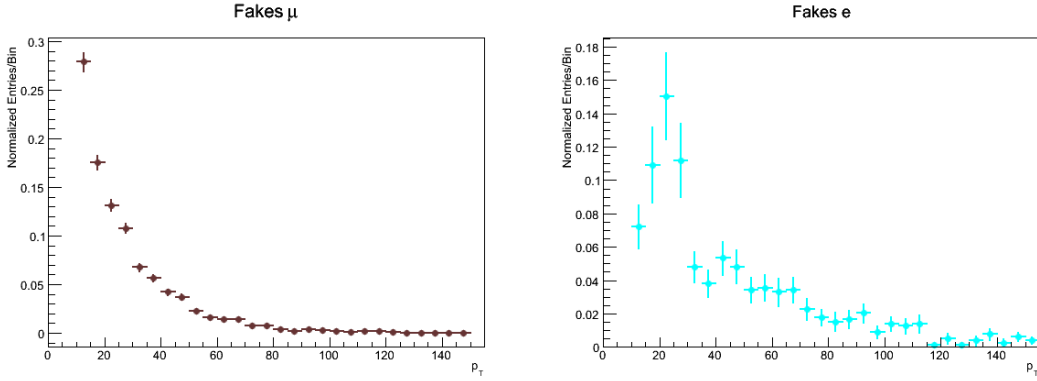


Figure 5.36. Templates used in the estimation of the fake background for muons (left) and electrons (right).

5.4.4. Charge Misidentification

The probability to mismeasure the charge of a lepton can be a significant source of background in the same-sign dilepton final state when there is one or more electrons are present. Even though the probability for mismeasuring the charge of an electron is quite low ($\sim 0.1\%$), the production rate of opposite sign dilepton pairs is very high in comparison to processes that can result in real same sign final states. The probability of a mis-measuring the charge of a muon is found to be negligible ($\lesssim 10^{-6}$).

Several additional cuts are applied to same-sign dielectron events to reduce the contamination from charge mis-identification. The transverse impact parameter of the electrons is required to be less than 0.005 cm from the primary vertex of the event (the nominal POG recommended cut is 0.015 cm). A comparison of the background modelling before and after including this requirement is shown in figure 5.37. There is also a very high probability of charge being mismeasured at high η as can be seen in figure 5.38. To reduce the contribution from these events, electrons with $|\eta| > 2.1$ are not considered for same-sign dielectron events.

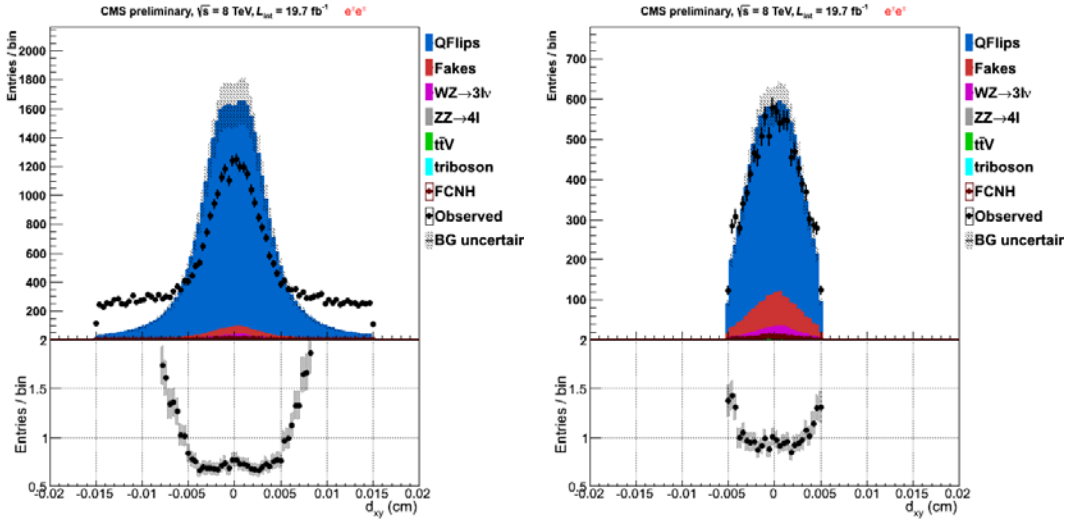


Figure 5.37. Transverse impact parameter of electrons in same-sign dielectron events before (left) and after (right) tightening the cut from 0.015 cm to 0.005 cm.

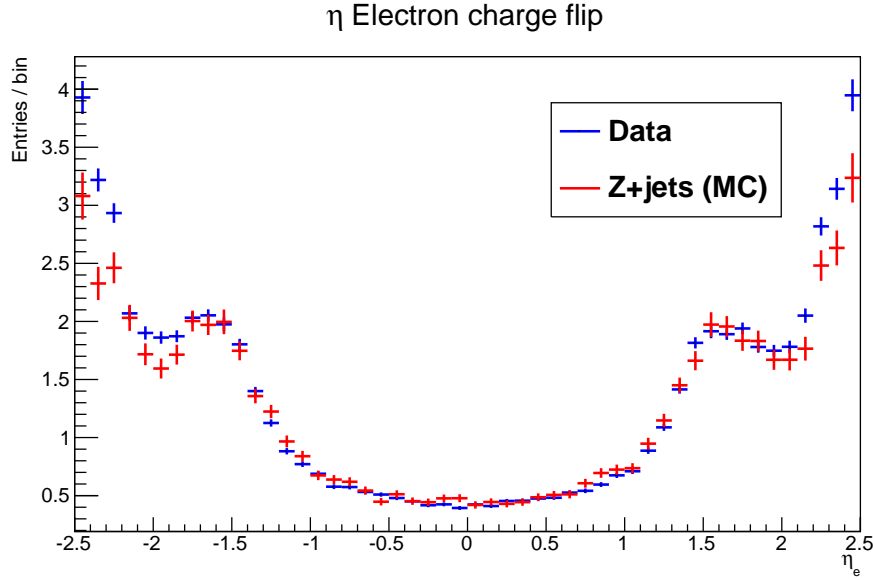


Figure 5.38. Charge flip η dependence in both data and Z+jets MC.

In order to estimate the probability for charge mis-identification from data, a control region consisting of dielectron events where the mass of the dielectron pair is found to be consistent with the mass of the Z ($|M_{ee} - M_Z| < 15 \text{ GeV}$) is selected. This control region is divided based on whether the dielectron pair is same-sign or opposite-sign. It is assumed that events that end up in the same-sign region are dominated by charge mis-identification of one of the two electrons in the pair. This can be seen to largely be the case in simulation figure 5.39. The discrepancy between data and MC in the same-sign dielectron case motivates our use of this data-driven approach since it is clear that the MC systematically underestimates the contribution. It can also be noted that given that the ratio between data and MC is flat, the discrepancy must arise due to the underestimation of Z decays.

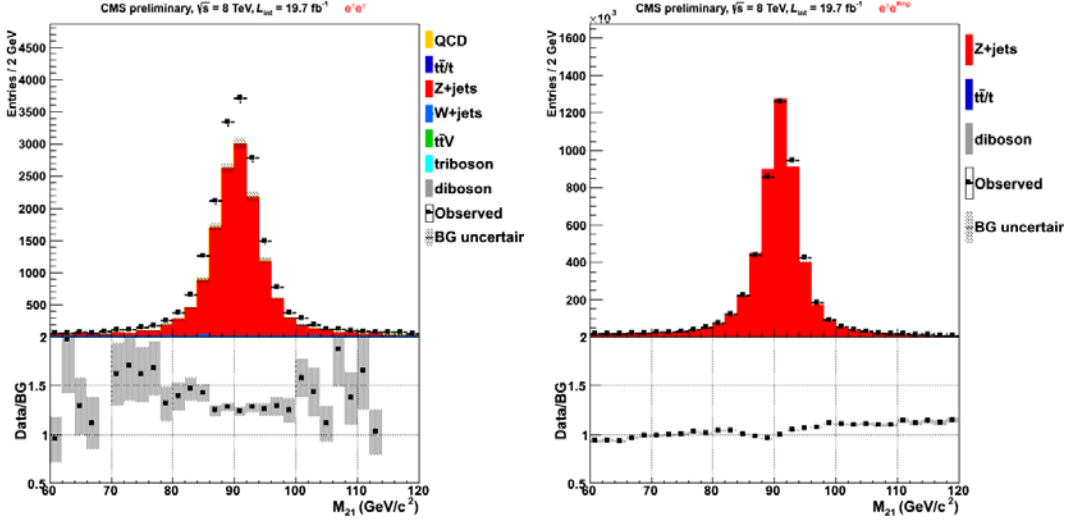


Figure 5.39. Dielectron mass for same-sign (left) and opposite-sign (right) pairs near the Z mass.

The probability for the an electron's charge to be mis-measured has multiple dependencies. The ones that are taken into account are the electron's p_T and η , and the multiplicity of jets in the event. The jet multiplicity dependence is modelled by splitting the p_T and η parameterization in two jet bins, $N_{jets} < 2$ and $N_{jets} \geq 2$. Only the higher jet multiplicity bin is important for signal extraction, but it is useful to have correct modelling for the 0-jet and 1-jet bins for cut optimization and having a control region for cross-checks. In each jet bin, the probability of sign flips is measured in 9×9 dielectron bins of p_T and η . The binning can be summarized,

- p_T : $[10, 30]$; $[30, 60]$; $[60, \text{inf}]$
- η : $[0, 0.8]$; $[0.8, 1.479]$; $[1.479, 2.1]$
- N_{jets} : $[0, 1]$, $[2, \text{inf}]$.

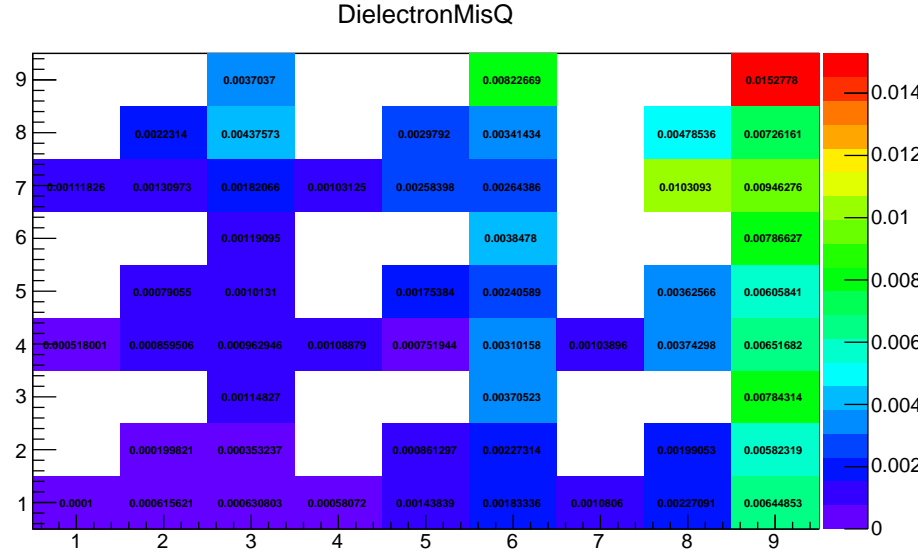


Figure 5.40. Two dimensional charge mis-identification rates for dielectron events.

The two dimensional rates with both jet bins combined are shown in figure 5.40. The relation between the two dimensional dielectron charge flip probability and the probability for a single electron to flip charge can be written,

$$(5.13) \quad P(p_{T,i}, \eta_i; p_{T,j}, \eta_j) \approx P(p_{T,i}, \eta_i) + P(p_{T,j}, \eta_j),$$

which ignores terms of second order, e.g. $p_{T,i}p_{T,j}$. Using this expression and the 2D dilepton charge flip probability, a one dimensional, single electron parameterization of the electron charge flip probability can be determined by averaging over each filled bin bin. The resulting one-dimensional probabilities are shown in figure 5.41.

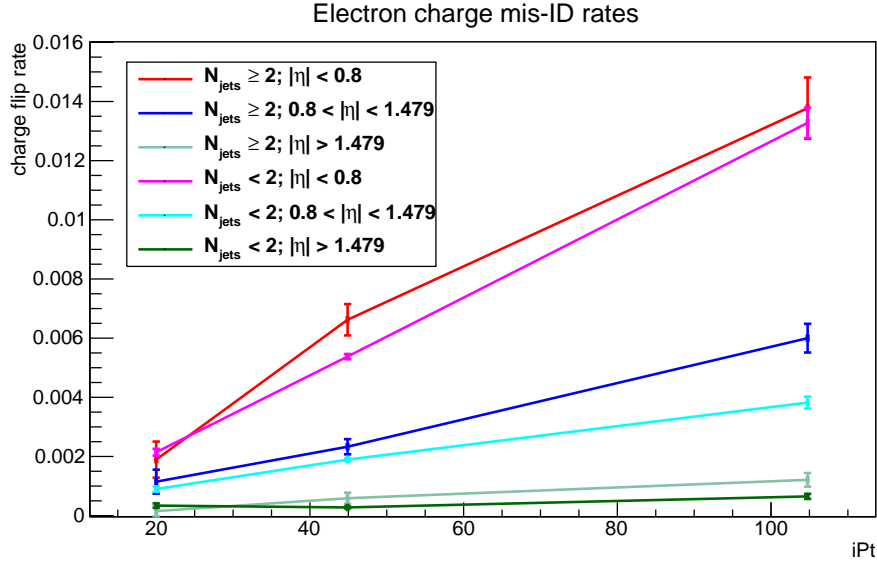


Figure 5.41. Charge mis-identification probabilities parameterized by p_T for different η bins and jet multiplicities.

Once the single electron rates are extracted they can be applied to weight opposite-sign dielectron events in our signal region. The signal region selection requires that same-sign dielectron events within 15 GeV of the Z mass be vetoed making this region orthogonal to the measurement region. To determine if extrapolation to the signal region is valid, simulated Z+jet events were considered to determine if the charge mis-identification is consistent between on-shell and off-shell Z production. In this case, the charge mis-identification rate is taken directly from MC-truth information. Based on this study, it can be concluded that the charge mis-identification is consistent between the measurement and signal regions (shown in figure 5.42).

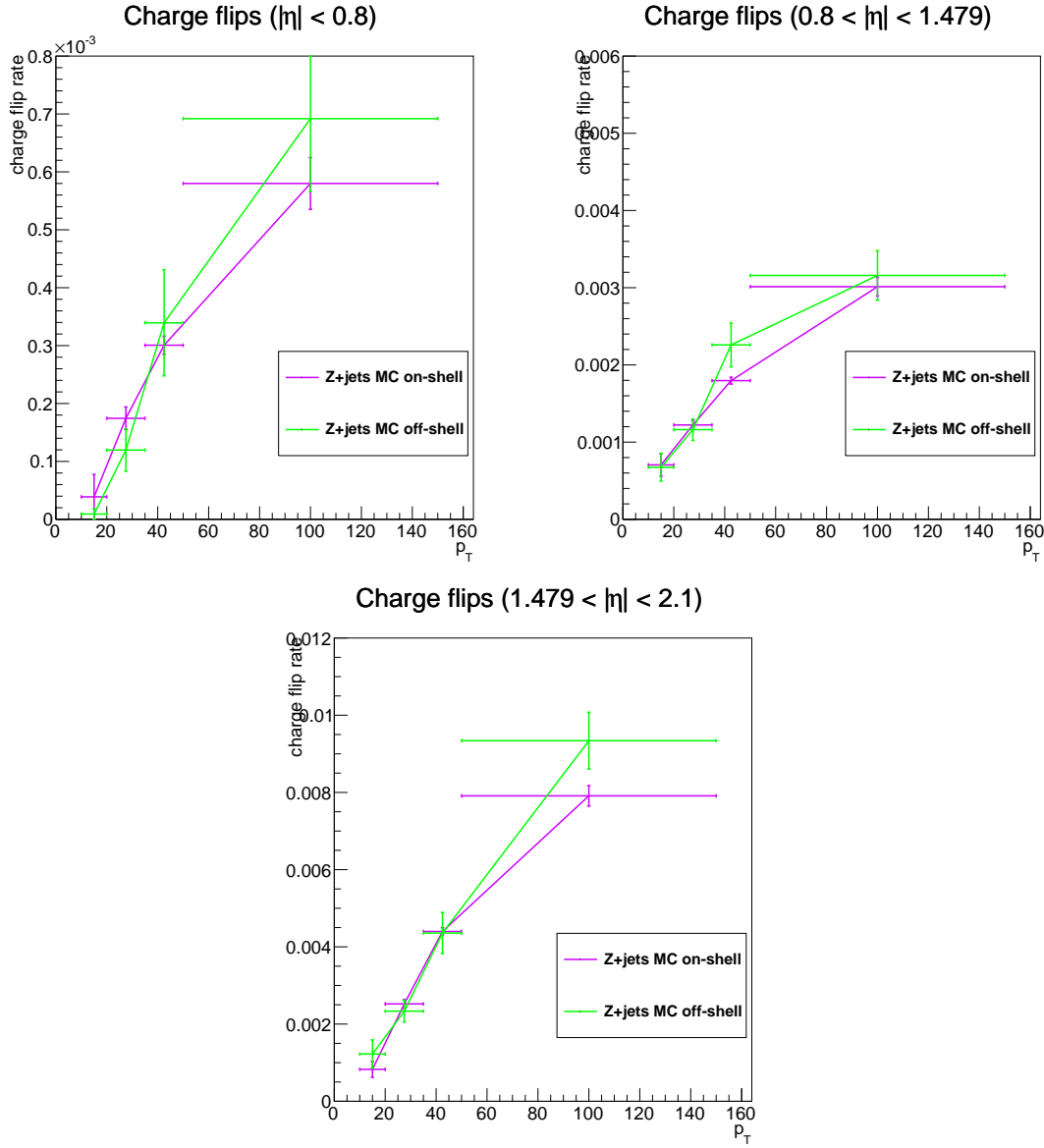


Figure 5.42. Comparison of charge flips measured using MC for events inside and outside a 30 GeV window centered on the Z mass for electrons with $|\eta| < 0.8$ (top left), $0.8 < |\eta| < 1.479$ (top right), and $|\eta| > 0.1479$ (bottom).

5.5. Systematics

Systematic uncertainties are largely introduced through background prediction models. In the case of data-driven backgrounds, the uncertainty comes from the statistics of the control region used to derive the background estimate or from the differences between the background control region and signal region in terms of composition (e.g., jet flavor of fake measurement region versus the signal region). Based on the work shown in section 5.4.3.4, an estimate of 20% on the uncertainty of the fake rate determination is used. Uncertainty on the charge mis-identification is based on comparison of the charge mis-identification in different simulated samples and different mass regions as shown in 5.4.3.4. For the case of simulated background models, there is uncertainty from the scaling of the sample, both from the assumed luminosity [43] and the cross-section of the process being modeled.

A number of corrections are applied to both data and MC which are also a source of uncertainty. Common to both are corrections to account for jet energy scale (JES) [56], MET and correction to lepton p_T [50, 53]. For the simulated samples, the efficiency of the lepton isolation and triggers is taken into account as well as the modelling of the pileup.

Uncertainty on the lepton selection criteria is assessed by adjusting the scale factors up or down by their individual uncertainties. For muons, the uncertainty per scale factor is 0.5% (ID) + 0.2% (ISO) + statistical which translates to an uncertainty of 1% per muon on the final yield. For electrons, a similar analysis finds a 2% uncertainty per electron.

Trigger efficiencies are treated in the same manner as the selection efficiencies. Taken from [44] for both double muon and electron triggers. The uncertainty on the MuEG triggers is inferred from the uncertainties observed on the efficiencies of the same-flavor

double lepton triggers. It is increased to reflect the fact that there is no correction applied to account for its inefficiencies.

Irreducible backgrounds are mostly estimated from simulated samples and therefore have an uncertainty associated with their normalization. The normalization for the $WZ \rightarrow 3\ell\nu$ is checked in section 5.4.1, and is seen to agree at the 1% level. For backgrounds originating from $t\bar{t}W$ and $t\bar{t}Z$, the theory uncertainties on the cross-section of 11% and 13% [59] are used.

Uncertainty on the pileup is attributable to the weighting procedure for matching the pileup in simulated samples to the pileup in data. For the same-sign dilepton channel, this is not significant since most of the background estimation is based on data-driven methods. The accuracy of the weighting procedure can be gauged from the opposite-sign dilepton events where good agreement is observed. An uncertainty of 1% is used.

PDF uncertainties for the signal model are taken into account according to the PDF4LHC working group recommendations [62]. Events are generated using the CT10 PDF set for which there are 26 associated eigenvectors. The uncertainty for an individual event is the average of the errors of each of these eigenvectors. To assess the resulting uncertainty on signal acceptance, the analysis is rerun with each event either being scaled up or down by the PDF uncertainty. When compared to the nominal signal yield, the overall effect after all the analysis cuts are applied is about 6%.

The systematics are summarized in table 5.10, and are taken into account in the process of setting the limit on $BR(t \rightarrow Hq)$.

systematic source	trilepton (%)	same-sign dilepton (%)
luminosity	2.6	2.6
jet energy scale	0.5	0.5
MET resolution	4	4
WZ normalization	15	15
ttV normalization	11-13	11-13
electron fake rates	40	40
muon fake rates	30	30
charge mis-ID (electrons only)	N/A	20
trigger (double muon)	N/A	1.
trigger (double electron)	N/A	2.
trigger (muEG)	N/A	2.
muon ID/ISO SF	1-3	1-2
electron ID/ISO SF	2-6	2-4
pileup	1	1
PDF uncertainties	6	6

Table 5.10. Sources of systematic uncertainty and the approximate effect on percent uncertainty of the yields.

5.6. Results

In the triplepton and same-sign dilepton selections, 86.2 ± 9.3 and 654.3 ± 73.1 events are expected, respectively, from the SM background processes and 79 and 631 events are observed, respectively. No excess beyond the SM background is observed and a 95% CL upper limit on the branching fraction of $t \rightarrow Hc$ is determined using the modified frequentist approach (CLs method [63, 64]). A summary of the observed and expected limits are presented in Table 5.11.

The signal event yield is obtained from the efficiency times acceptance and branching fraction for simulated events. As $\mathcal{B}(t \rightarrow Hc)$ is expected to be small, the possibility of both top quarks decaying via flavor changing neutral Higgs boson is not considered.

The observed and expected 95% CL upper limits on the branching fraction $\mathcal{B}(t \rightarrow Hc)$ are 0.93% and 0.89%, respectively, obtained from the combined trilepton and same-sign dilepton analyses. The one-sigma boundaries of the expected limits are 0.65 – 1.22%. The expected limits for the trilepton and same-sign dilepton selections show that they have comparable sensitivity.

The limit on the FCNH branching fraction can be translated into a limit on the left- and right-handed Yukawa couplings using the relation [65],

$$(5.14) \quad \mathcal{B}(t \rightarrow Hc) \simeq 0.29 \left(|\lambda_{tc}^H|^2 + |\lambda_{ct}^H|^2 \right).$$

This results in an observed upper limit of $\sqrt{|\lambda_{tc}^H|^2 + |\lambda_{ct}^H|^2} < 0.18$.

	$-\sigma$	$\mathcal{B}_{exp}(t \rightarrow Hc)$	$+\sigma$	$\mathcal{B}_{obs}(t \rightarrow Hc)$
trilepton	0.95	1.33	1.87	1.26
same-sign dilepton	0.68	0.93	1.26	0.99
combined	0.65	0.89	1.22	0.93

Table 5.11. Upper limits at 95% CL on branching fraction of $t \rightarrow Hc$ for three leptons, same-sign dilepton, and combined selections.

5.7. Conclusions

A search for a flavor changing neutral Higgs boson in top quark decays based on $\sqrt{s} = 8$ TeV proton-proton collisions has been presented. A sample of trilepton and same-sign dilepton events were selected from data recorded by CMS during 2012 corresponding to an integrated luminosity of 19.7 fb^{-1} . These events are selected to enhance the sensitivity to events originating from the process $pp \rightarrow t\bar{t} \rightarrow Hc + Wb$, where the Higgs boson is

decays to WW , ZZ , and $\tau\tau$. No excess of events over the SM background is observed and a $\mathcal{B}(t \rightarrow Hc)$ branching fraction larger than 0.93% is excluded at the 95% confidence level.

References

- [1] E. Yazgan, “Flavor changing neutral currents in top quark production and decay,” pp. 285–294, 2014.
- [2] J. Aguilar-Saavedra, “Top flavor-changing neutral interactions: Theoretical expectations and experimental detection,” *Acta Phys.Polon.*, vol. B35, pp. 2695–2710, 2004.
- [3] G. Eilam, J. L. Hewett, and A. Soni, “Rare decays of the top quark in the standard and two-higgs-doublet models,” *Phys. Rev. D*, vol. 44, p. 1473, 1991. [Erratum-ibid. D 59, 039901 (1999)].
- [4] B. Mele, S. Petrarca, and A. Soddu, “A New evaluation of the t to cH decay width in the standard model,” *Phys. Lett. B*, vol. 435, p. 401, 1998.
- [5] J. Aguilar-Saavedra, “Top flavor-changing neutral interactions: Theoretical expectations and experimental detection,” *Acta Phys.Polon. B*, vol. 35, p. 2695, 2004.
- [6] S. Chatrchyan *et al.*, “The CMS experiment at the CERN LHC,” *JINST*, vol. 3, p. S08004, 2008.
- [7] S. Chatrchyan *et al.*, “Observation of a new boson at a mass of 125 GeV with the CMS experiment at the LHC,” *Phys.Lett.*, vol. B716, pp. 30–61, 2012.

- [8] G. Aad *et al.*, “Observation of a new particle in the search for the Standard Model Higgs boson with the ATLAS detector at the LHC,” *Phys.Lett.*, vol. B716, pp. 1–29, 2012.
- [9] F. Englert and R. Brout, “Broken Symmetry and the Mass of Gauge Vector Mesons,” *Phys.Rev.Lett.*, vol. 13, pp. 321–323, 1964.
- [10] P. W. Higgs, “Broken symmetries, massless particles and gauge fields,” *Phys.Lett.*, vol. 12, pp. 132–133, 1964.
- [11] P. W. Higgs, “Broken Symmetries and the Masses of Gauge Bosons,” *Phys.Rev.Lett.*, vol. 13, pp. 508–509, 1964.
- [12] P. W. Anderson, “Plasmons, Gauge Invariance, and Mass,” *Phys.Rev.*, vol. 130, pp. 439–442, 1963.
- [13] Y. Nambu, “Quasiparticles and Gauge Invariance in the Theory of Superconductivity,” *Phys.Rev.*, vol. 117, pp. 648–663, 1960.
- [14] J. Goldstone, A. Salam, and S. Weinberg, “Broken Symmetries,” *Phys.Rev.*, vol. 127, pp. 965–970, 1962.
- [15] K. Olive *et al.*, “Review of Particle Physics,” *Chin.Phys.*, vol. C38, p. 090001, 2014.
- [16] F. Abe *et al.*, “Observation of top quark production in $\bar{p}p$ collisions,” *Phys.Rev.Lett.*, vol. 74, pp. 2626–2631, 1995.

- [17] S. Abachi *et al.*, “Observation of the top quark,” *Phys.Rev.Lett.*, vol. 74, pp. 2632–2637, 1995.
- [18] “First combination of Tevatron and LHC measurements of the top-quark mass,” 2014.
- [19] M. Czakon and A. Mitov, “Top++: A Program for the Calculation of the Top-Pair Cross-Section at Hadron Colliders,” *Comput.Phys.Commun.*, vol. 185, p. 2930, 2014.
- [20] S. Glashow, J. Iliopoulos, and L. Maiani, “Weak Interactions with Lepton-Hadron Symmetry,” *Phys.Rev.*, vol. D2, pp. 1285–1292, 1970.
- [21] M. Gell-Mann, “A Schematic Model of Baryons and Mesons,” *Phys.Lett.*, vol. 8, pp. 214–215, 1964.
- [22] G. Zweig, “An SU(3) model for strong interaction symmetry and its breaking. Version 2,” pp. 22–101, 1964.
- [23] N. Cabibbo, “Unitary Symmetry and Leptonic Decays,” *Phys.Rev.Lett.*, vol. 10, pp. 531–533, 1963.
- [24] J. Beringer and many more..., “Review of particle physics*,” *Phys. Rev. D*, vol. 86, p. 010001, Jul 2012.
- [25] S. Chatrchyan *et al.*, “Search for Flavor-Changing Neutral Currents in Top-Quark Decays $t \rightarrow Zq$ in pp Collisions at $\sqrt{s} = 8\text{TeV}$,” *Phys.Rev.Lett.*, vol. 112, no. 17, p. 171802, 2014.

- [26] F. Abe *et al.*, “Search for flavor-changing neutral current decays of the top quark in $p\bar{p}$ collisions at $\sqrt{s} = 1.8$ TeV,” *Phys.Rev.Lett.*, vol. 80, pp. 2525–2530, 1998.
- [27] T. A. collaboration, “Search for single top-quark production via FCNC in strong interaction in $\sqrt{s} = 8$ TeV ATLAS data,” 2013.
- [28] V. Khachatryan *et al.*, “Searches for heavy Higgs bosons in two-Higgs-doublet models and for tch decay using multilepton and diphoton final states in pp collisions at 8 TeV,” *Phys.Rev.*, vol. D90, p. 112013, 2014.
- [29] J. Bjorken and S. Weinberg, “A Mechanism for Nonconservation of Muon Number,” *Phys.Rev.Lett.*, vol. 38, p. 622, 1977.
- [30] B. McWilliams and L.-F. Li, “Virtual Effects of Higgs Particles,” *Nucl.Phys.*, vol. B179, p. 62, 1981.
- [31] O. U. Shanker, “Flavor Violation, Scalar Particles and Leptoquarks,” *Nucl.Phys.*, vol. B206, p. 253, 1982.
- [32] T. Cheng and M. Sher, “Mass Matrix Ansatz and Flavor Nonconservation in Models with Multiple Higgs Doublets,” *Phys.Rev.*, vol. D35, p. 3484, 1987.
- [33] W.-S. Hou, “Tree level $t \rightarrow ch$ or $h \rightarrow t$ anti- c decays,” *Phys.Lett.*, vol. B296, pp. 179–184, 1992.
- [34] Particle Data Group, J. Beringer, *et al.*, “Review of Particle Physics,” *Phys. Rev. D*, vol. 86, p. 010001, 2012.

- [35] L. Evans and P. Bryant, “LHC Machine,” *JINST*, vol. 3, p. S08001, 2008.
- [36] V. Khachatryan *et al.*, “CMS Tracking Performance Results from early LHC Operation,” *Eur.Phys.J.*, vol. C70, pp. 1165–1192, 2010.
- [37] P. Adzic *et al.*, “Energy resolution of the barrel of the CMS electromagnetic calorimeter,” *JINST*, vol. 2, p. P04004, 2007.
- [38] “Jet Energy Resolution in CMS at sqrt(s)=7 TeV,” Tech. Rep. CMS-PAS-JME-10-014, CERN, Geneva, 2011.
- [39] “Performance of the CMS missing transverse momentum reconstruction in pp data at $\sqrt{s} = 8$ TeV. Performance of the missing transverse energy reconstruction by the CMS experiment in $\sqrt{s} = 8$ TeV pp data,”
- [40] “Performance of cms muon reconstruction in cosmic-ray events,” *JINST*, vol. **05**, p. T03022, 2010.
- [41] N. Odell, “Measurements of luminosity and normalised beam-induced background using the CMS Fast Beam Condition Monitor,” *PoS*, vol. ICHEP2012, p. 526, 2013.
- [42] J. L. Leonard, A. Bell, P. Burtowy, A. Dabrowski, M. Hempel, *et al.*, “Fast Beam Condition Monitor for CMS: performance and upgrade,” *Nucl.Instrum.Meth.*, vol. A765, pp. 235–239, 2014.
- [43] “CMS Luminosity Based on Pixel Cluster Counting,” Tech. Rep. CMS-PAS-LUM-13-001, CERN, Geneva, 2012.

- [44] “Search for the Higgs boson in $Z+\gamma$ decays,” Tech. Rep. CMS-AN-13-038, CERN, Geneva, 2013.
- [45] T. Sjöstrand, S. Mrenna, and P. Z. Skands, “PYTHIA 6.4 Physics and Manual,” *JHEP*, vol. 05, p. 026, 2006.
- [46] J. Pumplin *et al.*, “New generation of parton distributions with uncertainties from global analysis,” *JHEP*, vol. 07, p. 012, 2002.
- [47] S. Heinemeyer and m. m. many, “Handbook of LHC Higgs Cross Sections: 3. Higgs Properties: Report of the LHC Higgs Cross Section Working Group,” Tech. Rep. arXiv:1307.1347. CERN-2013-004, Geneva, 2013. Comments: 404 pages, 139 figures, to be submitted to CERN Report. Working Group web page: <https://twiki.cern.ch/twiki/bin/view/LHCPhysics/CrossSections>.
- [48] J. Alwall *et al.*, “MadGraph 5: Going beyond,” *JHEP*, vol. 1106, p. 128, 2011.
- [49] S. Frixione, P. Nason, and C. Oleari, “Matching NLO QCD computations with Parton Shower simulations: the POWHEG method,” *JHEP*, vol. 11, p. 070, 2007.
- [50] S. Chatrchyan *et al.*, “Performance of CMS muon reconstruction in pp collision events at $\sqrt{s} = 7$ TeV,” *JINST*, vol. 7, p. P10002, 2012.
- [51] S. Chatrchyan *et al.*, “The performance of the CMS muon detector in proton-proton collisions at $\sqrt{s} = 7$ TeV at the LHC,” *JINST*, vol. 8, p. P11002, 2013.

- [52] S. Baffioni, C. Charlot, F. Ferri, D. Futyan, P. Meridiani, I. Puljak, C. Rovelli, R. Salerno, and Y. Sirois, “Electron reconstruction in CMS,” *Eur. Phys. J. C*, vol. 49, p. 1099, 2007.
- [53] V. Khachatryan *et al.*, “Performance of electron reconstruction and selection with the CMS detector in proton-proton collisions at $\sqrt{s} = 8$ TeV,” 2015.
- [54] CMS Collaboration, “Particle-flow event reconstruction in CMS and performance for jets, taus, and E_T^{miss} ,” CMS Physics Analysis Summary CMS-PAS-PFT-09-001, 2009.
- [55] M. Cacciari, G. P. Salam, and G. Soyez, “The anti- k_t jet clustering algorithm,” *JHEP*, vol. 04, p. 063, 2008.
- [56] CMS Collaboration, “Determination of jet energy calibration and transverse momentum resolution in CMS,” *JINST*, vol. 6, p. 11002, 2011.
- [57] S. Chatrchyan *et al.*, “Identification of b-quark jets with the CMS experiment,” *JINST*, vol. 8, p. P04013, 2013.
- [58] R. C. Gray, C. Kilic, M. Park, S. Somalwar, and S. Thomas, “Backgrounds To Higgs Boson Searches from $W\gamma^* \rightarrow l\nu l(l)$ Asymmetric Internal Conversion,” 2011.
- [59] M. Garzelli, A. Kardos, C. Papadopoulos, and Z. Trocsanyi, “ $t \bar{t} W^\pm$ and $t \bar{t} Z$ Hadroproduction at NLO accuracy in QCD with Parton Shower and Hadronization effects,” *JHEP*, vol. 1211, p. 056, 2012.

- [60] “A Search for Anomalous Production of Events with Three or More Leptons using 19.5 fb^{-1} of $\sqrt{s} = 8 \text{ TeV}$ LHC Data,” Tech. Rep. CMS-AN-12-343, CERN, Geneva, 2013.
- [61] CMS Collaboration, “Search for standard model higgs boson produced in association with top quarks and decaying to leptons,” CMS AN AN-13-159, CERN, 2013.
- [62] M. Botje, J. Butterworth, A. Cooper-Sarkar, A. de Roeck, J. Feltesse, *et al.*, “The PDF4LHC Working Group Interim Recommendations,” 2011.
- [63] T. Junk, “Confidence level computation for combining searches with small statistics,” *Nucl. Instrum. Meth. A*, vol. 434, p. 435, 1999.
- [64] A. L. Read, “Presentation of search results: the CL_s technique,” *J. Phys. G*, vol. 28, p. 2693, 2002.
- [65] N. Craig, J. A. Evans, R. Gray, M. Park, S. Somalwar, *et al.*, “Searching for $t \rightarrow ch$ with Multi-Leptons,” *Phys. Rev. D*, vol. 86, p. 075002, 2012.
- [66] J. Therhaag, “TMVA: Toolkit for multivariate data analysis,” *AIP Conf.Proc.*, vol. 1504, pp. 1013–1016, 2009.
- [67] A. Bell, E. Castro, R. Hall-Wilton, W. Lange, W. Lohmann, *et al.*, “Fast Beam Conditions Monitor BCM1F for the CMS Experiment,” *Nucl.Instrum.Meth.*, vol. A614, pp. 433–438, 2010.

- [68] A. E. Dabrowski *et al.*, “The performance of the Beam Conditions and Radiation Monitoring System of CMS,” pp. 489–495, 2011.
- [69] S. van der Meer, “Calibration of the Effective Beam Height in the ISR,” 1968.

APPENDIX A

Supplemental analysis material

A.1. Analysis distributions by flavor category

This appendix collects relevant analysis variables for all lepton flavor categories used in this analysis for each of the cut levels as well as the corresponding event yields.

	Rare	$WZ \rightarrow 3l\nu$	$Non - prompt$	BG	$Data$	$t \rightarrow Hc$
ss dilepton	57.3 ± 3.5	199.2 ± 15.6	49.3 ± 19.8	325.9 ± 25.5	308	2.9 ± 0.2
Z removal	5.8 ± 0.4	11.9 ± 1.0	5.2 ± 2.1	24.7 ± 2.4	28	1.6 ± 0.2
2+ jets	1.9 ± 0.2	1.7 ± 0.2	1.0 ± 0.5	4.8 ± 0.6	7	1.2 ± 0.1

Table A.1. Event yields for trilepton category with eee final states.

	Rare	$WZ \rightarrow 3l\nu$	$Non - prompt$	BG	$Data$	$t \rightarrow Hc$
ss dilepton	72.7 ± 3.2	303.5 ± 19.8	134.7 ± 38.4	526.1 ± 43.3	498	11.7 ± 0.7
Z removal	13.5 ± 0.7	26.4 ± 1.8	32.9 ± 8.6	74.5 ± 8.8	62	8.7 ± 0.5
2+ jets	5.8 ± 0.5	3.8 ± 0.3	12.2 ± 3.3	21.9 ± 3.3	20	6.0 ± 0.4

Table A.2. Event yields for trilepton category with $ee\mu$ final states.

	Rare	$WZ \rightarrow 3l\nu$	$Non - prompt$	BG	$Data$	$t \rightarrow Hc$
ss dilepton	120.2 ± 5.2	389.9 ± 22.5	187.6 ± 48.2	753.4 ± 53.5	703	16.7 ± 0.8
Z removal	20.8 ± 0.9	38.8 ± 2.3	72.4 ± 18.8	140.1 ± 18.9	113	13.1 ± 0.7
2+ jets	8.3 ± 0.6	5.1 ± 0.4	24.5 ± 6.9	38.4 ± 6.9	29	9.0 ± 0.5

Table A.3. Event yields for trilepton category with $e\mu\mu$ final states.

	Rare	$WZ \rightarrow 3l\nu$	$Non - prompt$	BG	$Data$	$t \rightarrow Hc$
ss dilepton	130.2 ± 5.5	559.3 ± 32.7	253.7 ± 74.9	1004.9 ± 81.9	1046	8.7 ± 0.5
Z removal	14.3 ± 0.7	39.8 ± 2.4	39.6 ± 11.8	101.5 ± 12.1	106	4.6 ± 0.3
2+ jets	3.6 ± 0.3	5.2 ± 0.4	12.0 ± 3.7	21.4 ± 3.7	23	3.0 ± 0.2

Table A.4. Event yields for trilepton category with $\mu\mu\mu$ final states.

	Rare	$WZ \rightarrow 3l\nu$	Charge Mis-ID	$Non - prompt$	BG	$Data$	$t \rightarrow Hc$
ss dilepton	167.3 ± 4.8	347.9 ± 19.2	347.9 ± 19.2	6844.0 ± 1641.8	7359.1 ± 1642.0	7442	136.0 ± 6.4
Z removal	167.3 ± 4.8	347.9 ± 19.2	347.9 ± 19.2	6844.0 ± 1641.8	7359.1 ± 1642.0	7442	136.0 ± 6.4
2+ jets	73.1 ± 3.5	72.8 ± 4.1	72.8 ± 4.1	757.7 ± 202.0	903.6 ± 202.1	871	113.1 ± 5.3
MET	43.5 ± 2.4	26.0 ± 1.5	26.0 ± 1.5	194.7 ± 57.2	264.2 ± 57.3	234	59.9 ± 2.9

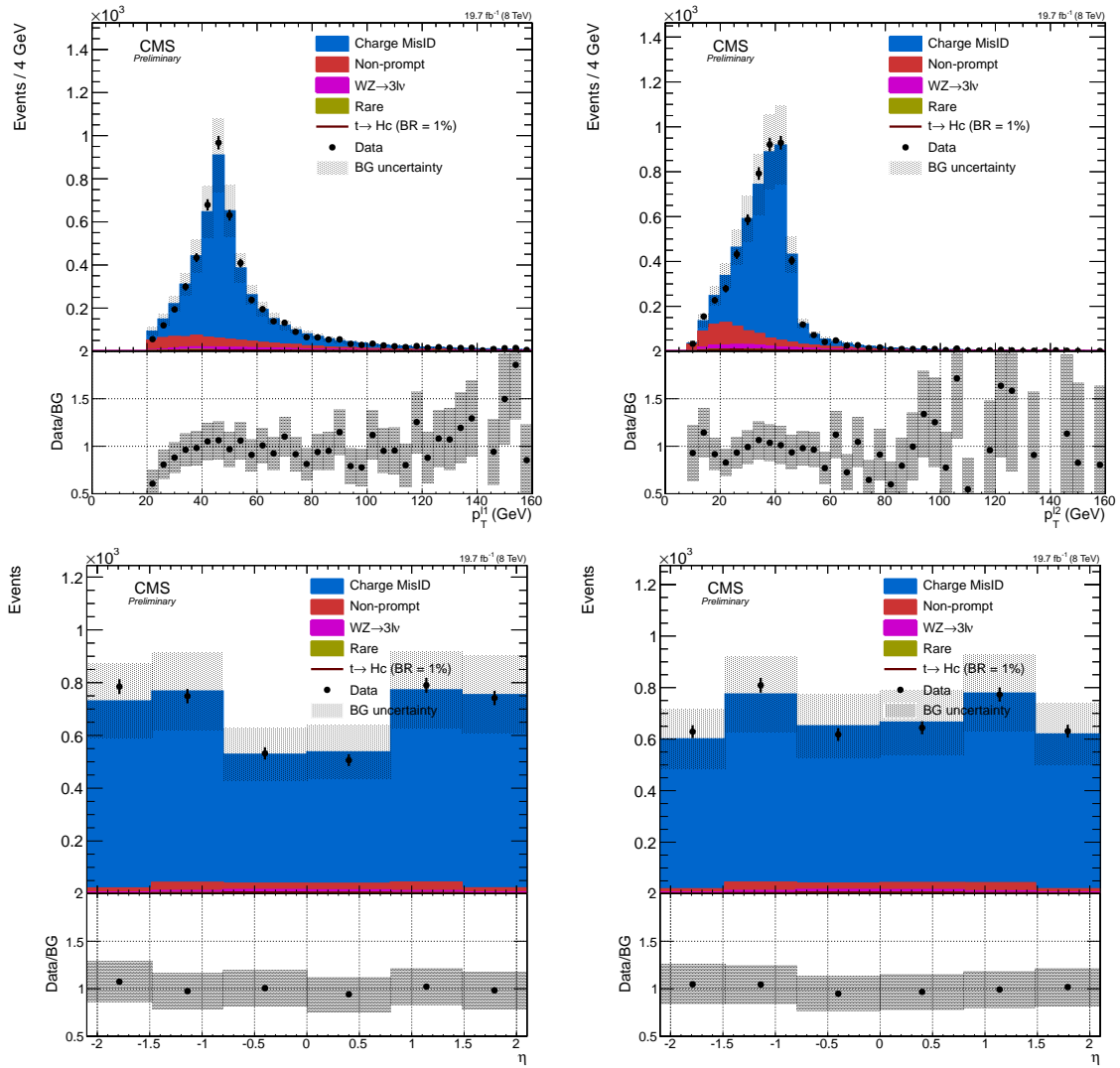
Table A.5. Event yields for same-sign dilepton category with $\mu\mu$ final states.

	Rare	$WZ \rightarrow 3l\nu$	Charge Mis-ID	Non-prompt	BG	$Data$	$t \rightarrow Hc$
ss dilepton	84.0 ± 3.3	175.8 ± 11.9	4323.7 ± 865.0	717.6 ± 257.7	5301.2 ± 902.7	5244	58.7 ± 3.2
Z removal	67.2 ± 2.7	137.6 ± 9.3	437.5 ± 87.5	567.1 ± 203.4	1209.5 ± 221.7	1140	43.5 ± 2.4
2+ jets	33.2 ± 1.9	38.3 ± 2.7	60.9 ± 12.2	102.6 ± 38.5	235.0 ± 40.5	234	36.1 ± 2.0
MET	18.6 ± 1.5	13.2 ± 1.0	11.9 ± 2.4	22.3 ± 9.0	65.9 ± 9.5	73	19.0 ± 1.1

Table A.6. Event yields for same-sign dilepton category with ee final states.

	Rare	$WZ \rightarrow 3l\nu$	$ChargeMisID$	$Non - prompt$	BG	$Data$	$t \rightarrow Hc$
ss dilepton	261.1 ± 7.5	556.4 ± 31.1	83.6 ± 16.7	3082.6 ± 681.5	3983.7 ± 682.5	4104	198.5 ± 9.5
Z removal	261.1 ± 7.5	556.4 ± 31.1	83.6 ± 16.7	3082.6 ± 681.5	3983.7 ± 682.5	4104	198.5 ± 9.5
2+ jets	119.2 ± 5.2	131.1 ± 7.4	40.7 ± 8.1	701.1 ± 170.7	992.1 ± 171.1	927	164.8 ± 7.9
MET	66.4 ± 3.3	44.8 ± 2.6	20.3 ± 4.1	192.8 ± 51.1	324.2 ± 51.4	324	88.1 ± 4.3

Table A.7. Event yields for same-sign dilepton category with $e\mu$ final states.

A.1.1. $e^\pm e^\pm$ Figure A.1. Kinematic distributions for $e^\pm e^\pm$ at preselection level.

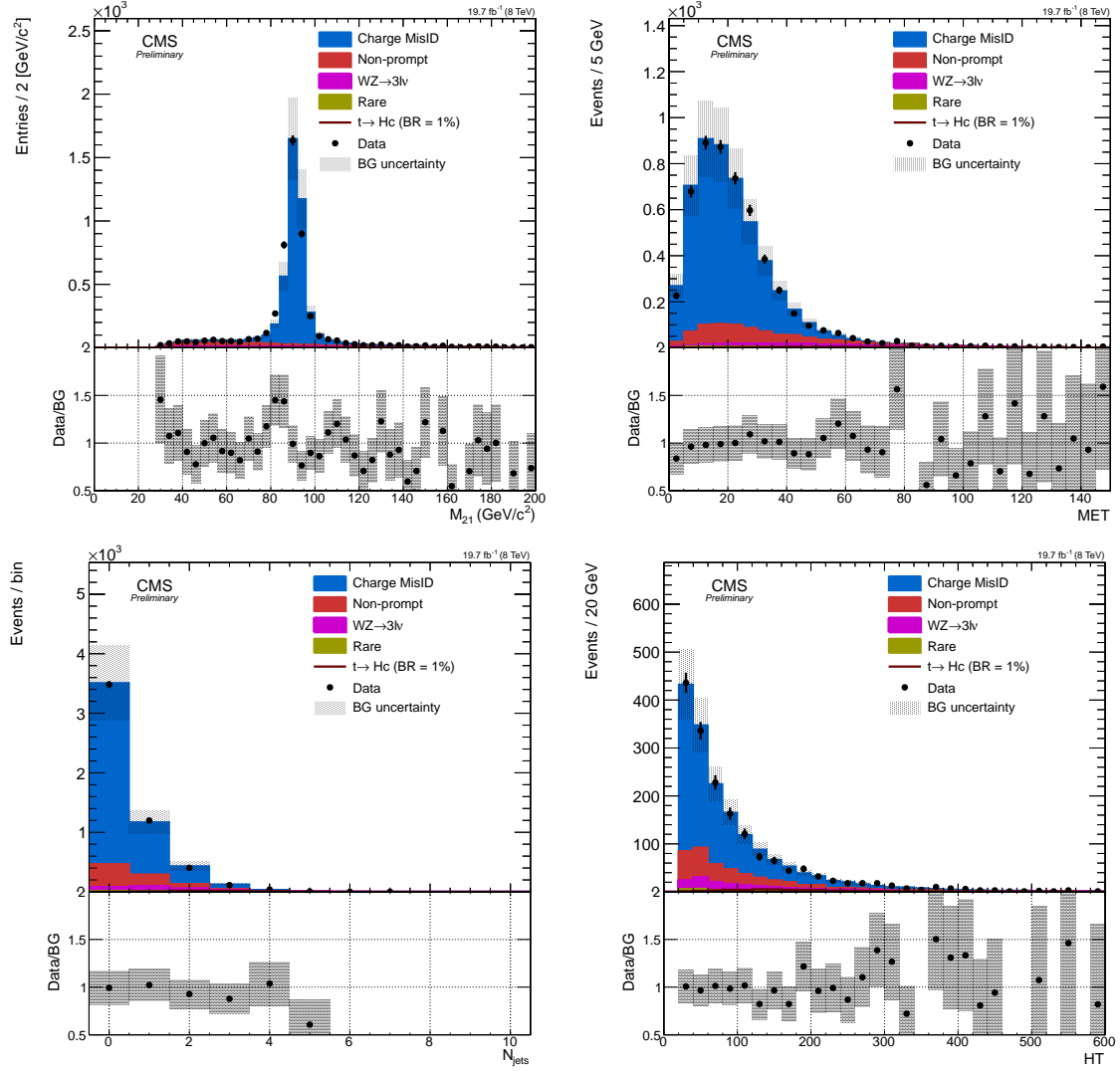
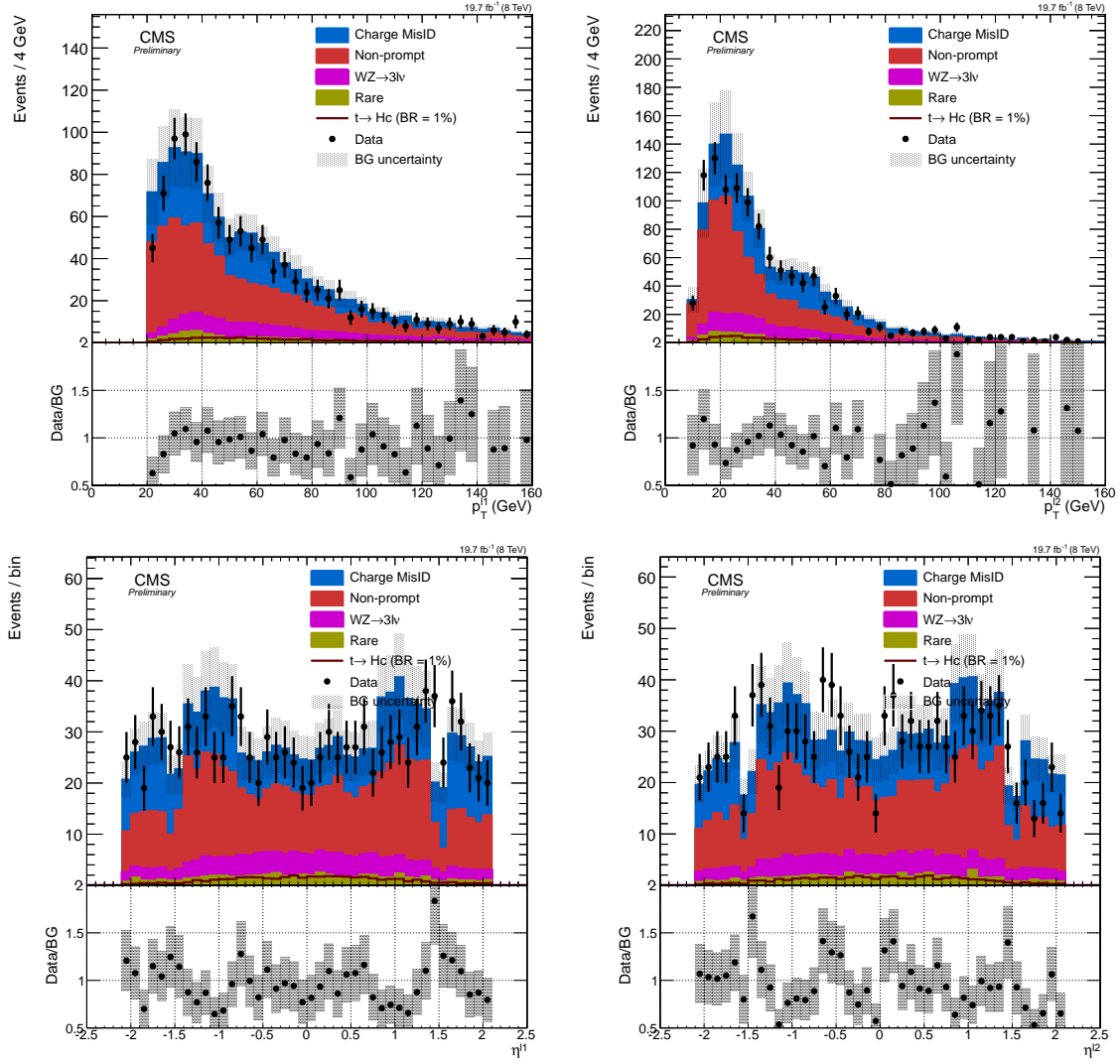
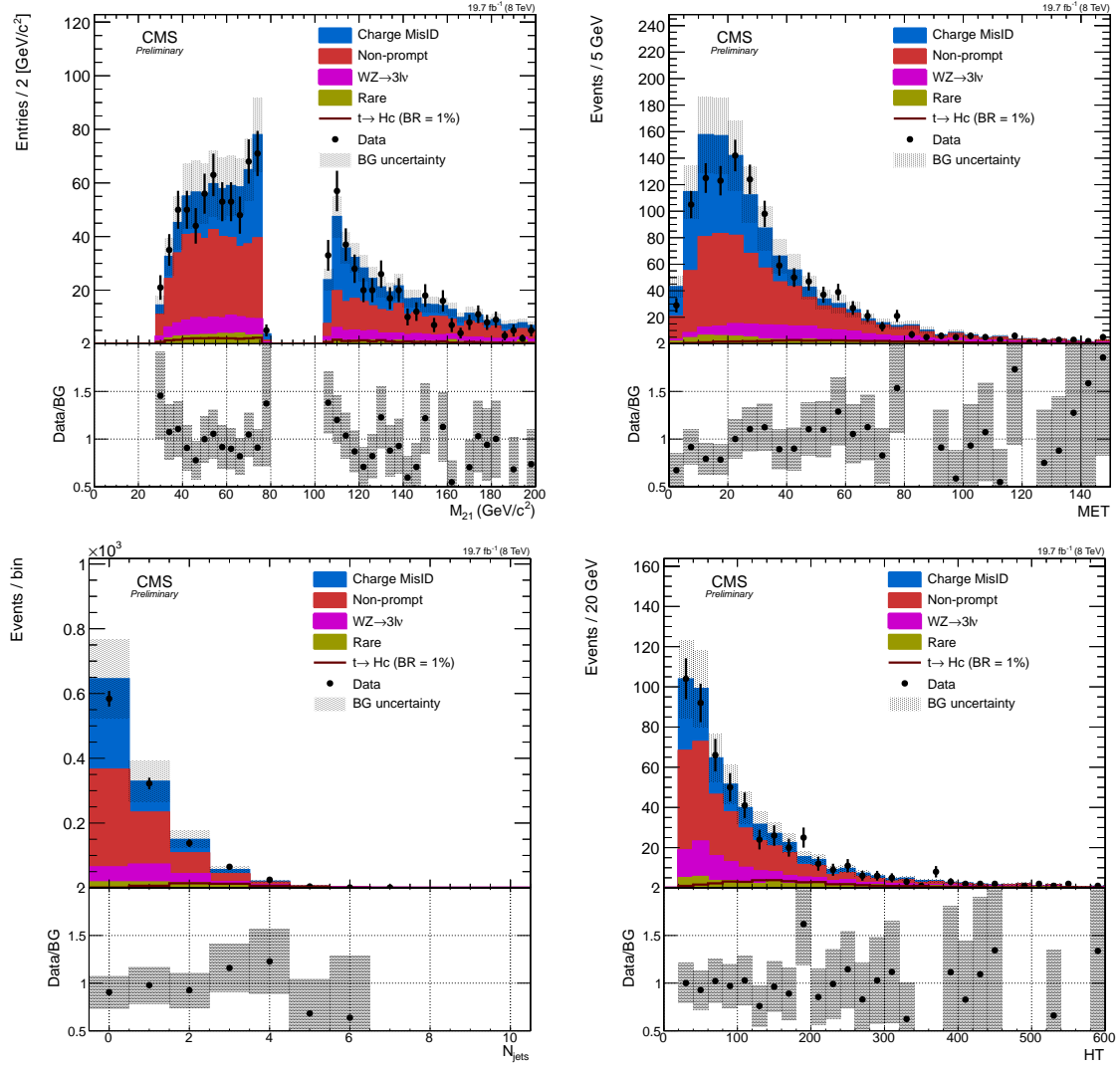


Figure A.2. Analysis variables for $e^\pm e^\pm$ at preselection level.

Figure A.3. Kinematic distributions for $e^\pm e^\pm$ after Z veto.

Figure A.4. Analysis variables for $e^\pm e^\pm$ after Z veto

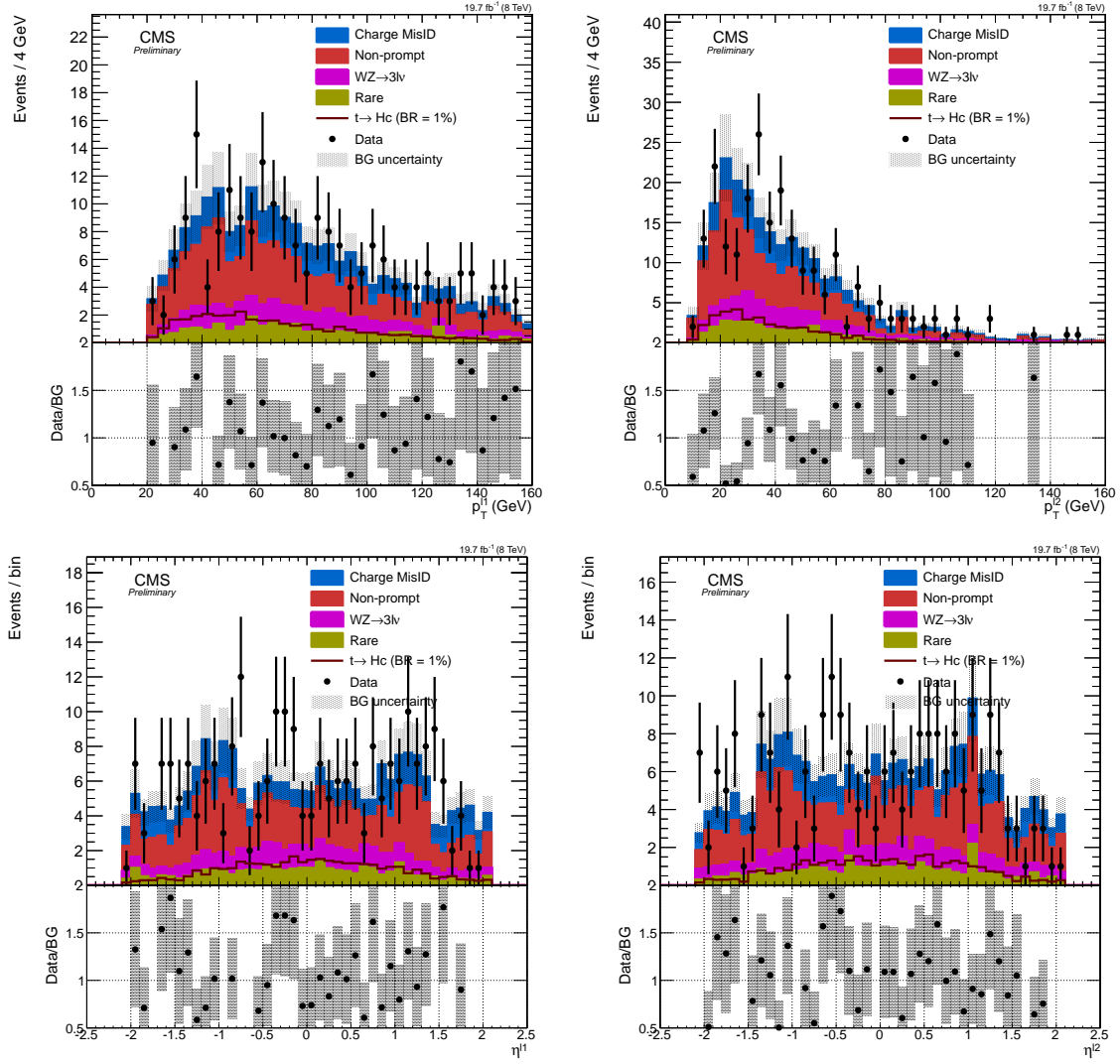


Figure A.5. Kinematic distributions for $e^\pm e^\pm$ after 2 jet requirement.

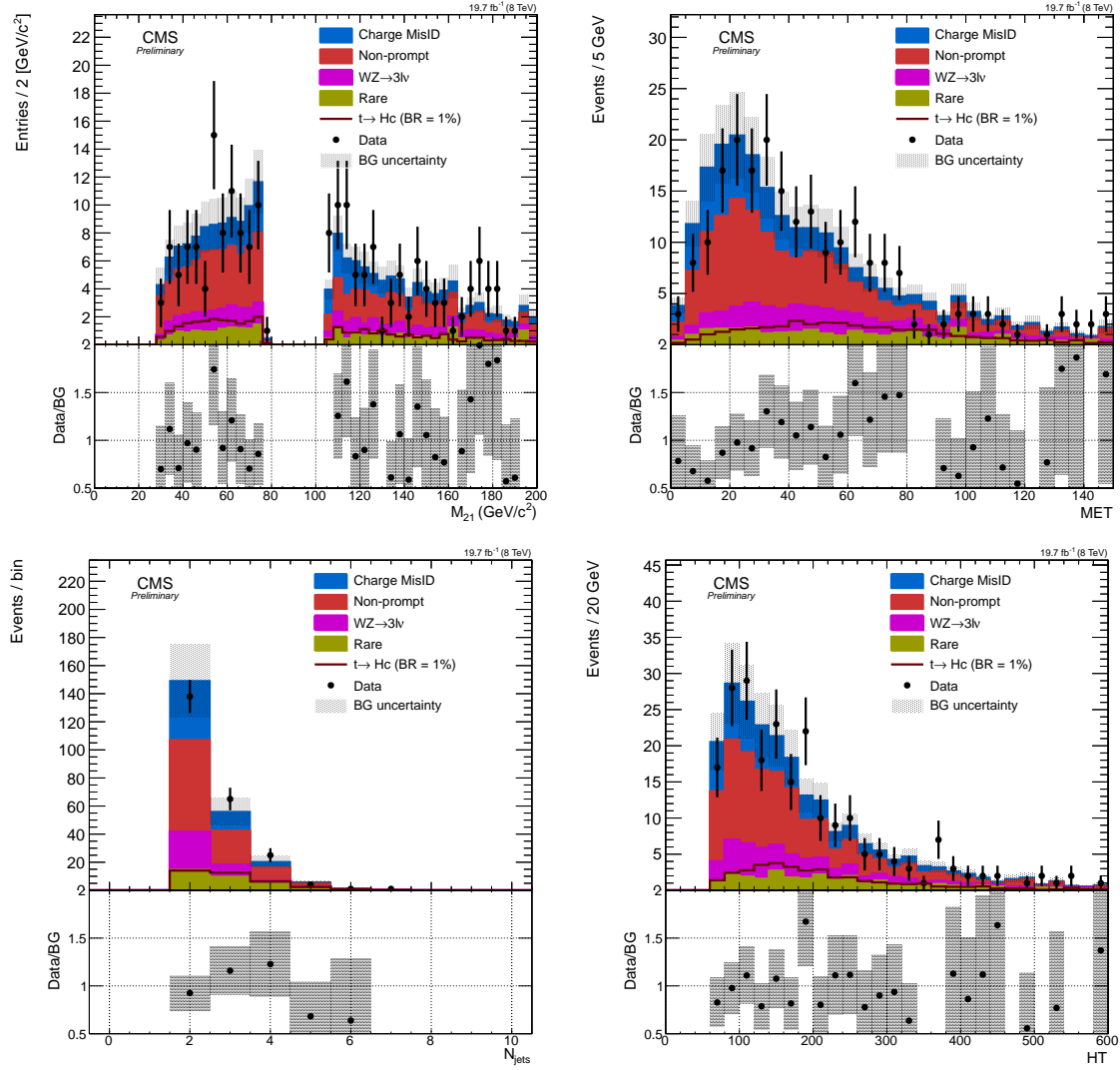


Figure A.6. Analysis variables for $e^\pm e^\pm$ after 2 jet requirement.

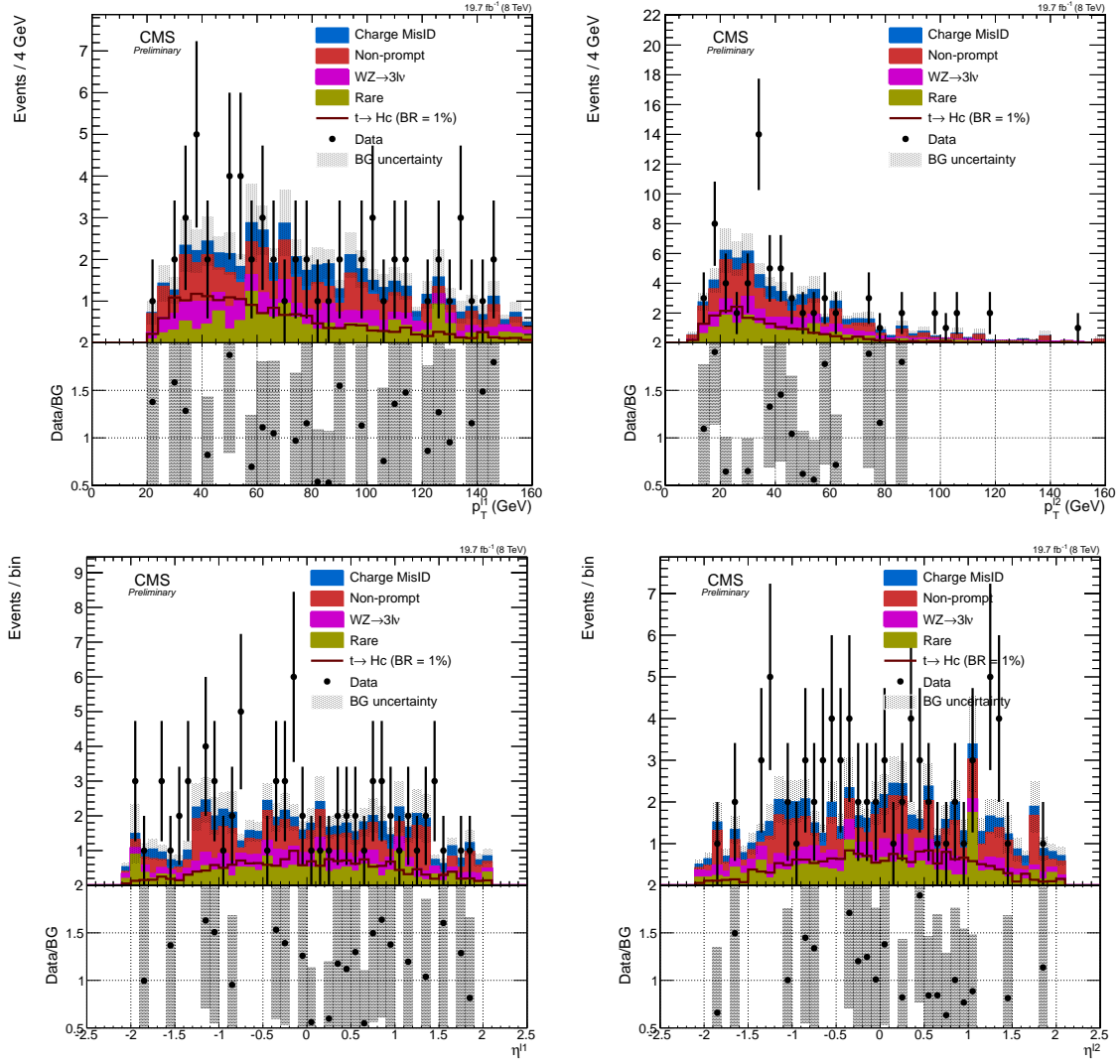


Figure A.7. Kinematic distributions for $e^\pm e^\pm$ after MET and HT cuts.

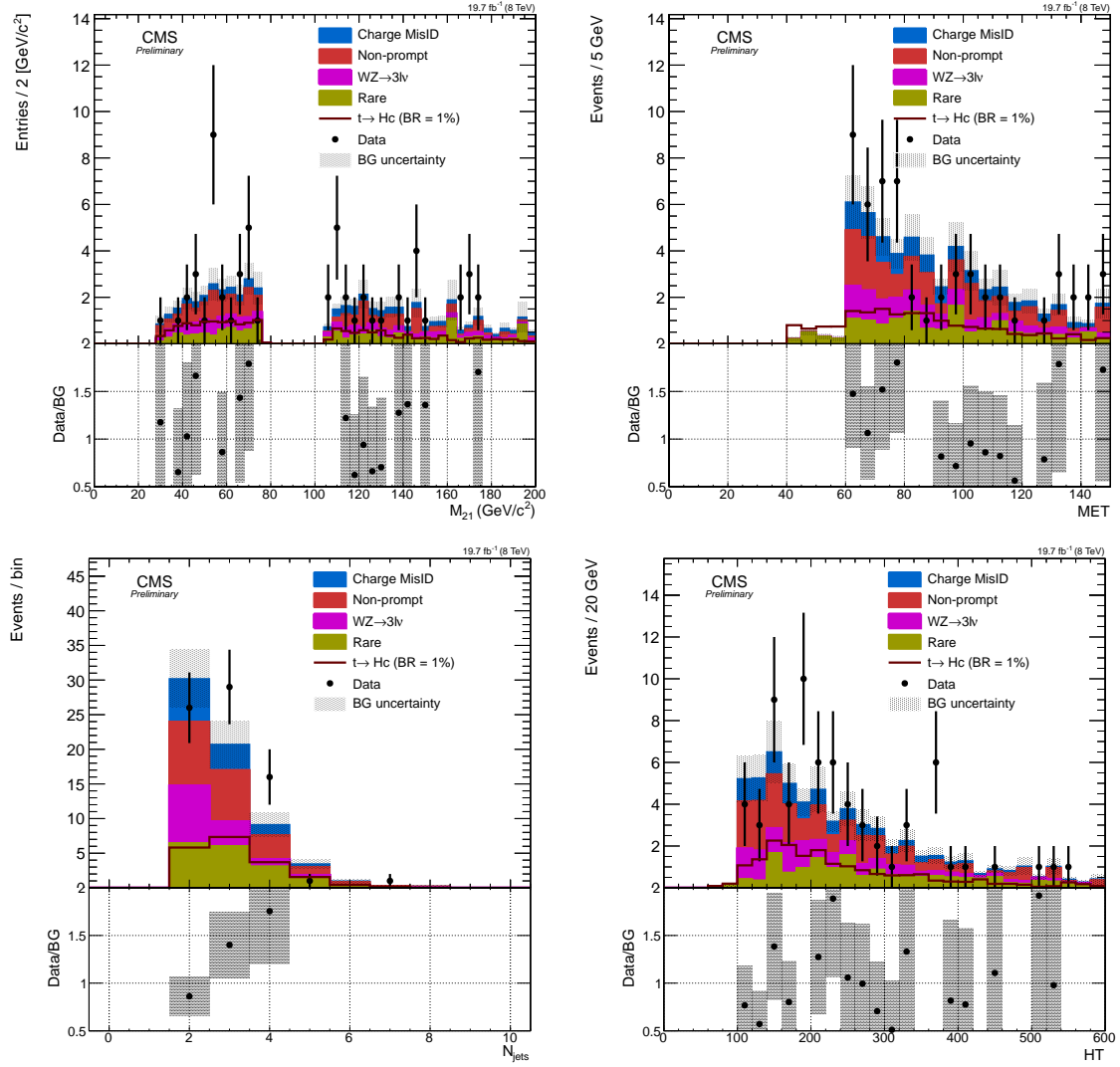
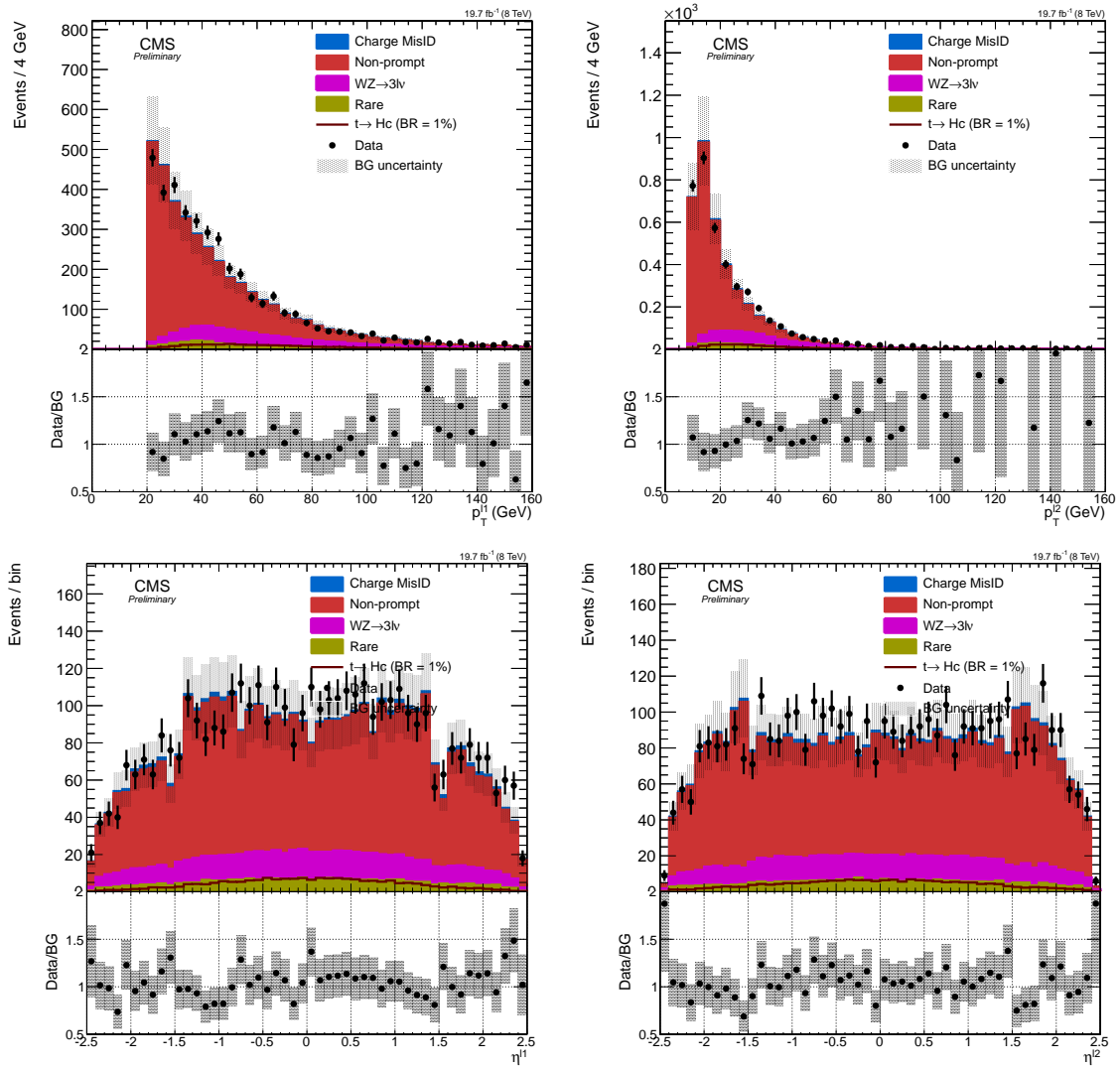


Figure A.8. Analysis variables for $e^\pm e^\pm$ after MET and HT cuts.

A.1.2. $e^\pm\mu^\pm$ Figure A.9. Kinematic distributions for $e^\pm\mu^\pm$ at preselection level.

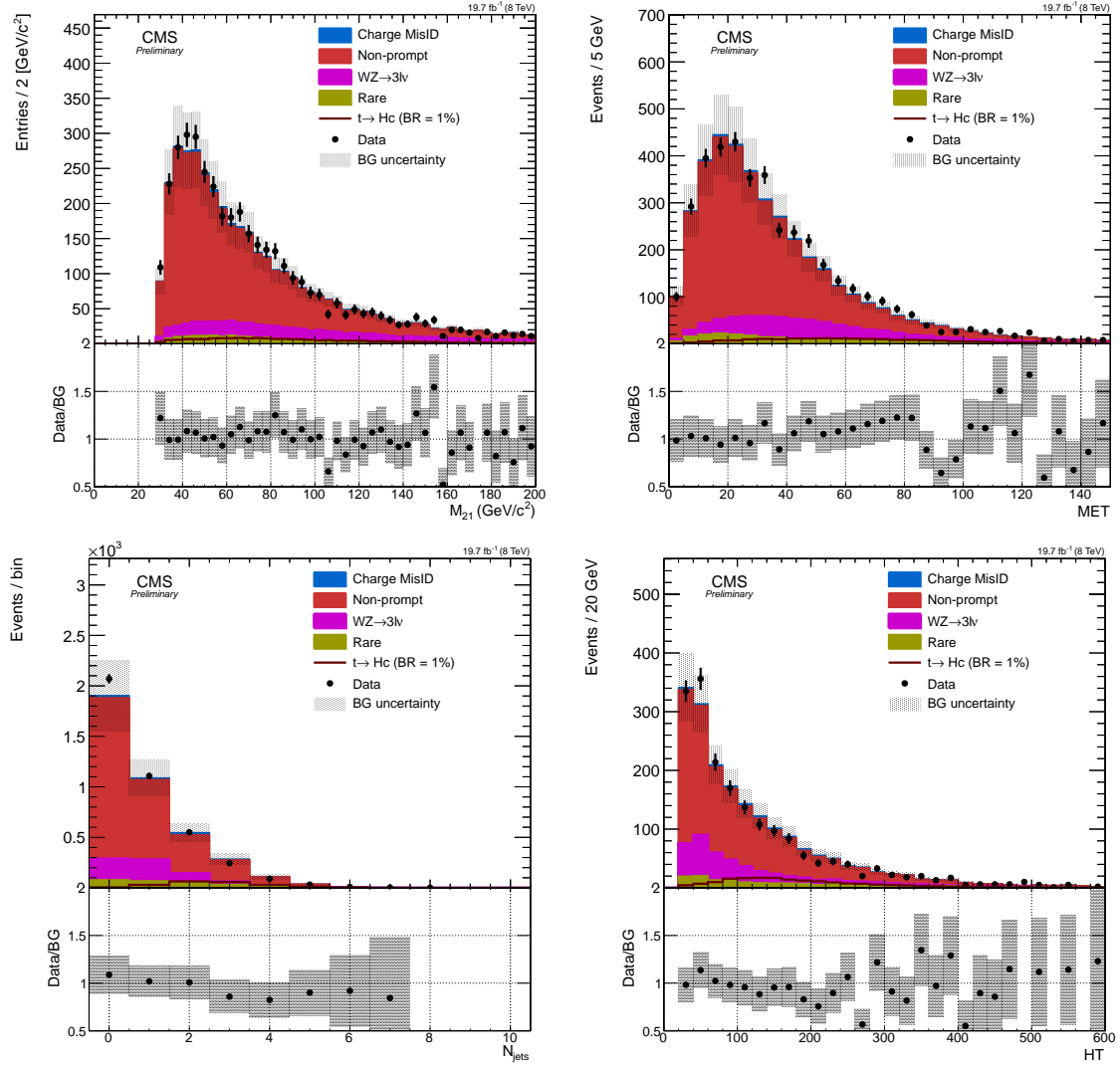


Figure A.10. Analysis variables for $e^\pm\mu^\pm$ at preselection level.

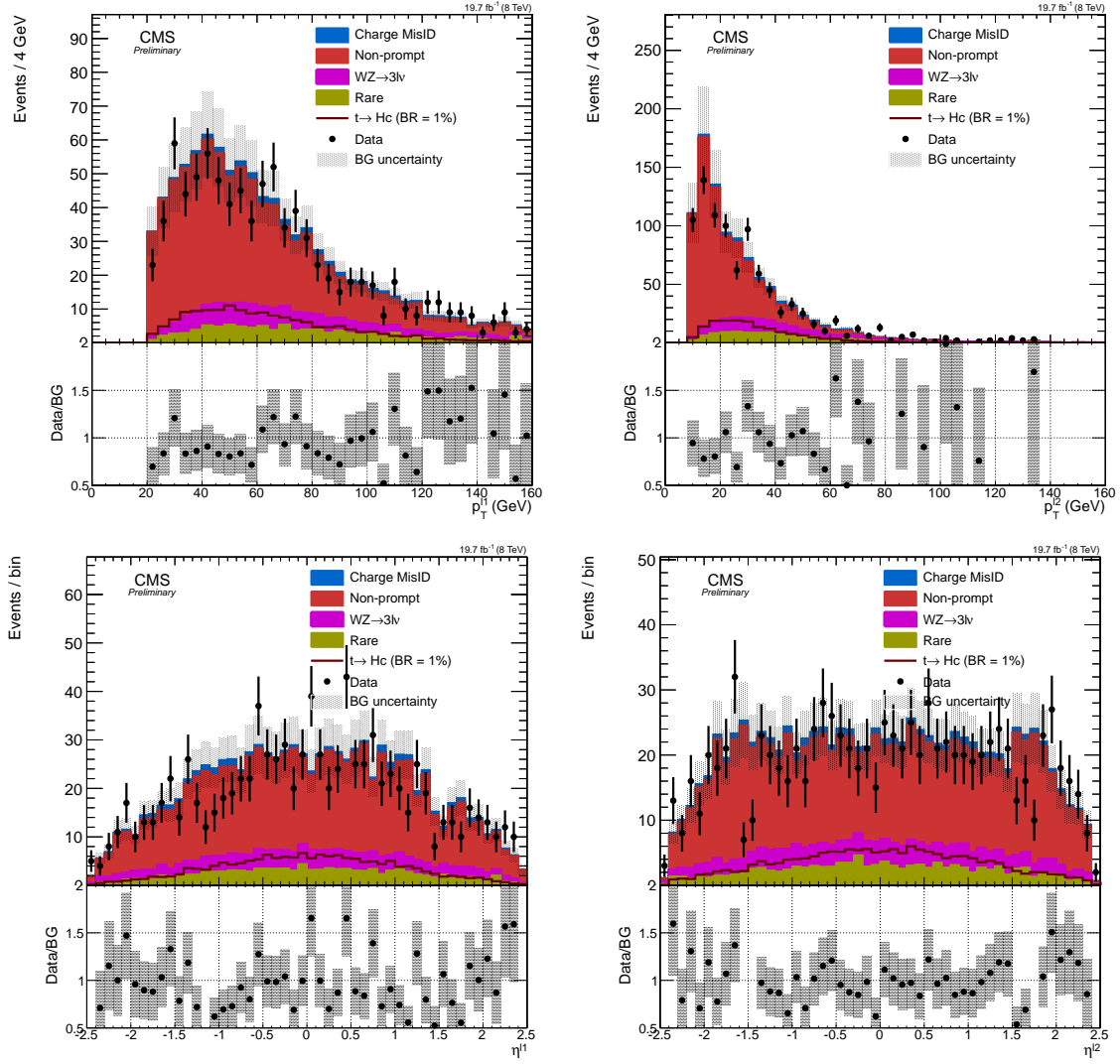


Figure A.11. Kinematic distributions for $e^\pm\mu^\pm$ after 2 jet requirement.

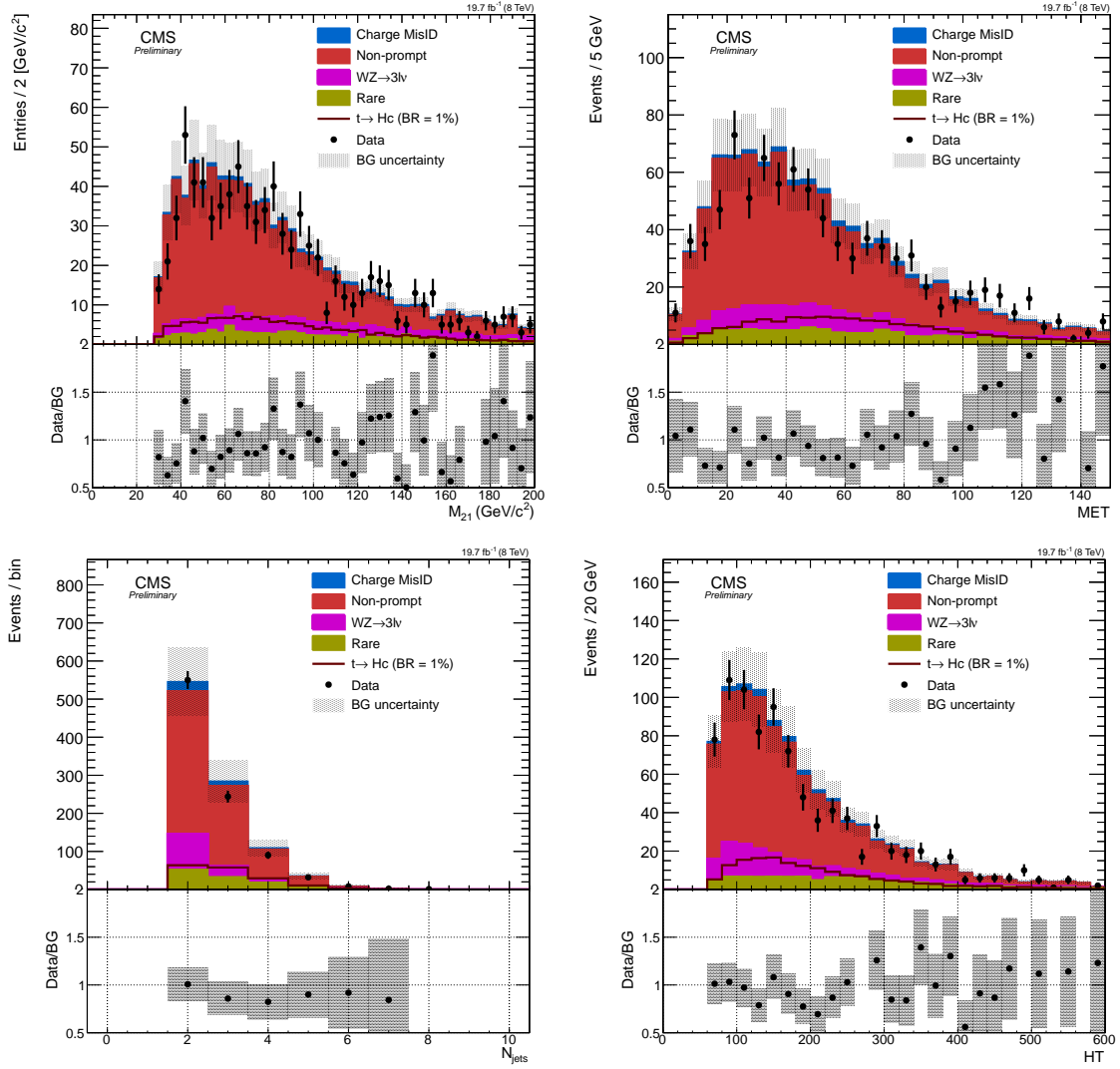


Figure A.12. Analysis variables for $e^\pm\mu^\pm$ after 2 jet requirement.

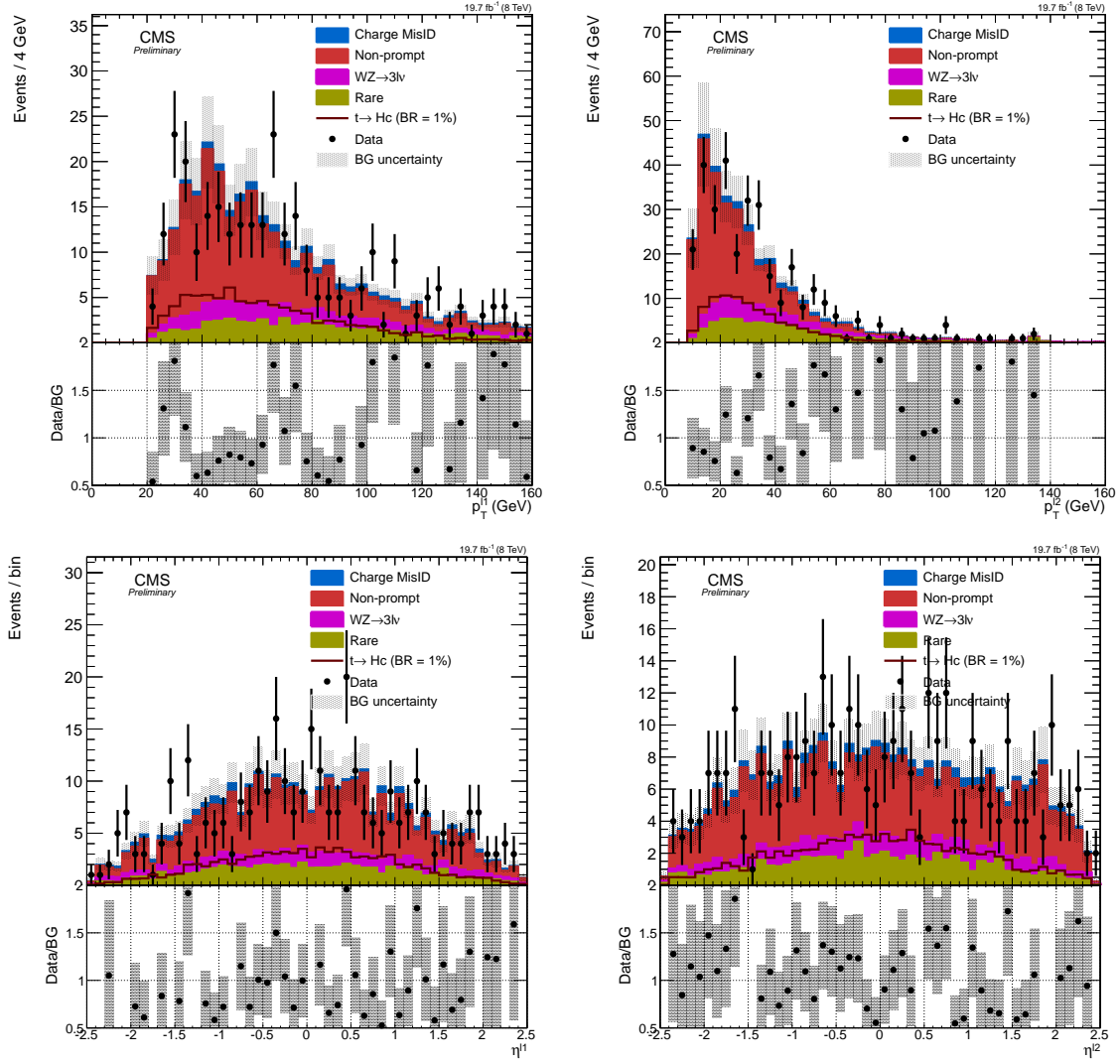


Figure A.13. Kinematic distributions for $e^\pm\mu^\pm$ after MET and HT cuts.

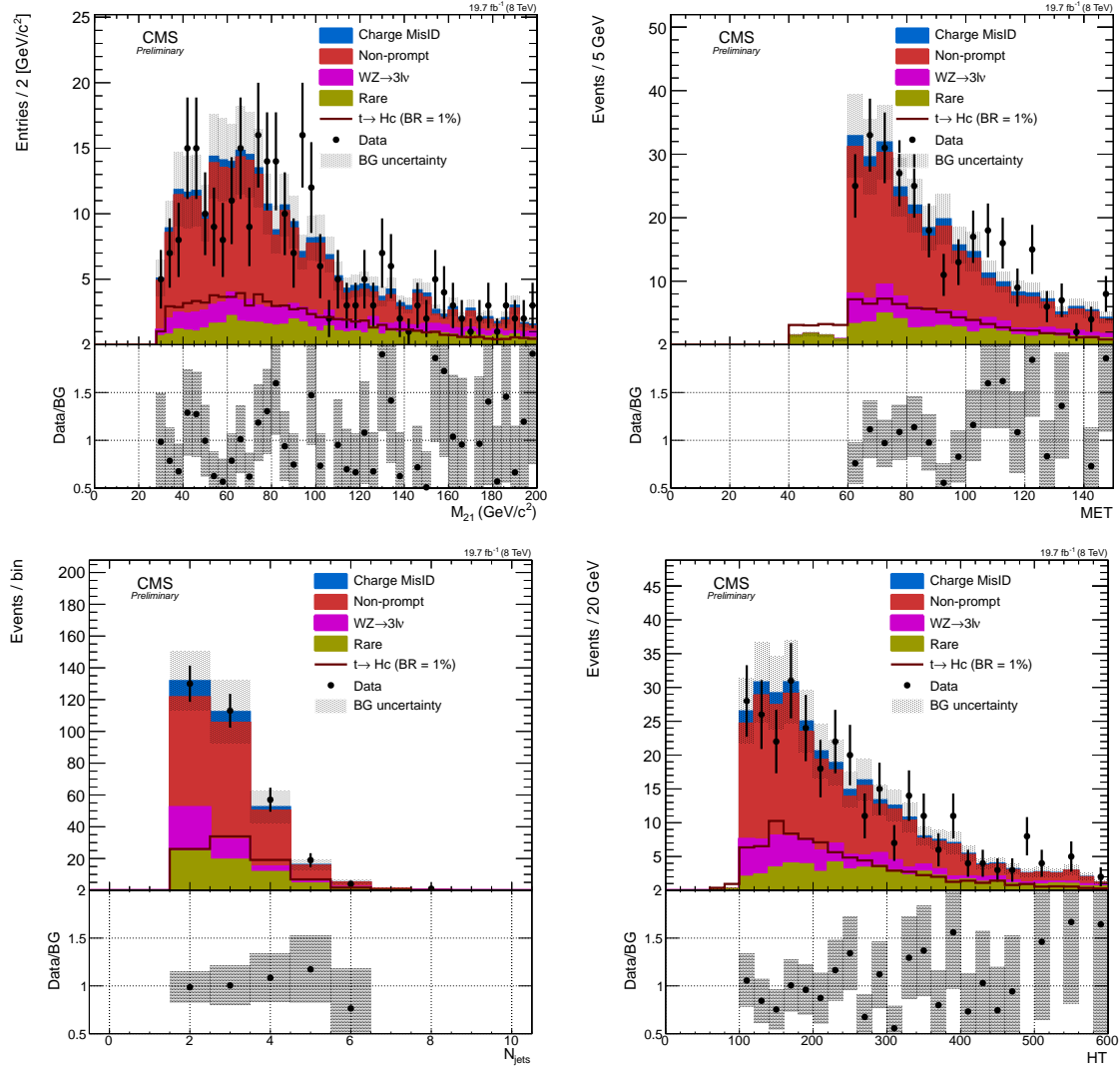


Figure A.14. Analysis variables for $e^\pm\mu^\pm$ after MET and HT cuts.

A.1.3. $\mu^\pm\mu^\pm$

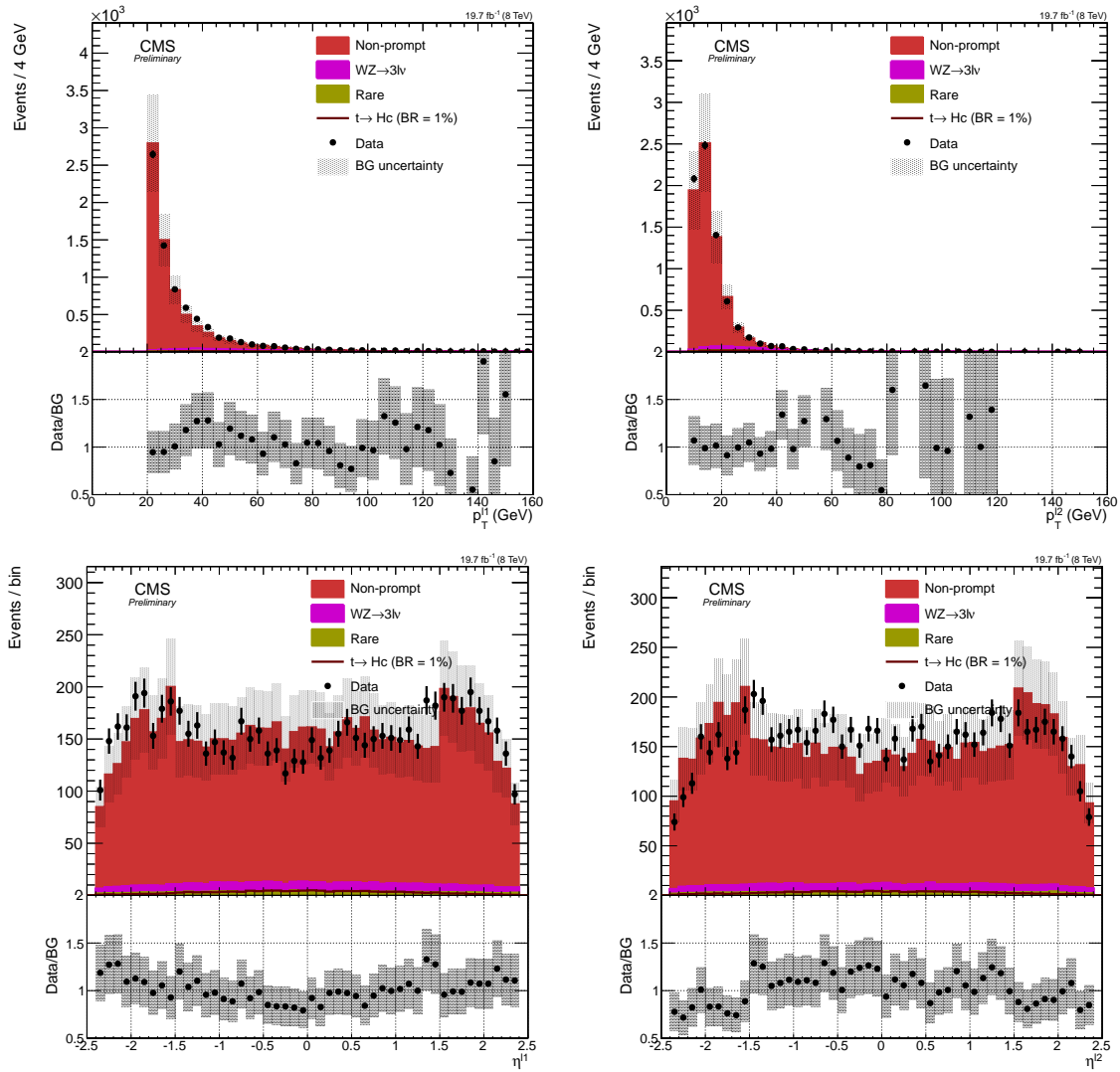


Figure A.15. Kinematic distributions for $\mu^\pm\mu^\pm$ at preselection level.

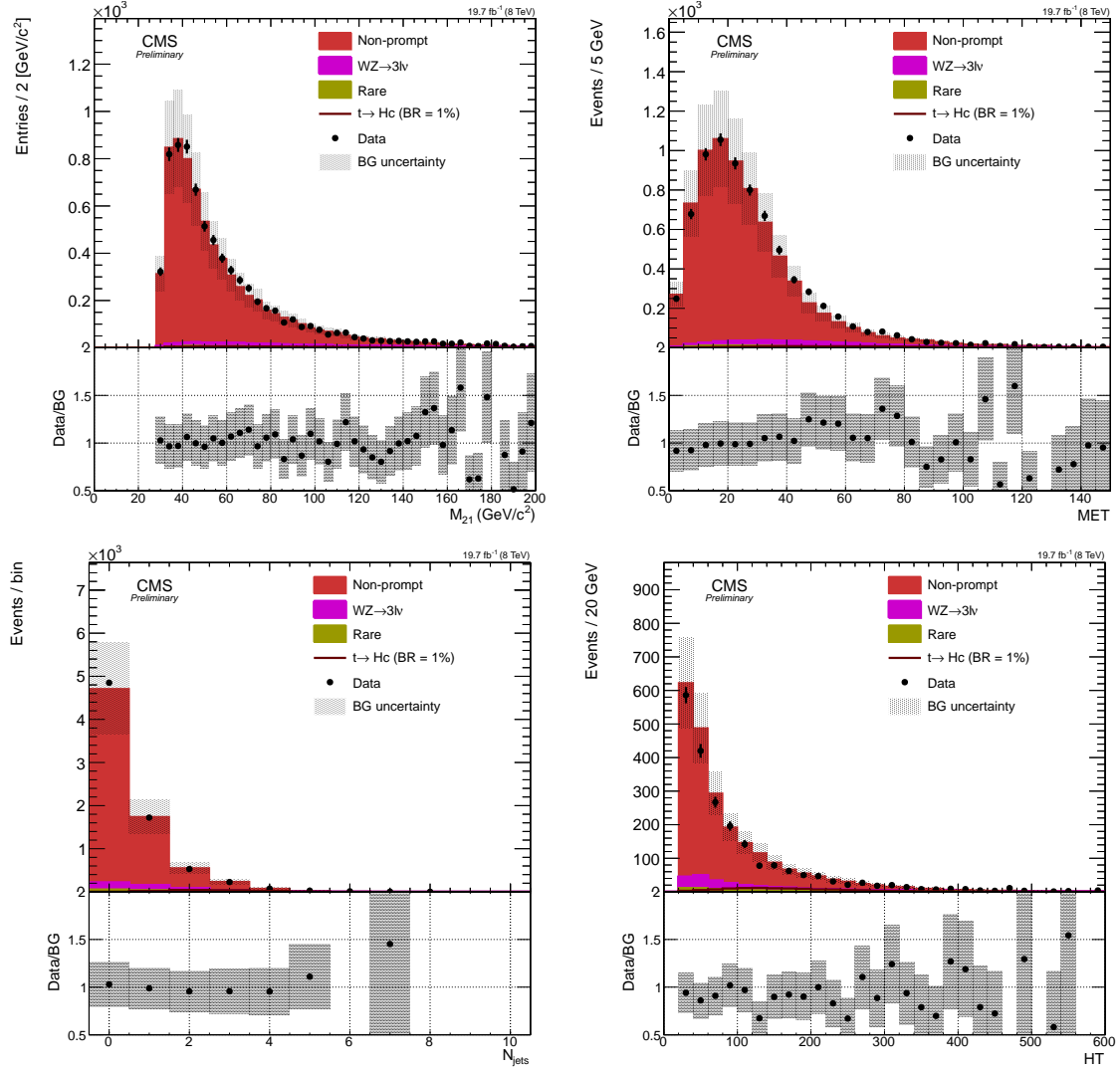


Figure A.16. Analysis variables for $\mu^{\pm}\mu^{\pm}$ at preselection level.

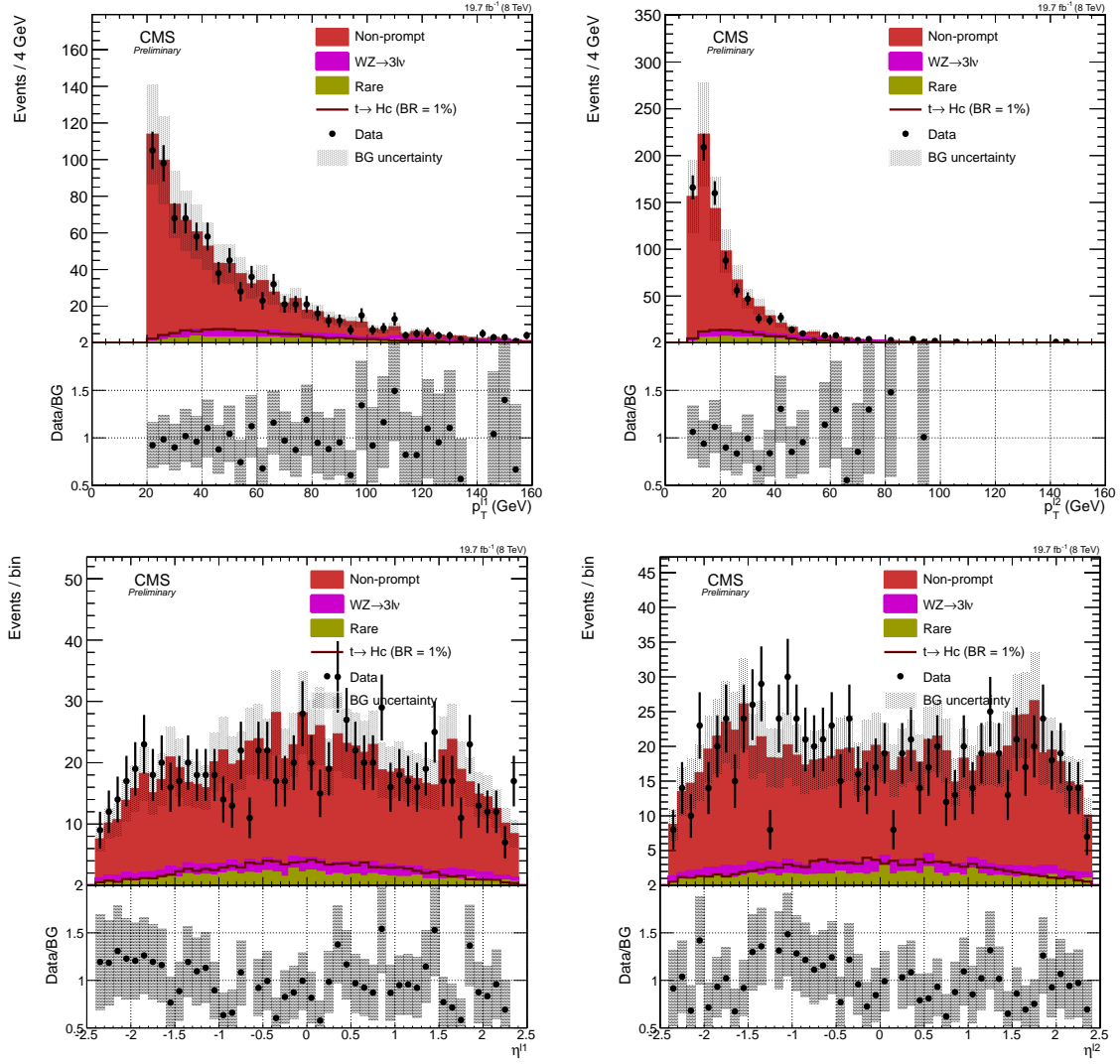


Figure A.17. Kinematic distributions for $\mu^\pm\mu^\pm$ after 2 jet requirement.

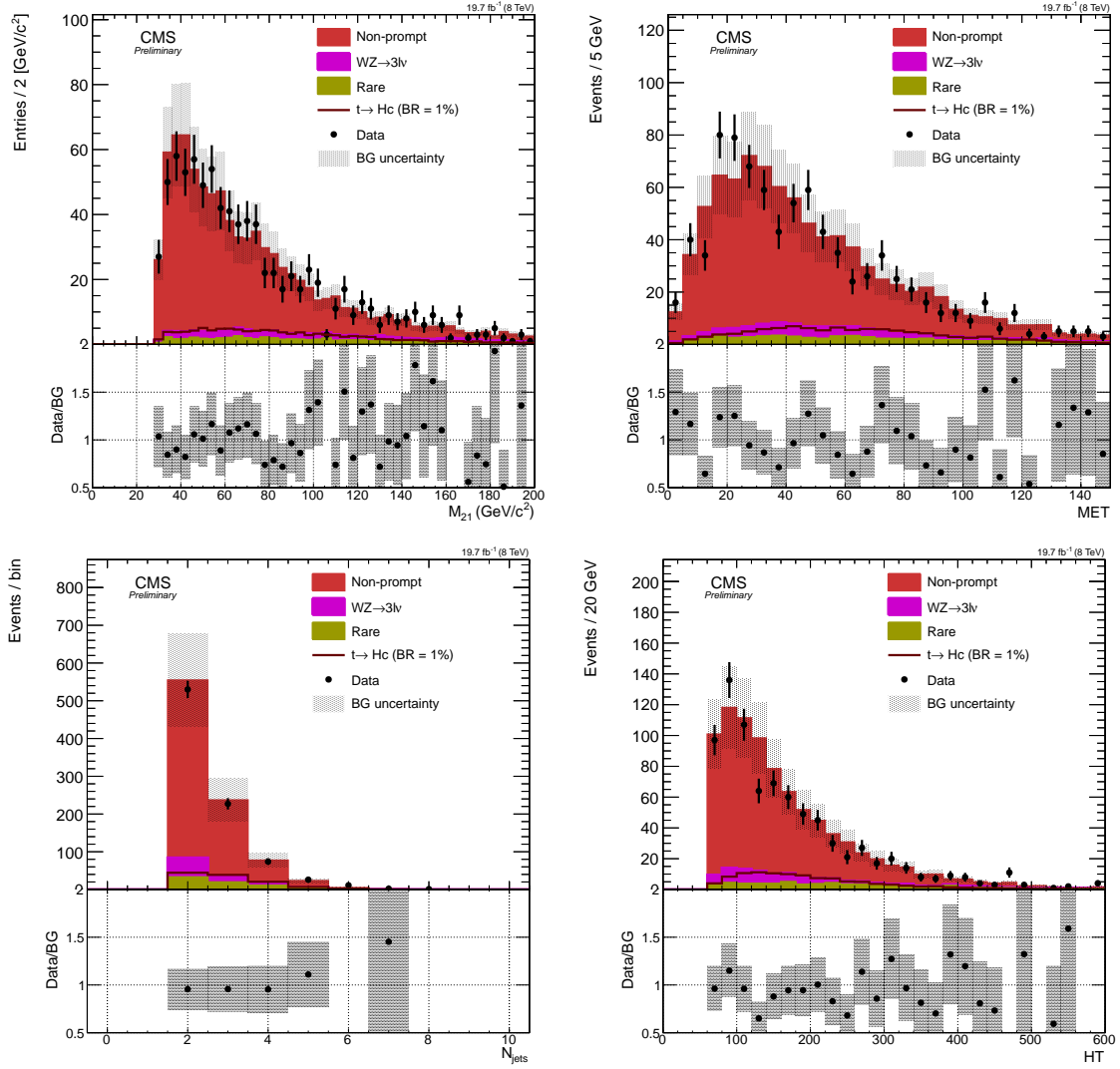


Figure A.18. Analysis variables for $\mu^{\pm}\mu^{\pm}$ after 2 jet requirement.

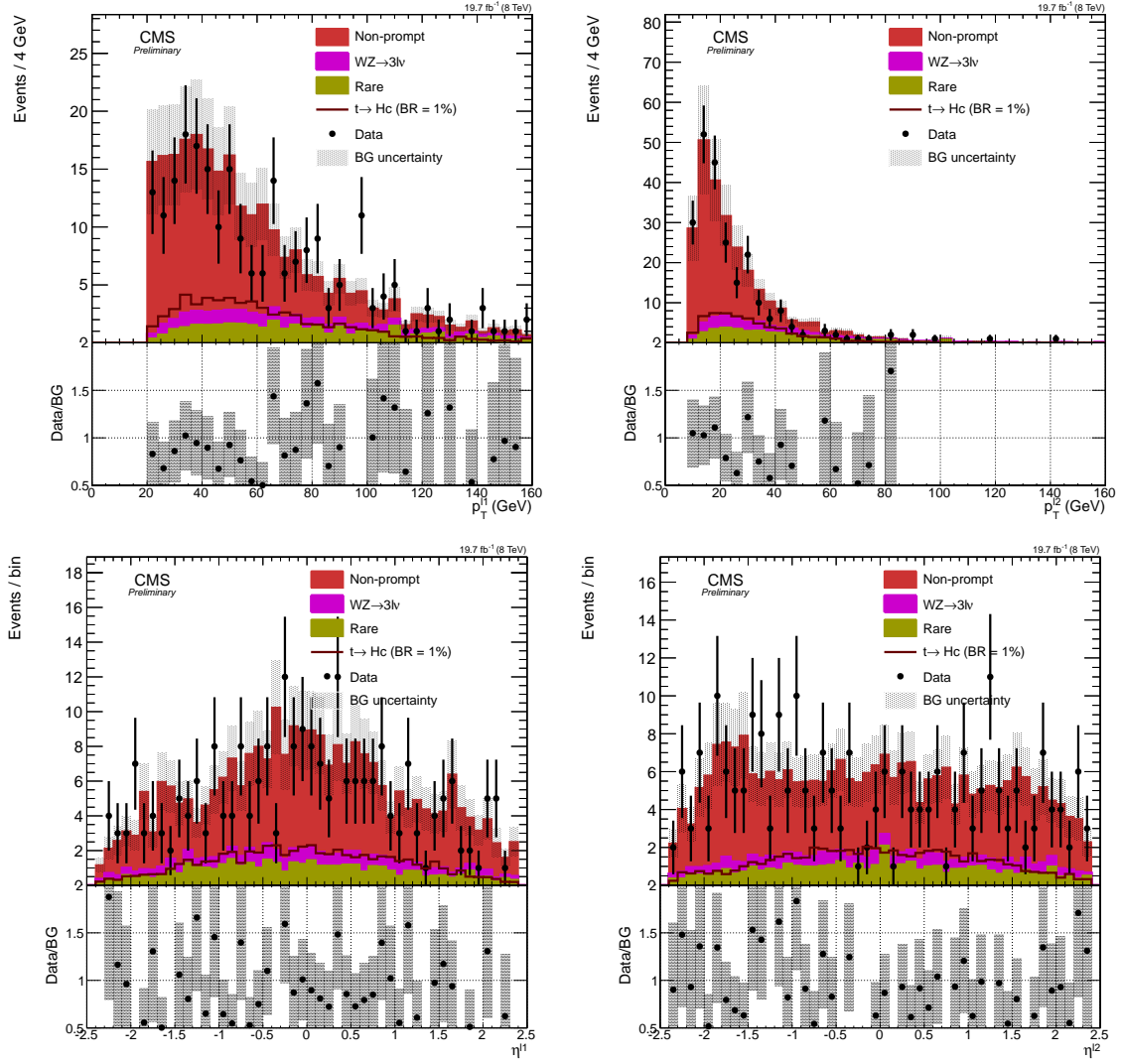


Figure A.19. Kinematic distributions for $\mu^{\pm}\mu^{\pm}$ after MET and HT cuts.

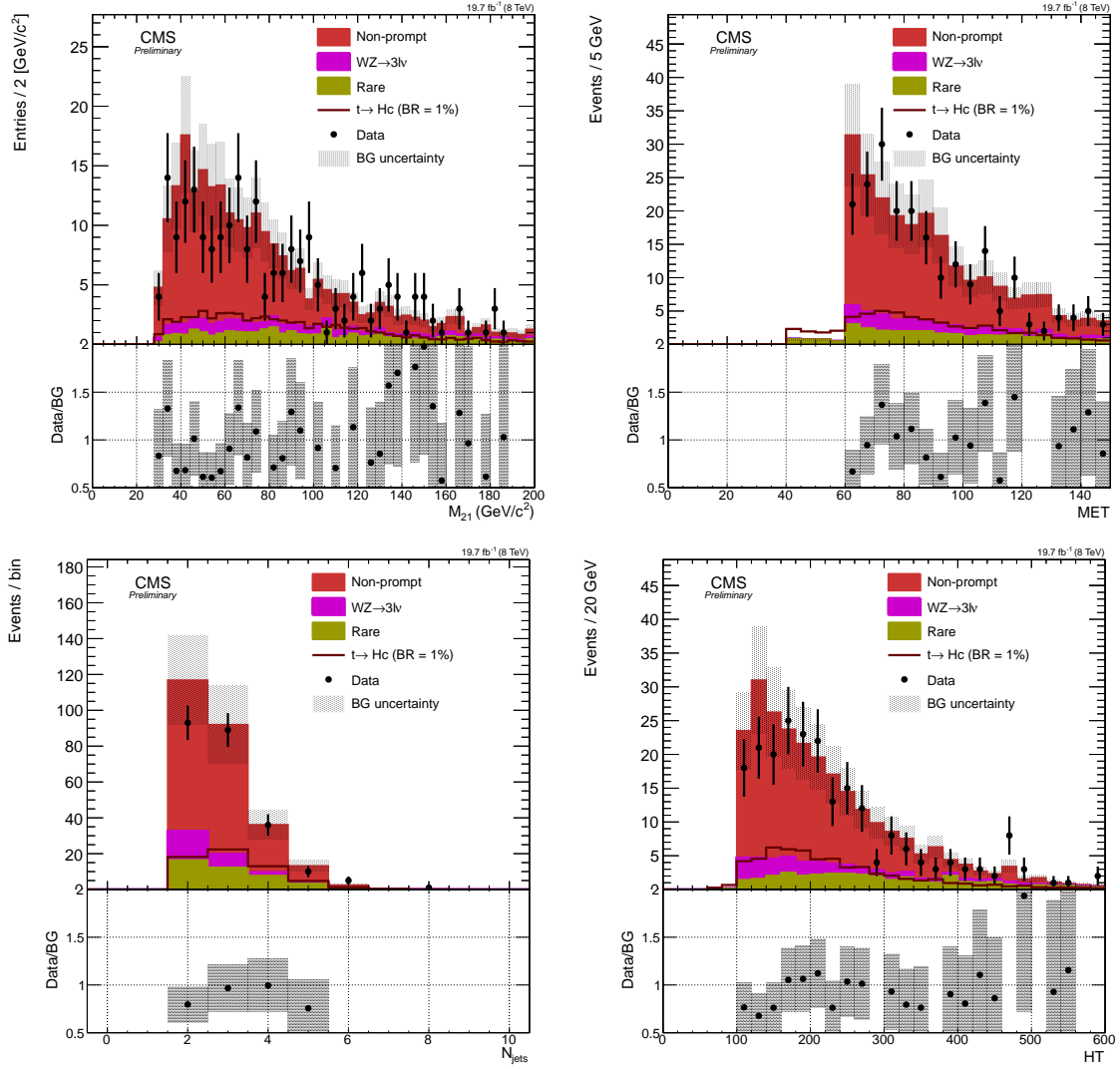
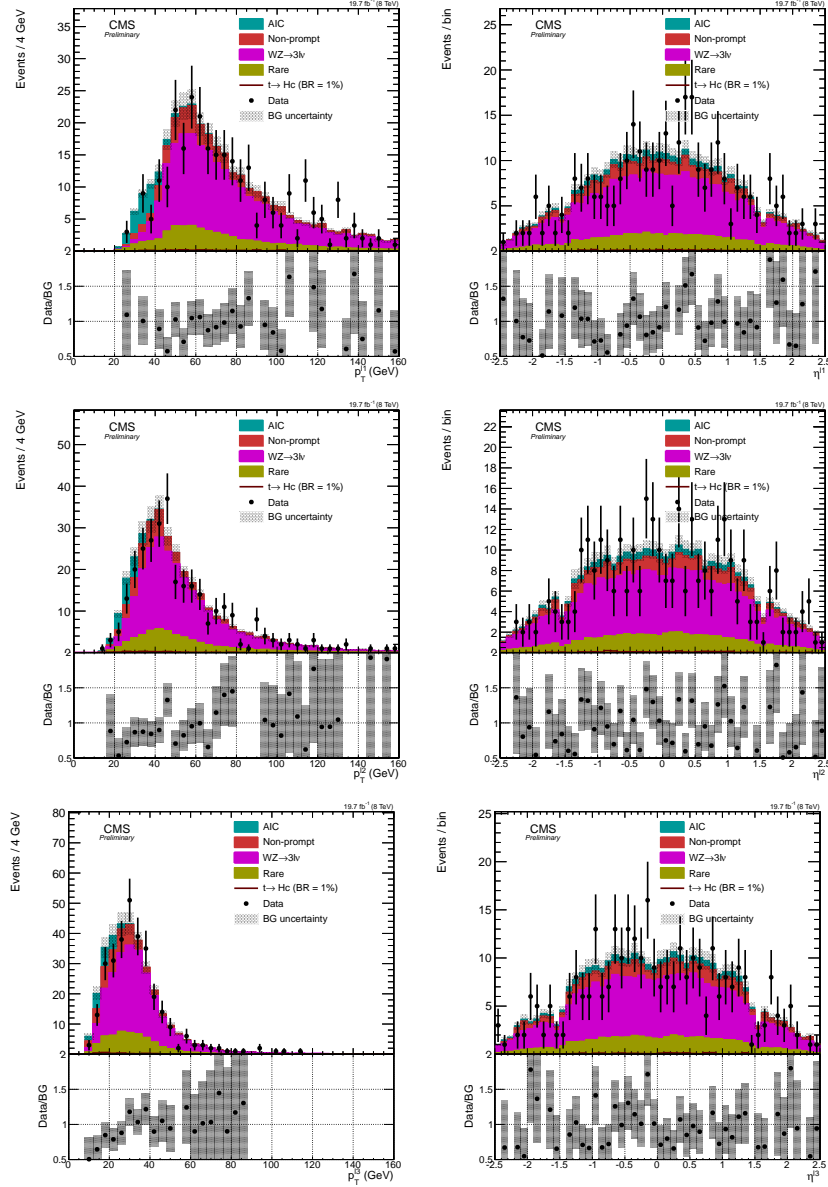


Figure A.20. Analysis variables for $\mu^{\pm}\mu^{\pm}$ after MET and HT cuts.

A.1.4. eee Figure A.21. Kinematic distributions for eee at preselection level.

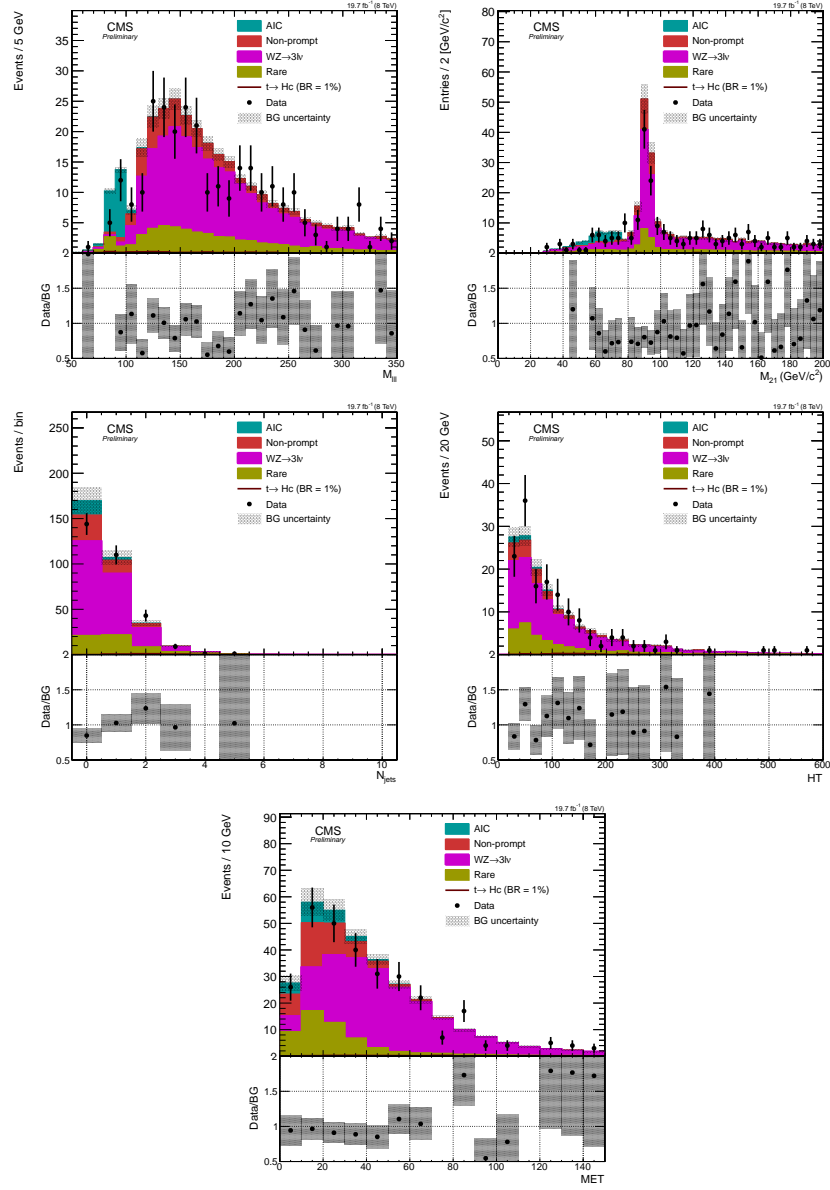
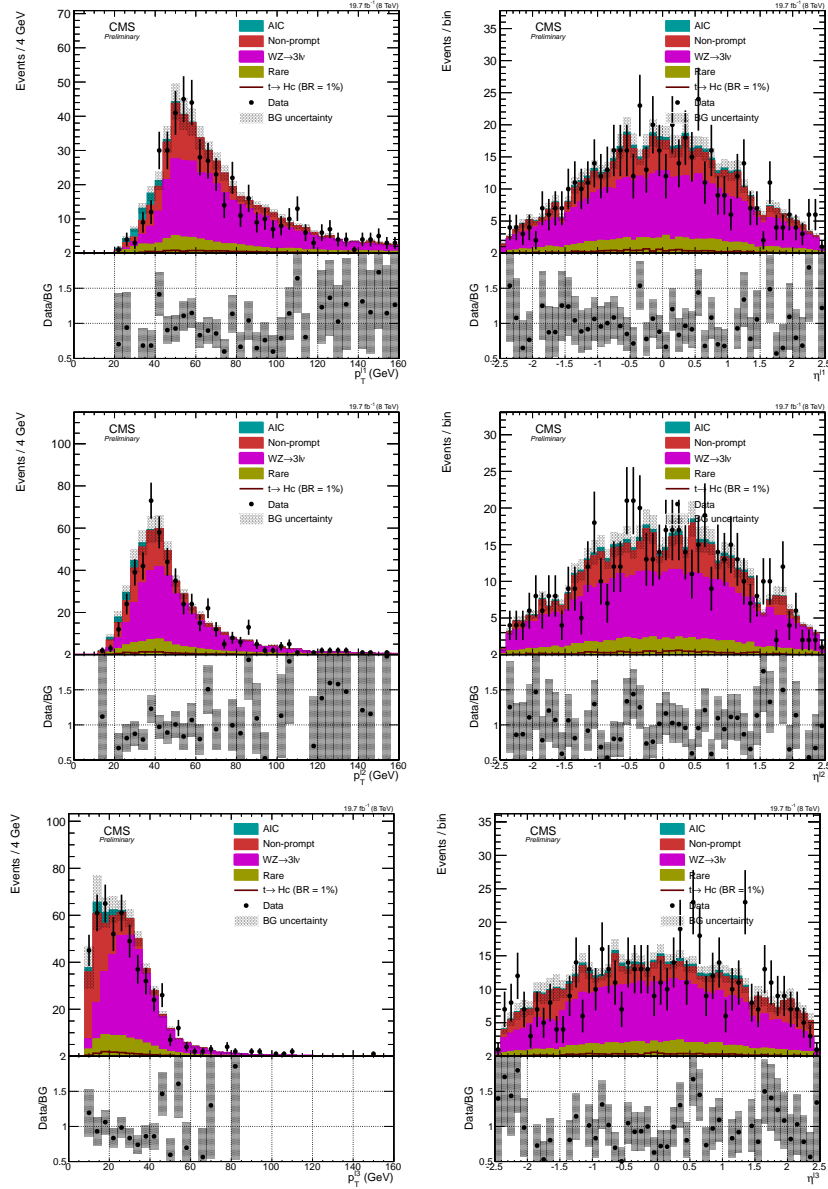
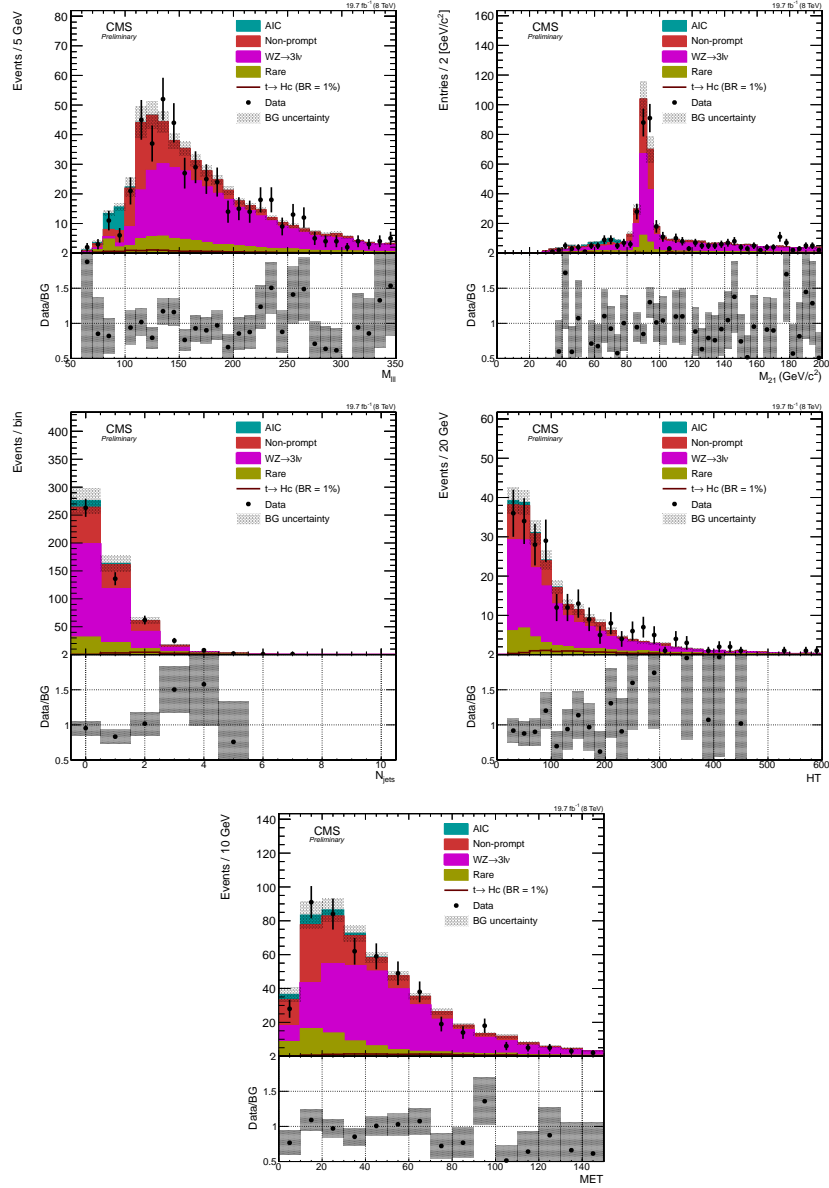
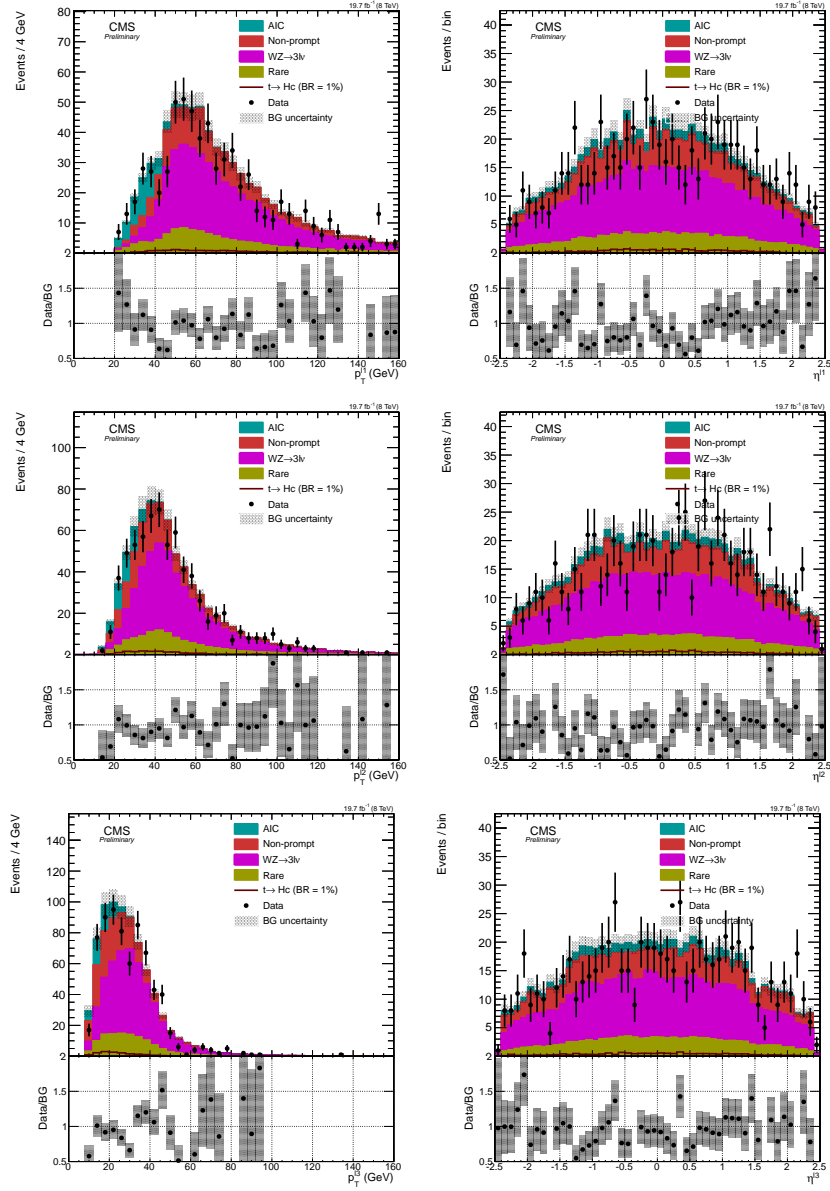


Figure A.22. Analysis variables for $\mu^{\pm}\mu^{\pm}$ at preselection level.

A.1.5. $ee\mu$ Figure A.23. Kinematic distributions for $\mu^{\pm}\mu^{\pm}$ at preselection level.

Figure A.24. Analysis variables for $\mu^\pm\mu^\pm$ at preselection level.

A.1.6. $e\mu\mu$ Figure A.25. Kinematic distributions for $\mu^{\pm}\mu^{\pm}$ at preselection level.

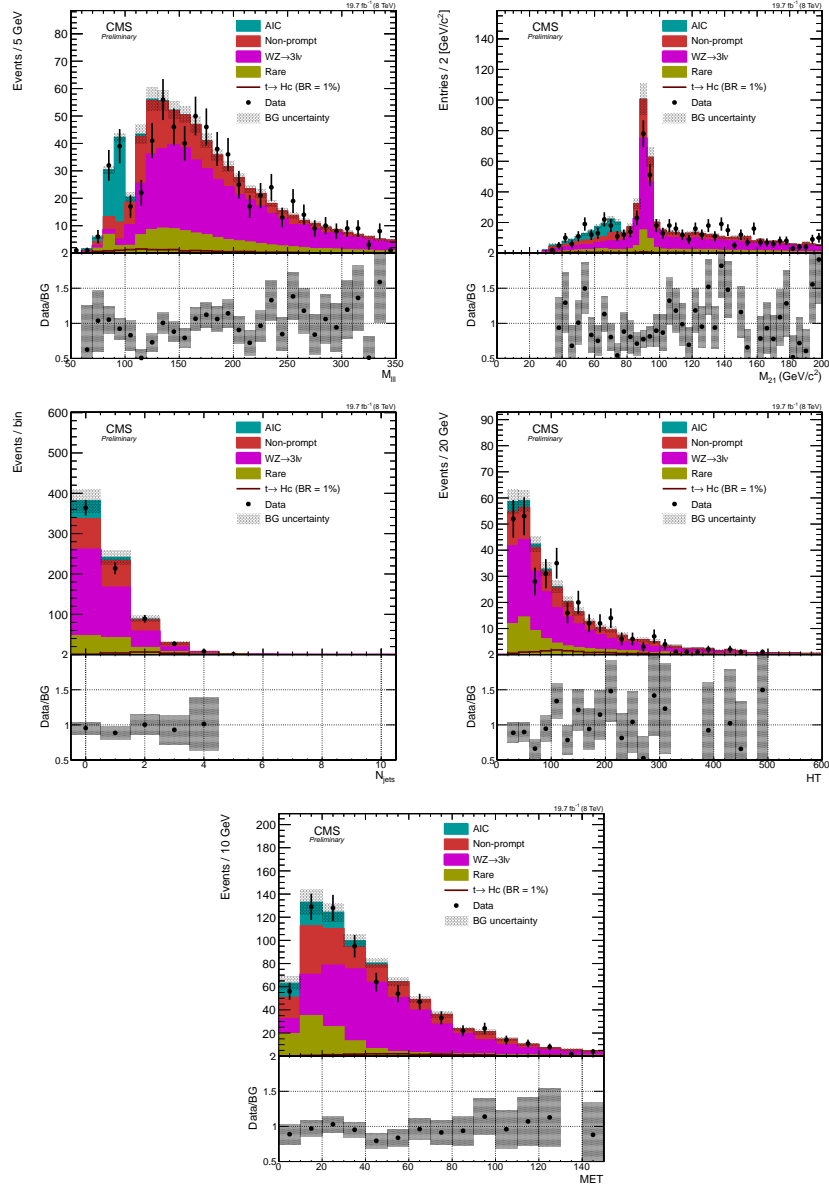
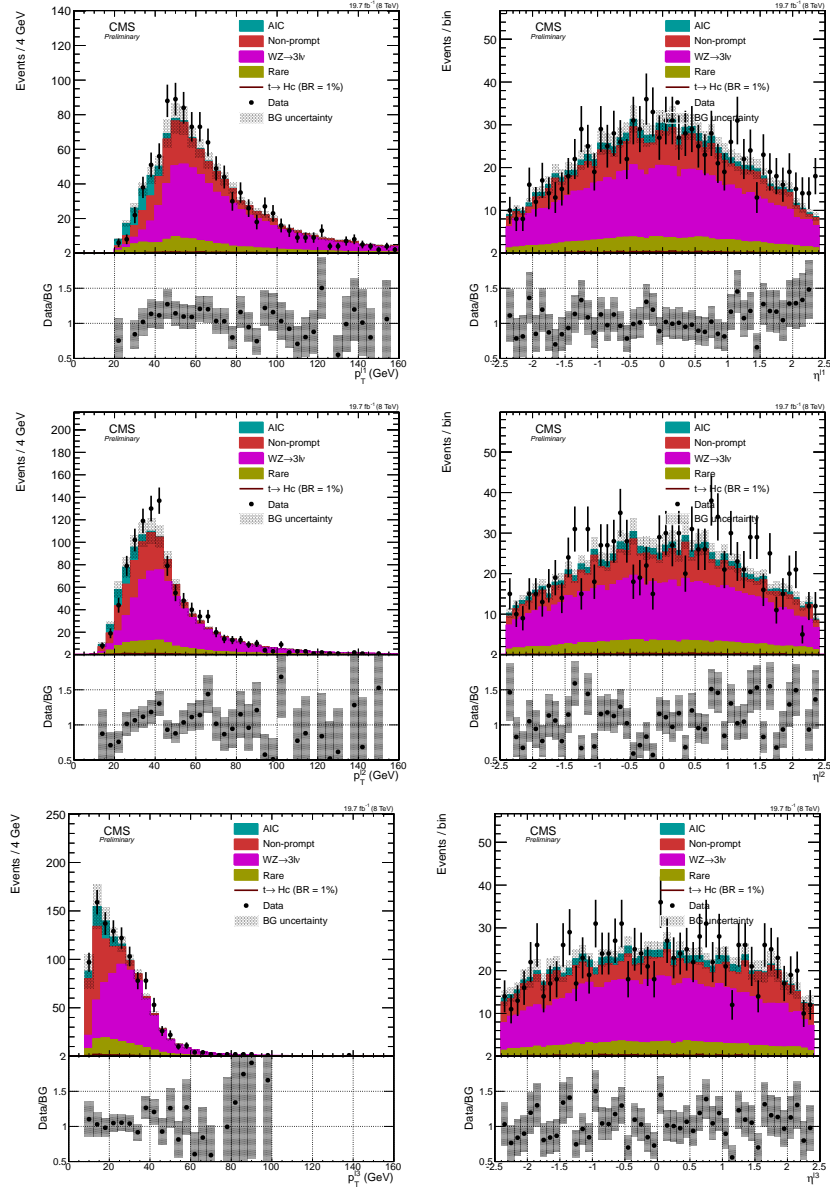


Figure A.26. Analysis variables for $\mu^{\pm}\mu^{\pm}$ at preselection level.

A.1.7. $\mu\mu\mu$ Figure A.27. Kinematic distributions for $\mu^\pm\mu^\pm$ at preselection level.

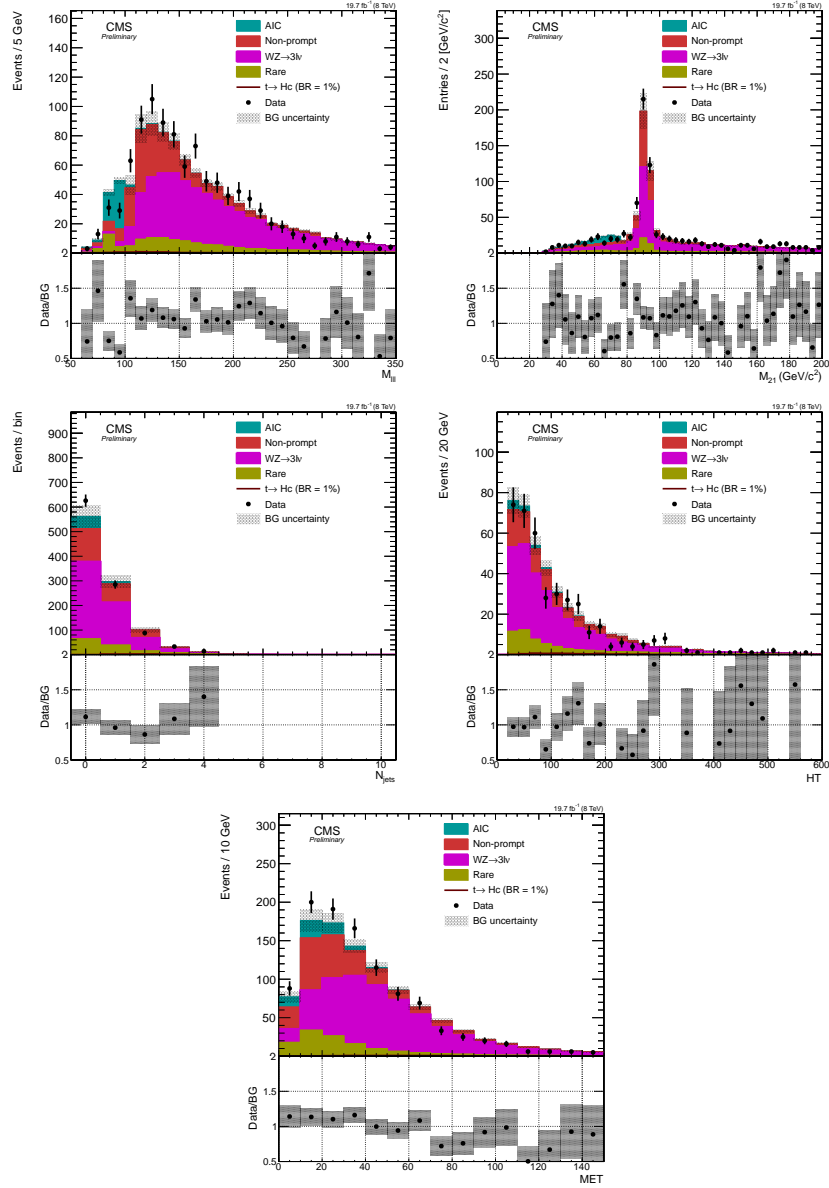


Figure A.28. Analysis variables for $\mu^\pm\mu^\pm$ at preselection level.

A.2. Multi-variate analysis

In order to take advantage of higher dimensional correlations between variables, a boosted decision tree (BDT) [66] is used to discriminate between the FCNH signal and background. This is carried out as a supplement to the cut and count analysis. Training is carried out after the Z veto and two or more jet requirement has been applied. The variables used as inputs are:

- MET;
- H_T ;
- b-jet multiplicity (passing medium CSV working point);
- M_T ;
- $M_{\ell\ell}$;

where M_T (shown in figure A.29) is defined as,

$$(A.1) \quad M_T = \sqrt{2 \times \text{MET} \times p_{t,\ell} (1 - \cos(\Delta\phi(\text{MET}, \ell)))}.$$

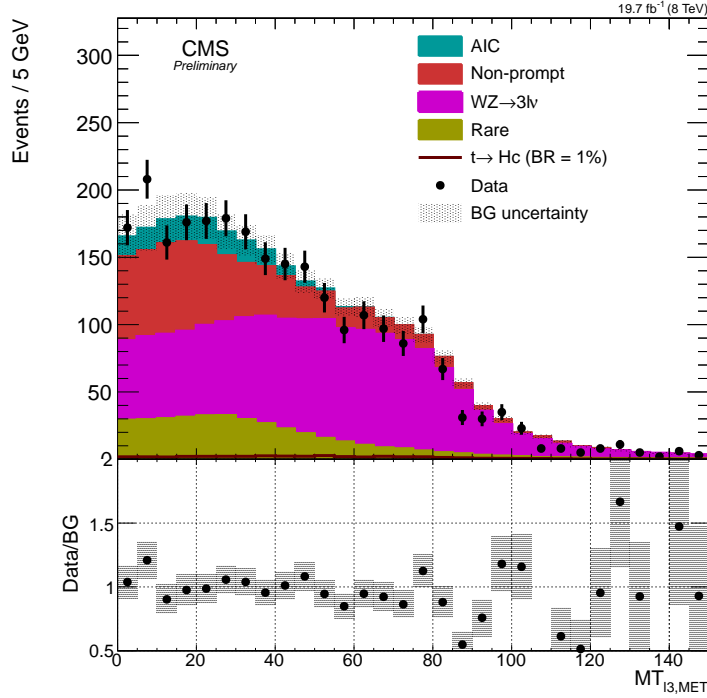


Figure A.29. M_T distribution at preselection level for three lepton events.

This is calculated only in the case that there are three leptons and two of them form OSSF pair. The remaining lepton is then used in the calculation to determine M_T . For the three lepton training, the $M_{\ell\ell}$ is formed from either the OSSF pair in the event, or if that does not exist, from the highest mass OS pair.

Examples of the input variable distribution for signal and background are shown in figure A.30. The correlation between the input variables for both the signal and background model are shown in figure A.31. These distribution allow for a determination of whether the included variables are strongly correlated and thus redundant. For the most part, the variables are uncorrelated.

The optimal cut is calculated based on the significance of the cut on the BDT output value taking into account the number of signal and background events before training the BDT. The cut efficiencies with optimal cut value (given by the maximum of the significance) is shown in figure A.32.

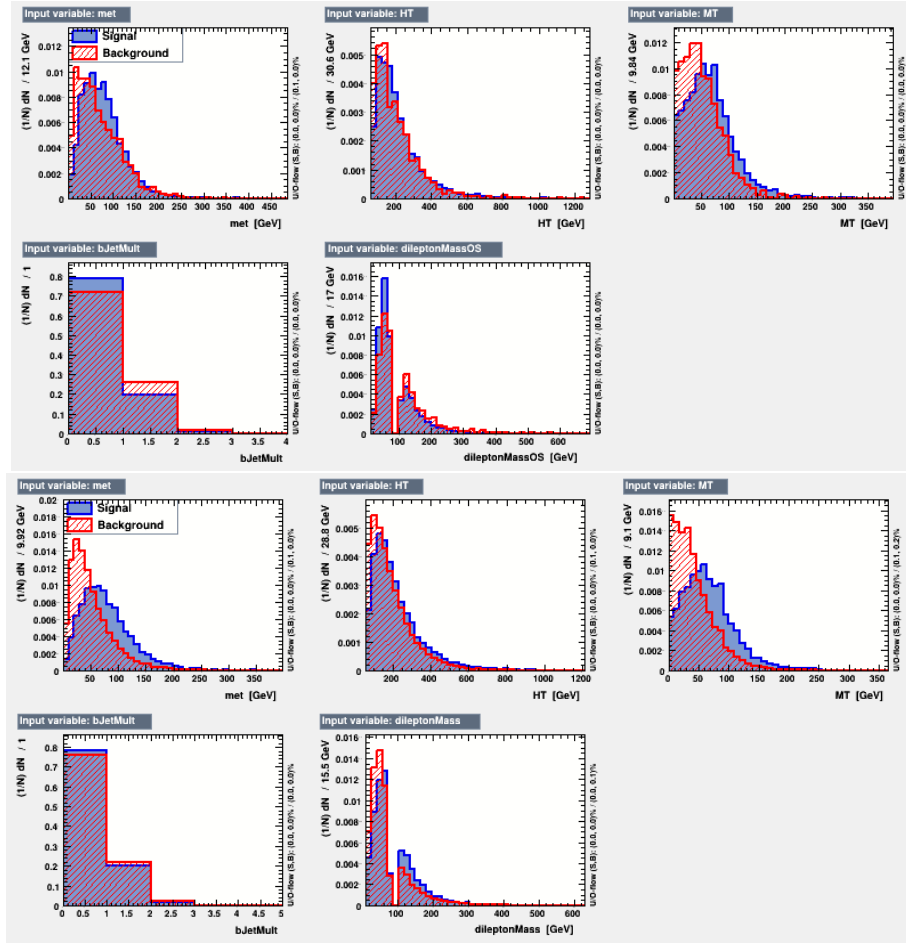


Figure A.30. Input variables for trilepton (top) and same-sign dilepton (bottom) BDT.

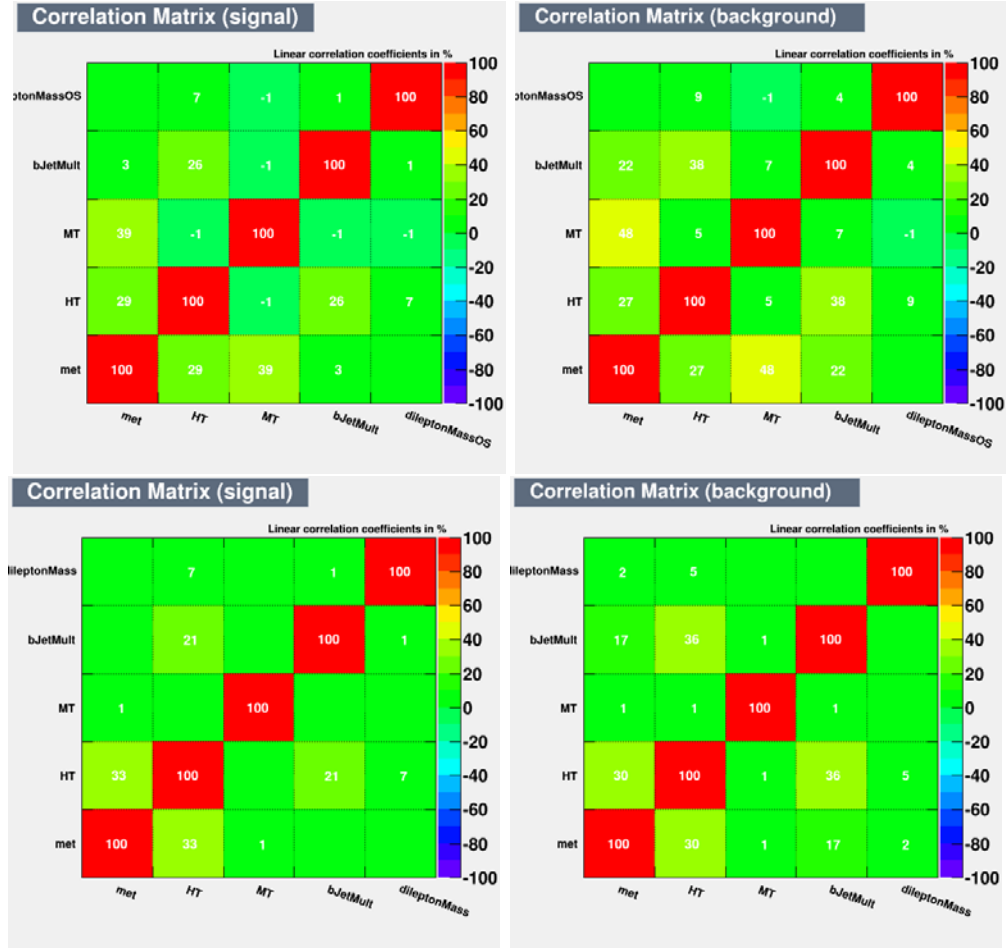


Figure A.31. Correlation matrix of input variables for trilepton (top) and same-sign dilepton (bottom) BDT.

	eee	$ee\mu$	$e\mu\mu$	$\mu\mu\mu$	ee	$e\mu$	$\mu\mu$
MT	0.2570	0.2426	.2475	.2455	.2290	.0825	.1193
M_{ll}	0.2250	0.2407	.2315	.2437	.1549	.0806	.0943
MET	0.2220	0.2270	.2295	.2320	.0444	.0224	.0758
HT	0.2070	0.2015	.2048	.2094	.0366	.0135	.0174
b-jet Mult	0.0890	0.8820	.0867	.0694	.0159	.0056	.0051

Table A.8. Ranking of input variables for BDT by flavor category.

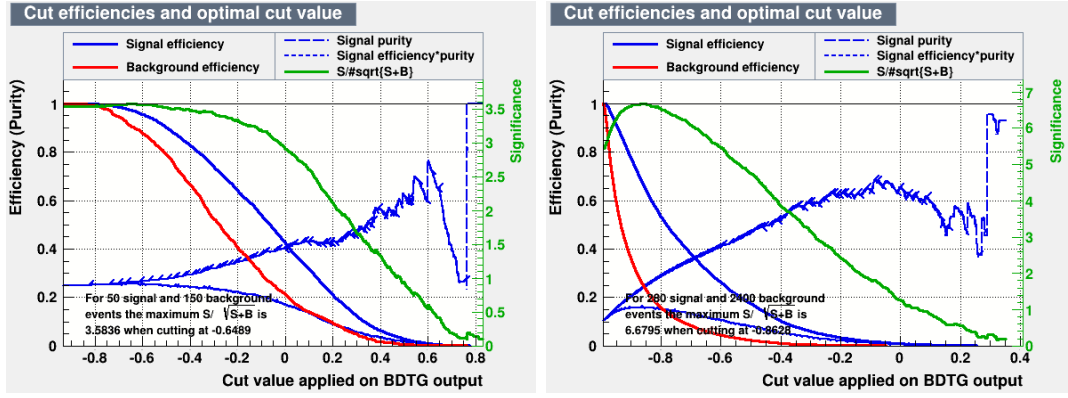


Figure A.32. Significance and efficiencies for singal and background by cut of the trilepton (left) and same-sign dilepton (right) BDT discriminator output.

APPENDIX B

Measurement of luminosity and normalized beam-induced background using CMS Fast Beam Conditions Monitor

B.1. Introduction

The CMS experiment [6] must function in an exceptionally high radiation environment with an expected maximum instantaneous luminosity in excess of $10^{34} \text{ cm}^{-2}\text{s}^{-1}$, and beam intensities on the order of 10^{14} protons. In the interest of protecting the inner detector – in particular, the inner silicon pixel tracker – it is important to characterize the long-term dose, and respond to rapid beam losses. To meet these needs, several beam and radiation detectors have been placed along the beam-pipe near the CMS detector.

Of particular interest is the Fast Beam Conditions Monitor (BCM1F). This detector is highly responsive to rapid variations in the beam conditions with a time resolution on the order of several nanoseconds. In addition to providing a vital role in beam monitoring, the detector is also capable of providing online, bunch-by-bunch instantaneous luminosity which can be used to provide real-time feedback to the LHC.

B.2. Beam Conditions Monitoring at CMS

The Fast Beam Conditions Monitor, BCM1F [67], is a particle detector based on single-crystal diamonds grown using chemical vapour (CVD) deposition techniques.

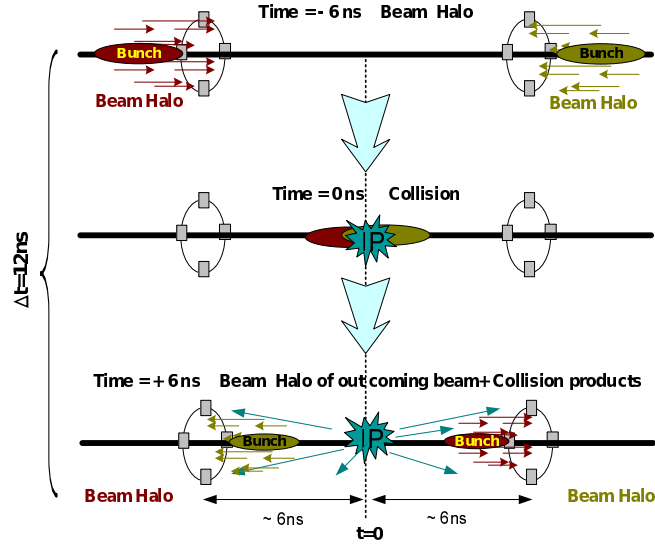


Figure B.1. Schematic of arrival time for various beam products.

Some important properties of single-crystal diamonds (sCVD) are its radiation hardness due to its large displacement energy and low leakage current with almost no temperature dependence removing the need for active cooling. These qualities make it an attractive material to be used in a particle detector, especially in areas of high radiation and locations where space is limited. This is particularly relevant in the densely packed CMS forward region, or in the CMS inner region where access to services like cooling is inconvenient. In addition, diamond sensors are characterised by very fast response allowing temporal measurements with nanosecond resolution.

The BCM1F detector consists of 8 sCVD sensors, installed in two planes located at 1.8 m on either end of the interaction point (IP) with each module at transverse distance of 5 cm from the nominal beam spot. Each sensor has a surface area of $5 \times 5 \text{ mm}^2$ and a thickness 0.5 mm^3 .

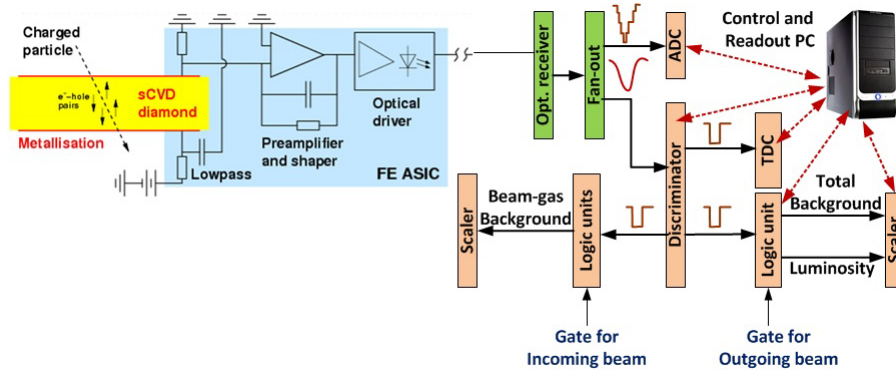


Figure B.2. A schematic of the BCM1F readout chain

The distance between the sensors and the IP is optimal for the separation of incoming and outgoing particles and corresponds to a time-of-flight of ~ 6 ns for relativistic particles as can be seen in fig. B.1. Hence, by dividing the signals into different time windows the rates of beam halo particles can be separated from those of collision products.

The details of the BCM1F readout chain are described in detail in [67]. In summary, an analog optical signal is sent from a radiation hard front-end ASIC to our back-end electronics (shown in fig. B.2) where rate counting and data acquisition for offline analysis of pulse characteristics is done.

B.3. BCM1F Signal Characterization

Several studies were undertaken over the course of data-gathering at CMS to characterize the behaviour of BCM1F. The goal of these tests is to characterize the detector's sensitivity to a variety of beam products and stability over a range of different operating conditions. Given that the BCM1F sends an analog signal to the backend, pulse characteristics (i.e., pulse amplitudes and time to return to threshold) can be assessed offline by using an ADC VME module with nanosecond resolution. It is important that this

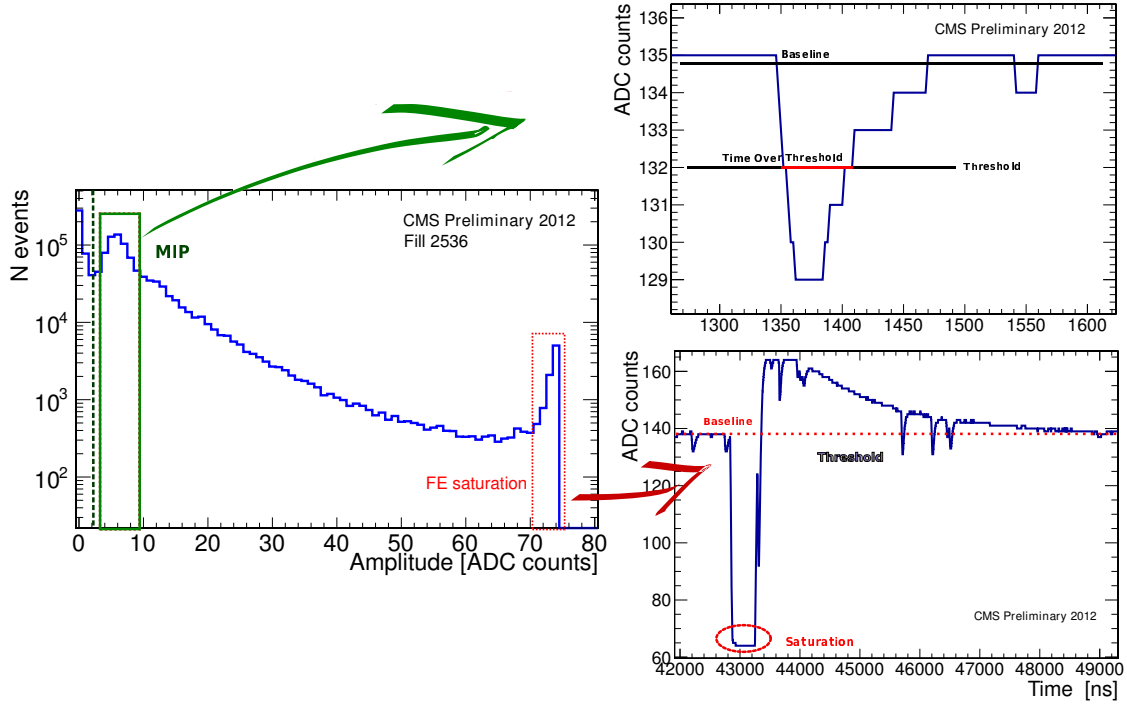


Figure B.3. Pulse characterization from data collected with back-end ADC.

is understood since the method for discriminating, and therefore, counting rates, uses a fixed-threshold discriminator. This means that if there occurs a shift in the signal baseline we are not going to see signals since they will no longer show sufficient voltage to pass the pre-set threshold. One way to gauge the significance of this effect is to measure the time that a given pulse spends over the threshold.

An example the characterization is shown in fig. B.3. One important feature to note is the occasional high amplitude signal that results in saturation of the front-end electronics. The consequence of this is a decrease in the hit counting efficiency due to an increase the time required to recover to baseline.

Another important quantity to determine is the single bunch hit probability. This is done by counting the rate of hits in the lead bunch in an orbit. This bunch is preceded by

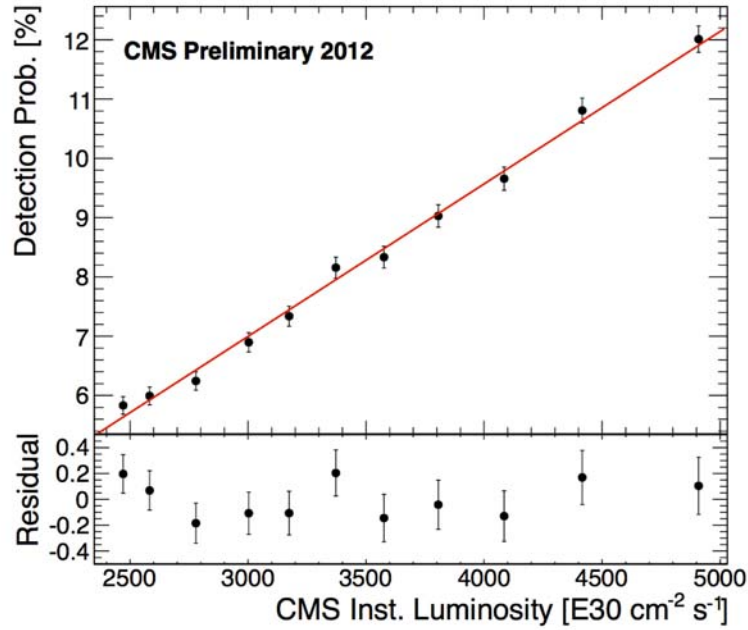


Figure B.4. Single bunch hit probabilities as a function of the instantaneous luminosity measured by HF. Hit probability is measured for the leading bunch in each orbit.

the abort gap, and is therefore much less likely to be affected by inefficiencies caused by signals from preceding bunches. A fair amount of variation between each of the 8 sensors is observed. Given that a range of single diamond rates need be considered in order to cover the range of observed luminosities, it is important to accurately characterize how the relative differences in hit probabilities depends on the particle flux. For the most part, it is observed that they are stable over the range of observed luminosities and demonstrate a linear dependence (fig. B.4).

B.4. Beam-induced background measurement

So-called beam-gas interactions occur when protons from the beam interact with residual gas in the beam pipe. These interactions are dominated by small angle, inelastic

collisions with the resulting particles moving parallel to the beam pipe. Typically the flux of these type of interactions is on the order of 10^{-5} less than the flux from collision products. In the case that there is degradation of the vacuum in the beam pipe, this flux can increase significantly causing excessive firing of channels in the pixel detector resulting in an increase in the overall dead-time.

Because the flux relative to collision products is typically so low, beam-gas products are separated from collision products by only looking at non-colliding bunch crossings that precede colliding bunches. Additionally, only non-colliding bunches that are sufficiently separated from the previous bunch train are considered due to the high flux from albedo following colliding bunches crossing.

An example of the resulting measurement is shown in fig. B.5. The normalized beam gas flux measurement is implemented online independent of the CMS central data acquisition, by using the following steps

- In real-time measure the bunch pattern of beam 1 and beam 2 with the BPTX.
- Select non-colliding bunches by generating an 8 ns wide gate from the BPTX signal, co-incident with the time arrival of incoming non-colliding bunches in BCM1F.
- Open a VETO gate, 900 ns long after a colliding bunch, thus permitting only non-colliding bunch intervals, well separated from collisions (reduce albedo products) to be selected.
- Use 12 ns time of flight between the -Z and +Z BCM1F detector planes to gate separately on incoming and outgoing beam products.

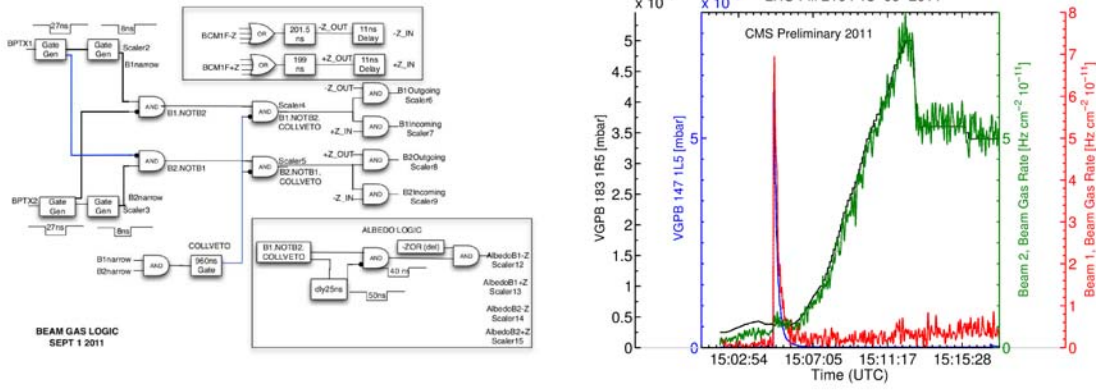


Figure B.5. Schematic of BCM1F back-end gating to select on beam-gas products (*left*). Comparison of beam-gas measurement and vacuum quality using pressure gauges (*right*).

- Measure a pedestal rate in 40 ns window before non-colliding bunch train, to estimate the non-beam gas component of the measured rate due to activation from collision products.
- Measure the bunch charge for each selected non-colliding bunch, online using the Fast Beam Current Transformer (FBCT), so as to obtain a correctly normalized beam-gas flux measurement, per 1011 particles.

The NIM logic implemented for the beam gas measurement is shown schematically in fig. B.5. The count rates in the relevant gates are integrated with a scaler module and then published every second. The normalized beam-gas flux is calculated, and made available to both CMS and the LHC every second.

The performance of the beam-gas measurement can be seen for LHC fill 2104 in fig. B.5. For additional details on this measurement, see [68].

B.5. Luminosity Determination and Calibration

The method of determining the luminosity delivered to CMS relies upon a relation between measurable quantities (rates in the BCM1F detector, for instance) and the actual rate of interactions due to collisions inside the detector. In the ideal circumstance with n_b colliding bunches circulating in the accelerator the following relation can be used,

$$(B.1) \quad L = \frac{n_b f_b \mu}{\sigma_{inel}}$$

where f_b is the frequency of the orbit, $\sigma_{inelastic}$ is the inelastic scattering cross-section, and μ is the average number of interactions per bunch crossing,

$$(B.2) \quad \mu = \frac{\langle N \rangle}{n_b}.$$

This, of course, assumes that the average number of interactions per orbit ($\langle N \rangle$) is perfectly measured. In reality, a quantity μ_{obs} is measured and is related to μ by multiplication by some detection efficiency, ε , such that,

$$(B.3) \quad \mu_{obs} = \varepsilon \mu,$$

$$(B.4) \quad \sigma_{obs} = \varepsilon \sigma_{inelastic}.$$

The ε term accounts for all detector specific effects, which may depend on the luminosity. Even at constant per bunch luminosity, ε is a function of the number of bunches in LHC

(arises from recovery time of front end: with more bunches in the machine, hits from a given bunch are more likely to be screened by a preceding bunch and are more likely to screen following bunches), the bunch intensity and the pattern of bunches within an orbit. Therefore, the relation between luminosity and the measured quantities is written,

$$(B.5) \quad L = \frac{n_b f_b \mu_{obs}}{\sigma_{obs}}.$$

The following sections describe our methodology for determining μ_{obs} and σ_{obs} .

B.5.1. Zero Counting

The number of interactions per bunch crossing for a given set of beam parameters follows a Poisson distribution. The probability of a given number of interactions, n , is given by,

$$(B.6) \quad p(n) = \frac{\mu^n e^{-\mu}}{n!}.$$

This relation allows to determine the average number of interactions when the probability that there is no interaction, $p(0)$, is measured,

$$(B.7) \quad \mu = -\ln[p(0)],$$

$$(B.8) \quad = -\ln[1 - p(> 0)].$$

For the case of the BCM1F, $p(0)$ is defined as the probability that there are no hits in the eight diamond sensors.

B.5.2. Van der Meer Scan Calibration

In order to convert the measured μ_{obs} value to a luminosity, we need to determine an absolute luminosity calibration. This, in essence, consists of determining the σ_{obs} value. The approach that we have adopted for producing the calibration was proposed by Van der Meer [69] and relies on making a simultaneous measurement of μ_{obs} and horizontal and vertical beam separation. The following expression defines the luminosity purely in terms of beam parameters,

$$(B.9) \quad L = f_b N_1 N_2 \int \rho_1(x, y) \rho_2(x, y) dx dy$$

where $N_{1/2}$ are the particles in the bunches of the beams, and $\rho_{1/2}(x, y)$ the density of the beams as a function of the transverse distance from their respective centers. Assuming that there is no correlation between the beam density in the x and y directions, the above equation can be re-parameterized in terms of the effective beam width,

$$(B.10) \quad \Sigma_x = \left[2\pi \int \rho_1(x) \rho_2(x) dx \right]^{-1},$$

$$(B.11) \quad \Sigma_y = \left[2\pi \int \rho_1(y) \rho_2(y) dy \right]^{-1},$$

yielding,

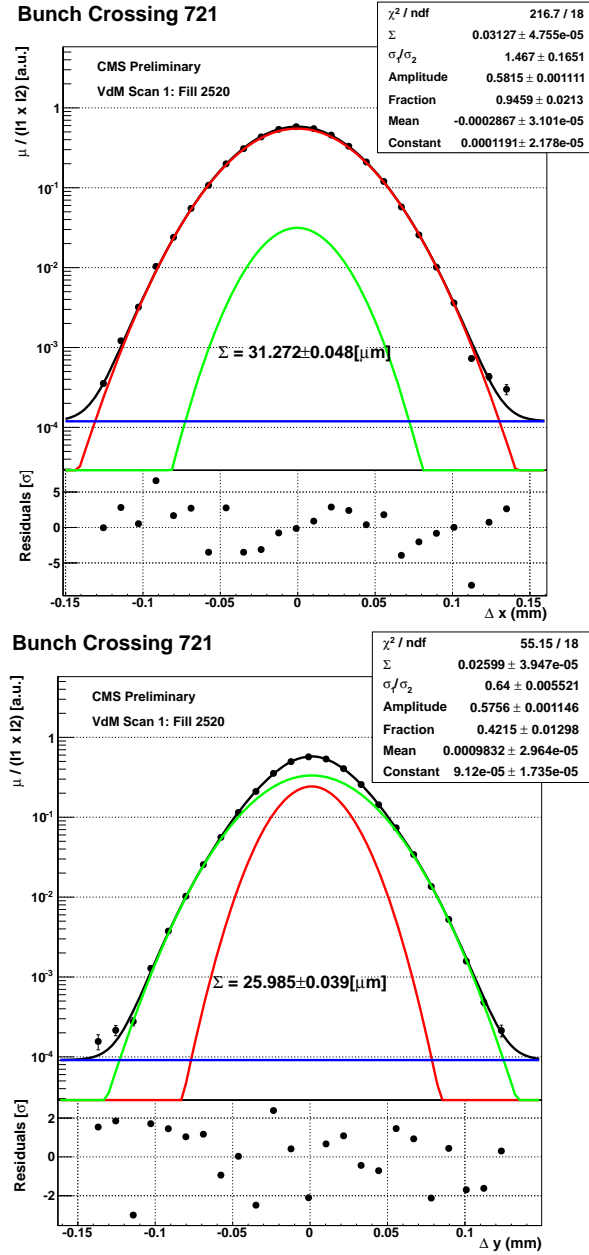


Figure B.6. Data gathered during the April 2012 VdM scan. The data is fit with a double gaussian plus constant where the single gaussian components are shown in red and green, the constant in blue, and the combined result is in black.

$$(B.12) \quad L = \frac{f_b N_1 N_2}{2\pi \Sigma_x \Sigma_y}.$$

From this expression and eq. B.5, a relation which allows for the determination of the effective cross-section can be derived,

$$(B.13) \quad \sigma_{vis} = 2\pi \Sigma_x \Sigma_y \frac{\mu_{vis,max}}{N_1 N_2}.$$

The effective widths are determined by separating the beams independently in the x and y directions. Therefore, for each calibration two separate scans need to be carried out. As the beams are separated, the rate at the detector is measured giving us a relation between the value of μ and the beam separation. This is then fit to extract the relevant quantities. For the April 2012 scan, it was determined that a double Gaussian distribution gives a suitably good fit. The form of the fit functions is,

$$(B.14) \quad \mu_{x,vis} = \mu_{x,vis}^{peak} \left(\frac{f_1 \Sigma_x}{\sigma_1} e^{\frac{(x-X_0)^2}{2\sigma_1^2}} + \left(1 - \frac{f_1 \Sigma_x}{\sigma_1} \right) e^{\frac{(x-X_0)^2}{2\Sigma_x^2} (1-f_1)^2 \left(1 - \frac{f_1 \Sigma_x}{\sigma_1} \right)^2} \right).$$

The BCM1F participated in the April 2012 VdM scan that consisted of 3 separate scans of the beam in the x and y directions. An example of the extraction of the calibration constant is shown in B.6. In figure B.7, the results of the first scan for each bunch crossing is shown with a comparison to the other luminometers from CMS. A systematically smaller width than HF is observed, but this difference is at the level of 1%. Though the cause of

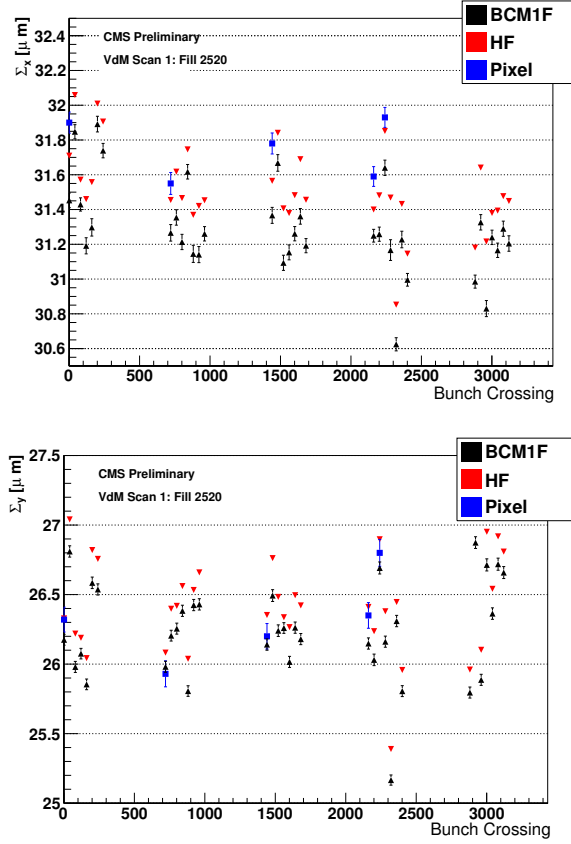


Figure B.7. Comparison between CMS luminometers of width of beam overlap for x and y scans.

this is not completely understood, a possible explanation lies in the higher sensitivity of HF to lower rates.

B.6. Simulation

To model and eventually correct for observed inefficiencies in the bunch-by-bunch counting rates a MC simulation was developed. This simulation takes into account pulse characteristics extracted from the ADC-based analysis. Input parameters for the simulation are:

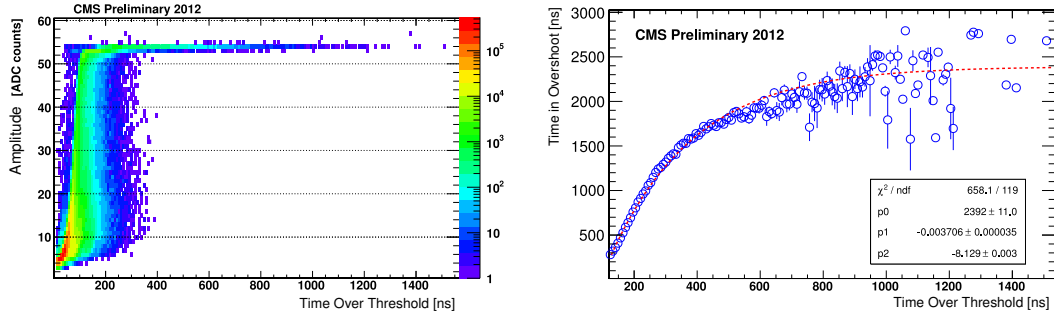


Figure B.8. Examples of distributions that are generated from the ADC analysis and used as inputs to the detector simulation.

- diamond-by-diamond single bunch hit probability,
- time over threshold,
- correlation between time over threshold/pulse amplitude and time in overshoot,
- evolution of overshoot amplitude.

Examples of the distributions that were used as inputs are shown in fig. B.8. The simulation is based on the hypothesis that the main source of inefficiency when counting bunch-by-bunch or integrated rates is that hits in bunches that come earlier in the fill pattern tend to "screen" hits from later bunches since the front-end electronics has not recovered from the previous hit. This is exacerbated by very energetic deposits that cause front-end saturation and lead to very long recovery times. In figure B.9 a comparison of the model and data collected while running with 1380 filled bunches is shown for the lead 400 bunch crossings. As can be seen, the overall drop off as a function of bunch crossing (roughly exponential) is reproduced in the simulation quite well. There is quite a bit of bunch-by-bunch variation that is not reproduced in the simulation as modelling these effects is outside the purview of this study.

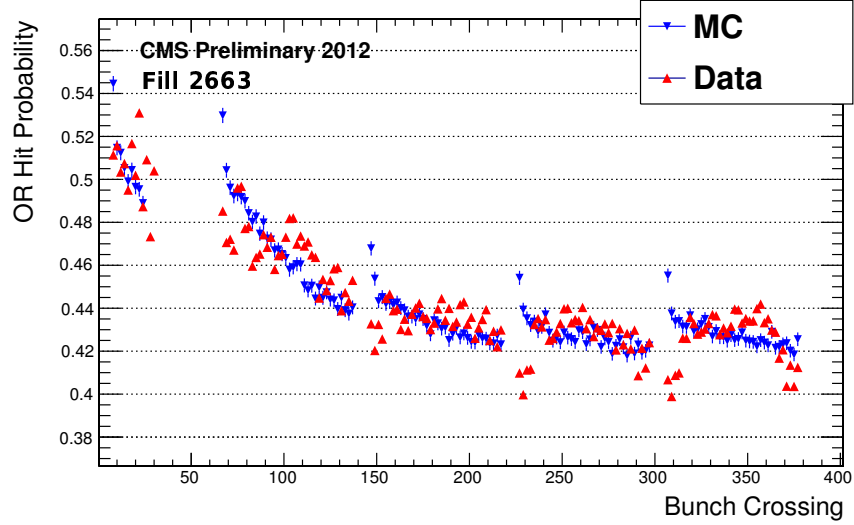


Figure B.9. Results of simulation of the BCM1F counting rate as a function of bunch-crossing for fill pattern with 1380 filled bunches, 1331 of which are colliding at IP5.

B.7. Conclusions

The BCM1F has demonstrated its effectiveness in measuring rates of both primary and secondary beam products during the first two years of running, and continues to do so into the third year of LHC running. It has proven valuable as a beam background, and has shown its viability as a luminometer.

Several studies are under way to assess radiation damage, the dependance of gain on rate, and effects of bias voltage polarization. The result of the knowledge gathered so far will guide plans for upgrades during the long shut-down of 2013-2014, and allow us to improve performance during the remainder of 2012. Plans for the upcoming shut-down include the installation of at least 8 new diamond sensors with the primary improvements being made on the construction of the front-end electronics. Some of the planned features of the new readout chip are,

- peaking time ≤ 10 ns,
- FWHM ≤ 10 ns,
- Baseline recovery ≤ 30 ns.

These improvements will make the BCM1F more robust in general and increase its viability as the primary online luminosity monitor at CMS.